In situ X-ray characterisation of photoinduced structural changes in solid ruthenium-sulfur dioxide complexes

A. E. Phillips
Trinity College, Cambridge

November 2010

This dissertation is submitted for the degree of
Doctor of Philosophy

DECLARATION

This dissertation is the result of my own work and includes nothing which is the outcome of work done in collaboration, except where specifically indicated in the text. It does not exceed the prescribed limit of 60 000 words.

. . . .

A. E. Phillips

PUBLICATIONS

Parts of chapters 3 and 5 have previously been published:

> Phillips, A. E.; Cole, J. M.; d'Almeida, T.; Low, K. S.
> "Effects of the reaction cavity on metastable optical excitation in ruthenium-sulfur dioxide complexes"
> *Phys. Rev. B* **2010**, *82*, 155118.

Further manuscripts based on the work reported here are in preparation:

> Phillips, A. E.; Cole, J. M.; d'Almeida, T.; Low, K. S.
> "High-temperature persistence of O-bound SO_2 in a solid ruthenium complex" (from chapter 3); communication in preparation for *J. Am. Chem. Soc.*

> Phillips, A. E.; Cole, J. M.; Low, K. S.
> "*L*-edge XANES analysis of ruthenium-sulfur dioxide photoisomerism in powders" (from chapter 6); article in preparation for *Phys. Chem. Chem. Phys.*

> Phillips, A. E.; Cole, J. M.
> "Bayesian analysis of the evidence for minor components: an alternative to the Hamilton $\mathcal{R}$-test" (from chapter 4); article in preparation for *Acta Cryst. A*

The following manuscripts in preparation report work done during the course of my Ph. D. which is not reported in this thesis:

> Higginbotham, A. P.; Cole, J. M.; Hickstein, D. D.; Phillips, A. E.
> "Fast calculation of hyperpolarizability of organic nonlinear optical molecules"; communication in preparation for *Appl. Phys. Lett.*

> d'Almeida, T.; Cole, J. M.; Phillips, A. E.; Ross, G.
> "Dual UV/X-ray chopper for laboratory millisecond time-resolved photocrystallography experiments"; article in preparation for *Rev. Sci. Inst.*

> Yeung, Y. M. C.; Pace, G.; Cole, J. M.; Phillips, A. E.; Friend, R. H.
> "Photochromism in PVA films containing ruthenium-sulfur dioxide complexes"; article in preparation for *J. Chem. Phys.*

ABSTRACT

X-ray diffraction provides an extremely detailed picture of the atomic structure of solids, but it has traditionally been restricted to the ground state. The emerging field of photocrystallography is beginning to allow the structure of optically excited states to be determined for the first time.

The work reported here centres on *in situ* photocrystallographic investigations of materials in the family $[Ru(SO_2)(NH_3)_4\mathbf{X}]\mathbf{Y}$, which are known to display two photoinduced, metastable states. In these compounds, the SO_2 ligand is respectively side- (O, S-) bound or O-bound, in contrast to the S-bound ground state.

Three new members of this family are presented:

1. **X** = isonicotinamide, **Y** = $(\text{tosylate})_2$
2. **X** = water, **Y** = $(\text{camphorsulfonate})_2$
3. **X** = pyridine, **Y** = $(\text{chloride})_2$

The photoexcited structures of compounds **1** and **2** are determined by single-crystal X-ray diffraction using laboratory and synchrotron sources. Compound **1** contains two crystallographically independent excitation centres. It exhibits a variety of metastable state geometries with different populations. Density-functional theory calculations demonstrate that the observed population of each geometry depends on steric repulsion from the crystal surroundings. Both compounds **1** and **2** exhibit significant populations of the O-bound metastable state at much higher temperatures (100 K to 120 K) than those at which this state has previously been observed (13 K).

The modelling and refinement strategy for these materials is discussed. A novel statistical test, based on Bayesian methods, for the reliability of models that include very small populations is presented.

Powder samples of all three compounds – including compound **3**, single crystals of which could not be grown – are analysed using Ru L-edge X-ray absorption spectroscopy. X-ray absorption near-edge spectroscopy is shown to be a suitable probe to measure photoexcitation in these systems, and reveals a slight increase in the Ru oxidation state upon photoexcitation. The structural change in compound **3** on photoexcitation is as expected from other members of this family.

Analysis of the data obtained on these three compounds reveals that the crystal surroundings of the photoexcitation centre strongly influence the geometry, population, and lifetime of the metastable states. These results are relevant to attempts to “crystal engineer” materials for applications in holographic data storage.

ACKNOWLEDGEMENTS

My grateful thanks go to everyone who enabled the work reported here to be done and made my time in Cambridge so enjoyable.

First and foremost, my supervisor Jacqui Cole provided a wonderful project, careful guidance, a proofreader's eagle eye and an unfailing sense of humour. Many thanks also to the other members of the Structure and Dynamics group: Thierry d'Almeida, for technical expertise especially at central facilities and adventures transporting *échantillons* across international borders; Kian Sing Low for good company and making marathon synchrotron sessions possible; T.-C. Lin for skills ranging from chef to chauffeur; Dan Hickstein and Andrew Higginbotham for many wide-ranging and profitable discussions; Nic Weng for demonstrating suitable sleep patterns for the writing-up process; and the new crowd: Alisha Cramer, Xiaogang Liu, Jignesh Radia, Sven Sylvester, and Martin Blood-Forsythe, for enlivening 428. Alisha, Sven and Martin made many helpful comments on early drafts of this thesis. Alicia Kelleher's calm competence kept everything going.

Jonathan Yates provided a great deal of assistance during my first forays into DFT calculations, and helpful feedback on my first-year report. When problems arose, Mike Payne pointed me in the right direction, consistently and speedily; his keen eyes was also invaluable in proof-reading drafts of papers. Michael Rutter was always ready to sort out my struggles with Linux and Fortran, as well as providing witty emails and the odd SATA cable. Tracey Ingham provided much-needed administrative support and advice. The TCM group as a whole dispensed strong coffee and scintillating conversation whenever necessary.

At Diamond, the expert support of Dave Allan, Harriott Nowell, and Sarah Barnett, on beamline I19, and Andy Dent and Giannantonio Cibin, on beamline B18, made experiments a pleasure. It is a further pleasure to acknowledge Dave along with Richard Needs for their very helpful comments as examiners of this thesis.

In the Astrophysics group, helpful conversations with Steve Gull and Rachael Padman improved chapter 4 immensely.

Enormous thanks are due to my referees, who were always ready to respond with wise advice to a pleading email, point me in the right direction, or write on my behalf: Cameron Kepert, Andrew Goodwin, Martin Dove, Mark Ellison, and of course Dr Cole herself. I am similarly indebted to Geoff Salem and Peter Simpson for their continued support. Liz New and Anelie and Neil Crighton provided sanctuary in Durham, friendly ears, and wise advice.

The communities of Beth Shalom and the Egalitarian Minyan, and the many wonderful people with whom I've shared a theatre or concert hall stage, provided essential respite from matters academic.

Ahmed Dahir Mohamed, introduced prematurely to the stress of the final year of a Ph. D., kept me going when everything looked bleak with endless love, support, and enthusiasm, not to mention the loan of his bike at crucial moments.

And, as always, I relied upon the support and encouragement of my wonderful family. Thank you.

CONTENTS

The science of crystallography is . . . now placed on a secure foundation [by the development of X-ray diffraction], supported equally by mathematics, geometry, and experiment, and its natural data are rendered available for chemists and physicists alike.

– A. E. H. Tutton
discourse delivered at the Royal Institution
Friday, March 14, 1913

CHAPTER 1

INTRODUCTION

> By showing how atoms arrange and disarrange themselves under innumerable variations of circumstances we must gain knowledge of the nature and play of the forces that bind the atoms together.
>
> – W. H. Bragg
> discourse delivered at the Royal Institution
> 5 June, 1914

1.1 Rationale and outline

It has been known for over a century that the structures of certain transition metal complexes change upon exposure to light, but only recently, with the development of the field of photocrystallography, have we been able to observe these structural changes directly. As this technique is relatively new, only a handful of excited-state crystal structures are yet known. However, this field holds great promise both to fundamental solid-state science, as a means of accessing a potentially vast array of novel structures, and to industry, where better understanding of the structural manifestations of optical excitation will allow the rational design of optically active materials.

The work presented here is a structural investigation of several members of the $[\mathrm{Ru(SO_2)(NH_3)_4}\mathbf{X}]\mathbf{Y}$ family (Figure 1.1), numbered for convenience in Table 1.1. This family is known to exhibit two different metastable states (Figure 1.2) but contains many more examples than have yet been investigated in detail. Of the materials listed here, only compound **4** has previously been studied, and both ground and metastable state crystal structures of compounds **1** and **2** are reported for the first time in this thesis. These compounds belong to the more general family of photoinduced linkage isomerism complexes,

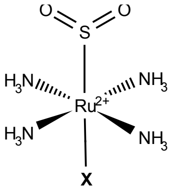

Figure 1.1: Generic structure of the $[Ru(SO_2)(NH_3)_4\mathbf{X}]^{2+}$ ion.

Table 1.1: Compounds belonging to the family $[Ru(SO_2)(NH_3)_4\mathbf{X}]\mathbf{Y}$ studied as part of the work reported here.

Compound	X	Y
1	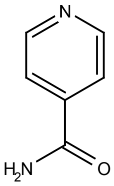 isonicotinamide	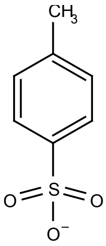 tosylate
2	H_2O	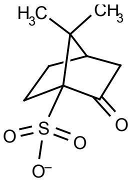 camphorsulfonate[a]
3	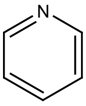 pyridine	$Cl^-/CF_3SO_3^-$ [b]
4	H_2O	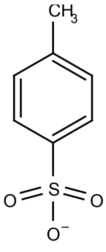 tosylate

[a] Racemic; shown here is the 1*S* isomer. [b] See discussion in Section 6.2.2.

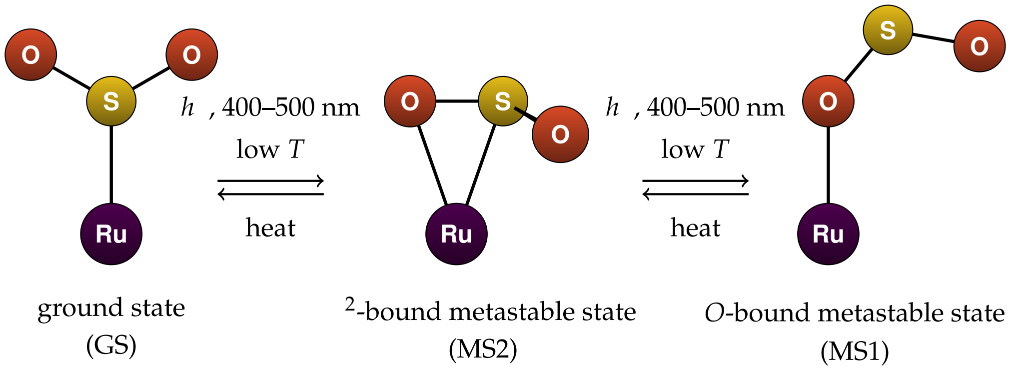

Figure 1.2: Schematic diagram of the ground and metastable states of the $[\mathrm{Ru(SO_2)(NH_3)_4}\mathbf{X}]^{2+}$ ion.

whose technological applications, particularly in high-density data storage, are the focus of much current research.

This topic thus arises from a confluence of circumstances: the advances in crystallography that have allowed these metastable states to be observed; the phenomenon of linkage isomerism and in particular the striking versatility of sulfur dioxide as a ligand; and the developing technologies which are poised to take advantage of the photoswitching behaviour of these materials. In the remainder of this chapter, I discuss the background to each of these factors in turn. The following chapter outlines the experimental and theoretical techniques used to investigate these materials.

The four central chapters of this thesis detail its principal results. In chapter 3, the results of the photocrystallographic experiments performed are presented. Chapter 4 presents a statistical test for the significance of crystallographic data with small minority populations, such as those obtained in the photocrystallographic experiments. Chapters 5 and 6 present complementary work designed to help interpret the crystallography: density-functional theory calculations and X-ray absorption spectroscopy measurements, respectively. Finally, chapter 7 summarises the material presented here and offers some suggestions regarding the future work arising from these results.

1.2 A brief history of X-ray crystallography

In 1895, Röntgen published the first systematic study of the mysterious radiation produced by firing electrons at a metal target in an evacuated tube.[1] This work fired both scientific and popular imaginations. The wave nature of "X radiation" was hotly disputed: while these rays appeared to be polarisable, they could not readily be reflected or refracted, and the manner in which they ejected photoelectrons from a metal surface could only be explained by a corpuscular model. Nonetheless, tentative measurements suggested that, if these rays were indeed wavelike, their wavelength would be around 10^{-10} m.[2] Meanwhile, it had already been suggested that crystals consisted of arrangements of atoms repeating regularly in three dimensions, and on the basis of known interatomic distances the length of the repeating unit could also be estimated at around 10^{-10} m. Based on the similarity of these length scales, von Laue correctly predicted that X-rays should diffract from crystals. In 1912 he and co-workers showed that X-rays diffracted from a crystal of copper sulfate; X-rays thus assumed their rightful position in the electromagnetic spectrum.[3]

X-ray diffraction had thus revealed the nature of the scattered beam. This phenomenon proved more useful, however, as a powerful probe of the diffracting crystal. By today's standards, data extended only to low resolution, intensity measurements from photographic film were coarse, and the models fitted were simplistic. Nonetheless, the method was the first to produce direct images of matter on an atomic scale, and many important structural results followed rapidly. Indeed, the very word "crystallography" soon became shorthand for this single experimental technique.[4]

Subsequent developments in sources, detectors, and solution and refinement techniques improved the quality of data substantially, in turn allowing more sophisticated models to be fit. Crystallography nonetheless remained exclusively a ground-state technique: a potent source of structural information but silent with respect to dynamic features. Two barriers prevented these features from being investigated. First, diffraction experiments by their very nature produce data which are averaged over time and space, making it difficult to investigate local or transient excitations. Perhaps more significantly, such features were widely assumed to be uninteresting or simply non-existent. The prevailing view was summarised by the 1939 Chemistry Nobel Laureate Leopold Ruzicka's claim that "a crystal is a chemical cemetery," a rigid and unchanging array of little relevance in comparison to the dynamic behaviour observed in solution.[5]

This assumption, however, has since been significantly challenged by advances in materials chemistry and physics. Solid materials are at the core of many technologies central to modern society, ranging from data transmission (optic fibres) and storage (DVDs) to energy generation (solar cells) and transport (batteries, hydrogen storage materials). Modern X-ray diffraction methods have allowed their structures to be modelled in unprecedented detail. The behaviour of such functional materials, however, cannot always be understood without reference to their dynamic as well as structural properties: how they respond to changes in their thermal, mechanical, chemical or optical environment. Furthermore, this information is invaluable in engineering new materials with desirable properties.

Fortunately, crystallographic techniques are proving potent sources of information on dynamics as well as structure. The quality of single-crystal diffraction data has increased to the point where anisotropic displacement parameters are routinely collected for non-hydrogen atoms, and have yielded great insight into the vibrational motion that indeed occurs.[5] (See, for example, the work of Maverick and coauthors on the barriers to rotation of *tert*-butyl groups in crystals,[6] or the present author's work on the thermal expansion of cyanide frameworks.[7]) In addition, it has been recognised that experiments can be performed specifically to elucidate the dynamic properties of a material by *in situ* modification of the conditions in which the sample is held. Many such perturbations are possible. Multiple-temperature experiments can yield insight into vibrational modes in solids. High-pressure techniques, particularly at synchrotron sources, were initially of interest to geological research but have since become increasingly common and applicable to a much wider range of studies.[8,9] A third option is to absorb guest molecules into, or desorb them from, a porous framework.[10–12] A wide variety of useful material properties can be probed in this way, allowing their precise structural origin to be determined, and hence new functional materials, with properties tuned to their intended application, to be designed.

This thesis describes work on still another possible perturbation: activation of selected electronic excitations by shining light on a single-crystal sample, a technique known as photocrystallography.

1.3 Photoactive materials

1.3.1 General principles

The crucial difference between reactions in the solid state and those in solution or gaseous phases is clearly the comparative lack of translational and rotational freedom within a rigid matrix. In the particular case of single-crystal-to-single-crystal transformations, therefore, it becomes important to ensure that the moieties which are to react are in close proximity within the crystal structure, a restriction known as the *topochemical postulate*.[13] This condition, which must be met for a reaction to occur in the first place, is distinct from the condition that the products should adopt a similar shape to the reactants. If they do not, crystals may crack under the internal stress caused by the reaction; see Section 2.1.

Several classes of photoactivated chemical reactions are particularly compatible with the topochemical postulate, either because the reacting moieties are part of the same molecule and are thus chemically bound to one another, or because only one reactant is involved. Intramolecular cycloaddition reactions involve a substantial change in chemical bonding with comparatively little difference in the nuclear positions. In particular, the conversion of into electron density can disrupt conjugated chains, altering the UV/visible absorption spectra of the molecule and resulting in photochromic materials.[14] On the other hand, *cis-trans* isomerism reactions in alkenes cause no change in bond sequence, but may induce either a very large change in nuclear positions or large internal stress within the solid. For this reason such reactions are often investigated within polymeric rather than crystalline matrices.[15–17]

Somewhere between these two classes of reaction falls the class of photolinkage isomerism reactions in transition metal complexes, which will form

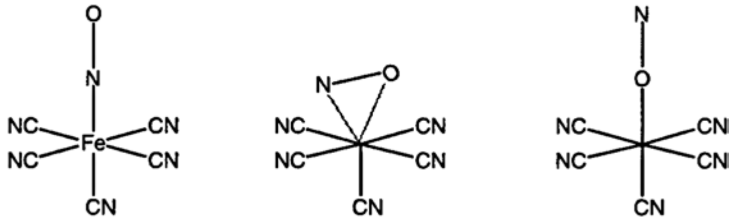

GS (η^1) MS2 (η^2) MS1 (η^1)

Figure 1.3: Ground (GS) and excited state (MS1 and MS2) geometries of the nitroprusside ion. Diagram by Buchs *et al.*[31]

the focus of this thesis. Several ligands, including NO_2, SCN^-, and CN^-, are famously *ambidentate* – able to bind through several different atoms[18,19] – and such complexes may exhibit photoexcited states in which the linkage mode differs from the ground state.[16,20] These states are more likely than the products of the reactions discussed above to be metastable, reverting thermally to their ground states.

It is worth noting that the material properties of compounds which undergo these types of photoreaction can be radically different, which can affect both their experimental accessibility and, potentially, their commercial viability. In particular, sublimation can be an excellent method of growing small single crystals of organic photoactive materials,[17] while recrystallisation from solvent must be used for the less volatile transition metal complexes. In some situations, it is possible to alter these material properties by embedding the photoactive component in a non-reactive matrix, either crystalline[21] or amorphous.[15,17,22,23]

Of the ligands that undergo photolinkage isomerism, NO, NO_2 and SO_2 have been most extensively studied using photocrystallography. For this reason, they are each considered in more detail in the following sections. Other ligands which exhibit this phenomenon, but which will not be further discussed, include N_2,[24,25] thiocyanate (on irradiation with rays),[26] dimethylsulfoxide,[22,27] and other organic sulfoxides.[28–30]

1.3.2 Complexes of NO

The first compound to have a metastable excited state photocrystallographically studied was sodium nitroprusside (sodium pentacyanonitroferrate(II), $Na_2[Fe(CN)_5(NO)] \cdot 2\,H_2O$). This compound is used medically to deliver nitric oxide to treat cardiac failure.[32] Studies using both neutron[33–35] and X-ray[36,37] diffraction culminated in the result that two photoexcited states are linkage isomers of the ground state: one in which the NO ligand is η^1- (end-) bound through the oxygen, and one in which it exhibits η^2 (side-bound) linkage (Fig. 1.3).

Analogous effects have been discovered in a variety of NO complexes,[38–40] and several reviews have been published.[20,41,42] Density-functional theory calculations have also been performed to elucidate the mechanism for these phototransformations.[31,38–40,43–47]

Although NO compounds are important as among the first and best-studied photolinkage isomerism compounds, it should be noted there are important differences between this diatomic ligand and the triatomic ligands discussed below. On the one hand, these complexes are more theoretically tractable, as the isomerisation process can be well modelled by considering a single degree of freedom, the Fe—N—O angle.[43] (For completeness, one would also have to consider rotation about the ground-state Fe—N—O axis, which allows several geometries for MS2: typically two are observed.) Moving to a triatomic ligand results in a concomitant increase to three degrees of freedom, increasing the complexity of computational treatments (*cf.* Section 5.2). On the other hand, the difference in electron density between GS and MS1 in the nitroprusside ion formally arises from the position of a single electron, so that very careful X-ray studies, complemented by neutron work, were needed to unambiguously identify this species. While the extra atom in triatomic ligands may “get in the way” in excited-state geometries through steric interaction with the surrounding crystal lattice, its presence usually makes excited states more crystallographically apparent, even when present in relatively small fractions, thus reducing ambiguity in the structure refinement process.

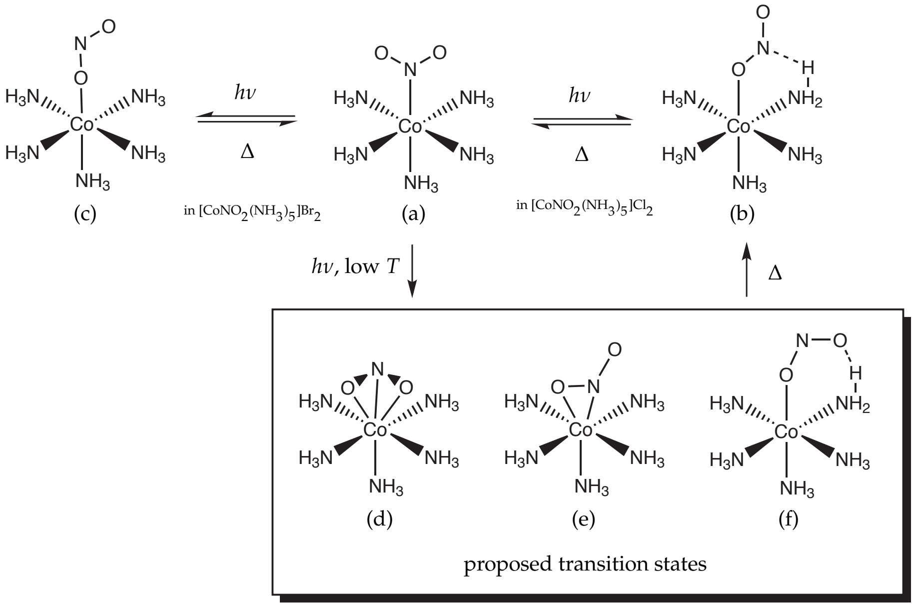

Figure 1.4: A menangerie of observed and proposed geometries of the $[CoNO_2(NH_3)_5]^{2+}$ ion: the ground N-bound (nitro) state (a) can be transformed by irradiation with blue or UV light into an O-bound (nitrito) state with an *exo* geometry (b) in the chloride salt or a linear Co O N linkage (c) in the bromide. The chloride also displays a low-temperature intermediate which has variously been identified as ^{3}-bound (d), ^{2}-bound (e), or O-bound (nitrito) with *endo* geometry (f).

1.3.3 Complexes of NO$_2$

It has been known since the earliest days of coordination chemistry that the two isomers of $[Co(NO_2)(NH_3)_5]Cl_2$ (Fig 1.4(a) and (b)), which can be independently synthesised, can also be readily interconverted either in the solid state or in solution. The *N*-bound “nitro” isomer can be transformed to the *O*-bound “nitrito” form by irradiation with blue or ultraviolet light, while the *O*-bound isomer reverts thermally to the *N*-bound form over time (typically several days in the solid).[48] Since then, the $[Co(NO_2)(NH_3)_5]^{2+}$ ion has been subject to extensive investigation using crystallographic and other methods. Experiments using ^{18}O-labelled ligands and ^{17}O-NMR spectroscopy have shown that both the thermal[49] and photochemical[50] transformations are intramolecular; moreover, scrambling between the bound and free oxygen atoms in the *O*-bound isomer can occur rapidly.[51–53] Consideration of the quantum yields obtained from excitation at various wavelengths has led to the hypothesis that the first process occurring on photoexcitation is the population of a dissociative ligand-metal charge transfer band, following which the NO_2 fragment either recombines with the complex, with or without isomerisation, or undergoes redox decomposition.[54] Differential scanning calorimetry measurements have suggested that the thermal equilibrium state of the chloride system is in fact a mixture of the *N*- and *O*-bound isomers, with an equilibrium ratio of NO_2:ONO$= 7.7(8)$ at 333 K.[55]

It was at first generally agreed that the isomerisation reactions occur *via* an ^{2}-bound transition state (Fig 1.4(e)),[50,51,56] although on the basis of the oxygen scrambling an ^{3} intermediate has also been proposed (Fig 1.4(d)).[52] A metastable species has been observed in the IR spectrum of the solid complex when irradiated at low temperatures: it has been proposed that this species is the postulated intermediate. Significantly, however, its structure has never been directly observed;[57] this is considered further in section 5.4.

This system introduces the theme of crystal packing effects, which will prove central to the work presented in this thesis. Crystallographically, the thermal *O*-to-*N*-binding transformation has been observed in single crystals. This involves two steps: first the ligand itself isomerises from *O*-bound to *N*-bound local geometry, then the crystalline surroundings relax from $P2_1nb$, the space group in which the *O*-bound complex packs as synthesised, to $C2/c$, that which the synthesised *N*-bound complex adopts.[56] (Note that a non-standard setting of $Pna2_1$ is used here in order to aid comparison between the two structures without the complication of relabelled axes.) The reverse photochemical reaction has only been investigated completely using powder diffraction methods, as crystal cracking prevents this transformation from occurring to completion within a single crystal.[58] In other words, only the first step of the analogous process has been observed for the reverse transformation; presumably, however, if the internal stresses could be relaxed without destroying the crystal, this would result in a return to $P2_1nb$ in a manner analogous to the second step. With a view to understanding how the crystal surroundings influence the isomerisation reaction and *vice versa*, the kinetics and structural changes associated with the photoactivated and thermal transformations of the $[Co(NO_2)(NH_3)_5]^{2+}$ ion, combined with a variety of counteranions, have been extensively studied by Boldyreva and co-workers.[59–65]

In the present work, relatively small photoexcitation yields are achieved, rendering irrelevant the question of rearrangement as 100% conversion is approached. However, computational methods such as random structure searching may well find lower-energy packings of the ^{2} geometry than that formed from the ground state packing. Moreover, the surroundings nonetheless exert an important influence on the photoisomerism behaviour (Chapter 5).

1.3.4 Complexes of SO_2

Sulfur dioxide is an exceptionally versatile ligand known to exhibit a wide variety of coordination modes, either binding to a single atom or bridging several atoms.[66,67] Interest in the linkage photoisomerism of ruthenium-sulfur dioxide-based compounds began with the observation of a metastable species in the IR spectrum of $[Ru(SO_2)(NH_3)_4Cl]Cl$ when irradiated with light at low temperatures.[68] In contrast to the *S*-bound ground state (Fig. 1.5, left), Coppens and co-workers reported on the basis of single-crystal X-ray diffraction measurements that this metastable species is an ^{2}-linked system (Fig. 1.5, centre). Moreover, related compounds in the $[Ru(SO_2)(NH_3)_4\mathbf{X}]\mathbf{Y}$ family also display an analogous metastable state.[69,70] A further, *O*-bound excited state was predicted from DFT calculations (Fig. 1.5, right),[69] and indeed this state has since been crystallographically observed in compound **4**.[71]

Despite also being triatomic, this ligand differs from NO_2 in two important respects. First, the side-bound isomer has been unequivocally observed *via* X-ray crystallography. Second, the thermodynamics – both the relative energies of the various geometries, and the energy barriers separating them – differ. In SO_2 the *O*-bound state is significantly less stable than the side-bound one, and decays to the side-bound state even at liquid nitrogen temperatures (see Section 3.6); while in NO_2 the *O*-bound isomer is stable for days at room temperature in the solid state, and the putative intermediate is only observable at liquid nitrogen temperatures.

This system has been well characterised by photocrystallography, and

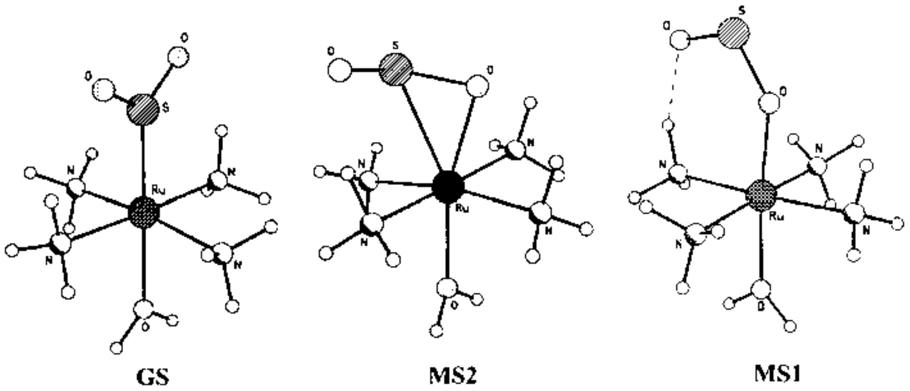

Figure 1.5: Theoretical ground and metastable state geometries of the $[Ru(SO_2)(NH_3)_4H_2O]^{2+}$ ion, present in compounds **2** and **4**. Figure by Kovalevsky *et al.*[69]

thus provides a convenient reference for the development of new experimental or computational methods. In addition, the family of complexes $[Ru(SO_2)(NH_3)_4\mathbf{X}]\mathbf{Y}$, where the *trans* ligand **X** and counterion **Y** may be varied relatively freely, provides fertile ground for exploring the factors which influence photoexcitation behaviour, which form the principal subject of this thesis.

1.4 Applications

1.4.1 Data storage

In an era characterised by ever-increasing amounts of data being generated and stored electronically, the search for more efficient and compact methods of storing this data is of great importance. Despite the success of modern optical storage media, the bit density in these materials is approaching the maximum achievable under the Rayleigh criterion; beyond this limit, diffraction effects will prevent individual bits from being optically resolved.[72] As such, there is an impetus to develop methodologies for storing more than one bit of information in each "pixel", improving both the storage density and the readout time: for instance, holographic storage takes advantage of the storage material's anisotropic refractive index to write three bits of data into each pixel. This technology can potentially support very high information densities of up to 10^{14} bits cm^{-2}.[73]

Relatively few materials suitable for this purpose, however, have so far been identified. Photocrystallographic studies of metastable excitations therefore provide an important means of investigating potential new materials for these applications.[74] Such materials must demonstrate clearly defined bistability so that data can be easily and accurately read and written. Different kinetic behaviour will produce materials suitable for different applications: irreversible photoinduced changes would produce read-only write-once media, while reversible or metastable changes would give rewritable media. Depending on the properties of the material in question, the media could be erased by thermal, optical, or magnetic control.

1.4.2 *Photoswitchable material properties*

The potential applications of these compounds will depend on what property of the "switched" material is to be measured. Various optical properties are of interest, including *photochromism*, where a material's absorption spectrum changes on irradiation with light, and *photorefraction*, where it is the refractive index which changes. In particular, holographic data storage relies upon the photorefractive properties of the recording medium. Sodium nitroprusside and other NO complexes that undergo linkage photoisomerism have been investigated as media for holographic data storage.[73,75] The photorefractive properties of these materials arise from the existence of the optically accessible metastable states (Section 1.3.2), rather than the Pockels effect (where birefringence is induced in proportion to the applied electric field, which is only possible in noncentrosymmetric systems).[76] This gives rise to unusual and potentially useful recording kinetics.[77] Measurable phase gratings have been written in sodium nitroprusside at both low[78] and ambient temperatures.[79] Many other photorefractive materials are being investigated for data storage purposes, including amorphous azobenzene-based polymers and other organic materials.[80]

Alternatively, photoinduced mechanical deformation may be used as the basis of a switching medium. Attempts to induce macroscale deformation of single crystals must strike a careful balance. If the interactions between neighbouring units are weak or the changes in molecular geometry small, the cell parameters will not be substantially altered by photoexcitation, so that the macroscopic deformation will be similarly small. However, if the changes in molecular geometry are too large – and in particular, if the crystal packing in the excited and ground states differ substantially – the strain placed on the crystal by photoexcitation is likely to cause it to crack. It should be pointed out that there is no necessary correlation between a large or small induced strain and the presence or absence of a change in the space group; symmetry changes may result from subtle atomic displacements, and equally substantial changes in molecular shape or packing need not alter the space group.

Despite the difficulties mentioned, several examples are known of single-crystal-to-single-crystal transformations which cause macroscopic geometric deformations.[17,81] It has been suggested that this effect requires a high level of global randomness in the excited state (*i.e.*, a lack of cooperativity between excited centres).[17] This requirement stands in stark contrast with other applications, where cooperativity between centres is a highly desirable goal in order to increase the excitation fraction achieved and hence enhance the material's bistability.

CHAPTER 2

TECHNIQUES

> Professor Röntgen's discovery of a new form of energy affecting sensitive plates reached this country in a somewhat exaggerated and inaccurate shape. . . . What may be called the popular and superficial aspect of his discovery has been seized upon with avidity. Shadow photographs have suddenly become an article of commerce; no illustrated paper is complete without reproductions of pictures showing the transparency of the human hand; every one who can command a vacuum tube and a few sensitive plates is busy repeating the primary experiment; ladies prattle of the new photography, and physicians already dream of unheard-of cures by its agency, and the market price of exhausted tubes – many of them of little value for the purpose in view – is rapidly rising.
>
> – *The Times*, Tuesday, 4 February, 1896

2.1 Photocrystallography

Many solid-state chemical reactions, including those which are photoactivated, can be investigated using traditional crystallographic techniques simply by comparing the diffraction patterns of a sample before and after reaction. By contrast, the term "photocrystallography" usually refers to a distinct experimental technique where the sample is irradiated *in situ*, allowing structural changes to be monitored directly as they occur. Single-crystal to single-crystal photoreactions were first investigated using this method by Nakanashi and co-workers, who monitored the [2+2]-dimerisation of 2-benzyl-5-benzylidene-cyclopentanone;[82] several similar experiments have since been performed and are summarised in a recent review.[83]

All photocrystallographic experiments involve collecting both “dark” data, from samples in the ground state, and “light” data, from samples during or immediately after irradiation with light. In almost all cases, the “light” data set will still contain a substantial proportion of the ground state. The two data sets are then individually refined to yield models for the ground and excited states and a numerical value for the excitation fraction achieved (*cf.* Section 2.1.3).

Within this basic framework, however, a variety of methods is possible.[84] First, the experimental procedure will depend strongly on the lifetime of the excited state. The methods of photocrystallography have been applied on timescales ranging from the ultrafast[85,86] to the metastable (see references in Section 1.3); the differences in procedure this entails are outlined below.

Second, suitable radiation must be chosen for both the “pump” (excitation) and “probe” (structure determination) steps. The “pump” wavelength should be chosen with regard to the UV/visible absorption spectrum of the material; choosing an absorption peak is liable to result in an unfeasibly short optical penetration depth, so that a shoulder or other weak absorption region may be more useful.[87] With respect to the probe radiation, as in general in crystallography, neutrons and X-rays find complementary uses due to their different scattering properties. Since neutron measurements require larger samples, however, limited optical penetration depth can severely limit the excitation achievable; thus neutron techniques are not as frequently useful as in conventional crystallography. It is possible to select particular X-ray wavelengths in order to perform anomalous scattering experiments. Laue methods, in which the crystal is irradiated with a wide range of wavelengths, are also possible; since multiple reflections can satisfy the Bragg condition simultaneously and thus collection times tend to be shorter, these methods are particularly popular in experiments on transient species.[84] Several complications, however, affect methods that use polychromatic radiation. Multiple diffraction peaks may overlap, making it difficult or impossible to resolve them; the absorption and extinction coefficients and structure factors will vary with X-ray wavelength; and Laue methods necessarily involve exposing the crystal to much higher intensities of X radiation. One increasingly popular compromise is to use “pink-beam” radiation, which is polychromatic but of limited bandwidth.[88,89] Both Laue and pink-beam methods are only possible at synchrotron facilities.

Finally, samples in a variety of different states may be probed by appropriate experimental techniques. Photoswitching effects have been observed in single crystals, powders, and polymer films, and in particular both single-crystal and powder photocrystallography are possible. It has been shown that the photoexcited population achieved may vary substantially between single-crystal and powder-based experiments. This variation has been attributed to effects dependent on the angle of light polarisation with respect to the direction of the photoactive ligand.[39,90] It has further been suggested that preferred orientation effects may be significant in powder-based experiments, which typically use a planar geometry for ease of irradiation. However, in at least one case it has been shown by comparison with capillary measurements that such effects are not necessarily important; moreover, if the photoexcited structure is refined against the relative differences in intensity of the Bragg peaks, any such effects would be expected to cancel out.[91] Photoswitching behaviour in films, which are among the more useful phases for applications, will naturally depend on the microstructure surrounding the excitation centres. For instance, preliminary transmission electron microscopy imaging of polyvinyl alcohol films containing the ruthenium-sulfur dioxide complexes discussed here indicates that these materials exist as small crystals embedded within the film.[92] Consequently, photocrystallograhic results are directly relevant even to this different medium.

The present work focuses on metastable, reversible transformations in single crystals, using monochromatic X-ray probes. A brief outline of photocrystallography on both long-lived and transient states is provided in the following sections.

2.1.1 *Long-lived excitations*

If an excited state lifetime is comparable to or longer than the timescale of a full crystallographic data collection, the nature of the excitation can be probed simply by comparison of a “dark” crystal structure obtained prior to irradiation with a "light" structure obtained afterwards. Only a single irradiation step thus needs to be performed. Three main obstacles can hamper the collection and interpretation of crystallographic data concerning long-lived species: the limited extent to which the transformation occurs; the limited lifetime in which measurements must be taken; and crystal damage caused by overheating, strain from the photoinduced geometric change, or, particularly in polychromatic experiments, X-ray absorption.

First, only a relatively small fraction (typically 20%) of the unit cells will exhibit the desired transformation.[84] This is partly an inevitable consequence of the fact that X-rays will have a greater penetration depth into the sample than visible light (although this effect can be minimised by judicious choice of crystal size and irradiation wavelength) and partly a deliberate experimental choice, since causing more unit cells than this to react may strain the lattice to such an extent that the crystal cracks.[58] As a result, the structure collected after irradiation will still exhibit a large fraction of the ground state. This must be subtracted off, using data from a careful "dark" collection corrected for any change in unit cell parameters, in order to reveal the photoexcited state *via* a Fourier difference map. The structure of this state can then be refined together with the ground state, with occupancy factors of the ground and excited states constrained to sum to 100%, to give a value for the fraction of photoexcitation observed along with ground and excited state structures. In extreme cases it may not be possible to include the metastable state atoms without rendering the model unstable to refinement. Even in these cases, though, a difference density map between the "light" data and the ground-state model may still demonstrate the presence of unmodelled electron density due to the metastable state, without providing quantitative information about its geometry or the excitation fraction achieved.

It follows from this that, for a successful data collection, the ground state structure should be very accurately known. Ideally, it should not be disordered, since the inclusion in the "light" model of some fraction of the excited state will itself introduce considerable disorder into the structural model, although the present work demonstrates that this is not an insurmountable obstacle. Similarly, structures in which a molecular group exhibits thermal libration are best avoided.

The second problem is simply collecting sufficient data within the lifetime of the excited state, which requires that the crystal, source and detector all be carefully chosen.[84] If the crystal has high symmetry, a complete structural model can be obtained from a relatively small volume of reciprocal space. However, symmetry elements intersecting the photoactive ligand, causing disorder in the metastable state, are then more likely. Although high symmetry makes it easier to collect large amounts of data, it is no guarantee of an easy refinement. The X-ray source should have high intensity, so that strong reflections can be detected even from a relatively small crystal (chosen for reasons of optical penetration depth discussed above), and a short wavelength, to increase the resolution of data collected within a given maximum scattering angle 2θ. The choice of wavelength is, however, limited by the requirement that the diffracted X-ray intensity must remain detectable at maximum 2θ, since atomic form factors will decrease with 2θ faster at smaller wavelengths. The detector should cover a large area with low readout time; here modern charge-coupled device (CCD) area detectors represent a good balance between speed and sensitivity.

Finally, as discussed above, the experiment must be designed to minimise sample damage by limiting the amount of excitation that occurs and the X-ray and optical irradiation times – or, particularly in Laue experiments, to maximise the amount of data collected before the sample invariably disintegrates.

2.1.2 *Transient excitations*

In contrast to the metastable case, transient photoexcited states must be regenerated continuously during data collection. In order to prevent damage to the crystal, either from excess heating or from strain caused by structural change, the light source is typically pulsed. To prevent the observed pattern from being swamped by the ground-state structure, the X-rays must themselves be pulsed so that the times when data are collected correspond to times when the crystal is illuminated, and thus the data represent a relatively high proportion of the excited state.

This is achieved by one of two methods, depending on the lifetime of the photoexcited state. If it is of the order of microseconds, a mechanical "chopper" can be used to break the X-ray beam into pulses.[93,94] For smaller lifetimes, of the order of nanoseconds, the temporal structure of a synchrotron must be used, so that the beam itself is generated in such a way as to have the required pulse pattern.[95] In either case, the X-ray flux reaching the crystal decreases dramatically, so that sensitive detectors and long experimental times are necessary to obtain meaningful data, which has only become possible relatively recently. As previously mentioned, Laue and pink-beam methods ameliorate this problem to some extent. Once collected, the "dark" and "light" data are treated in the same way as for the metastable case, whereby the Fourier difference map between the ground-state model and data collected after irradiation is interpreted as the geometric change associated with photoexcitation.

Since the structural changes associated with photoexcitation are often subtle, it is important to ensure that any observed changes cannot be ascribed to other phenomena – for instance, a change of temperature due to laser heating. For this reason, data collection is typically arranged so that frames of the "light" structure are collected in alternation with frames of the "dark" structure, so that effects due to crystal heating are properly accounted for in the dark reference structure. This method also has the advantage that, in the unfortunate event that the crystal cracks or is rendered unusable in the middle of the experiment, the data obtained until that point may still be able to be refined. By contrast, a "light" structure without the corresponding "dark", ground-state measurement is worthless, since the crucial step of subtracting off the ground state electron density becomes impossible, and thus the crucial change in electron density cannot be determined.

Although the work described here does not involve transient excitations, the metastable states of the compounds discussed have transient lifetimes at room temperature. The low-temperature metastable state structure determinations reported will thus provide an important reference for future transient work, both as well-studied systems to test apparatus and as a starting point for analogous experiments.

2.1.3 Refinement

Broadly speaking, the final refined model for a photocrystallographic experiment should contain the metastable state geometry with some fractional occupancy and the ground state with occupancy (1). However, it is not trivial to decide exactly which parameters to include in the model and at which stages of the refinement to allow them to vary.

The potential problems which must be avoided are as follows: first, an anisotropic model simultaneously including ground and metastable states will require a large number of parameters. This in turn will require a well-diffracting crystal and careful data collection so that sufficient meaningful data are available. With modern equipment, this criterion is not usually difficult to meet.

Secondly, a more serious issue is that certain sets of these parameters are likely to be highly correlated. Fractional occupancies which are allowed to vary are notoriously highly correlated to the atomic displacement parameters (ADPs) of the same atoms. For instance, a model which gives too high an electron density at a particular atom can be corrected either by lowering the occupancy of that atom or by increasing its ADPs. Moreover, since the ground and metastable state geometries often overlap, the same region of electron density may contain substantial contributions from several different atoms, again leading to high correlations. (In practice, of course, the comparison between model and data is done in reciprocal rather than real space; the result, however, is identical to that described using the real-space argument above.)

As a result of this, care is needed in treating the near-singular covariance matrix. In particular, some researchers have argued that the ground-state model should be refined against the "dark" data before being imported as a series of rigid bodies into the "light" refinement.[69] This has the advantage of reducing both the number of parameters being refined during the "light" refinement and the correlation between them. However, the severity of correlation problems will vary greatly depending on the system under consideration. In particular, systems such as the SO_2 complexes discussed in the present work are significantly easier to model than NO complexes, where MS1 (*O*-bound) overlaps completely with the ground state (*N*-bound) and formally differs from it in electron density by the position of a single electron.

The third issue has already been alluded to: a decision must be made as to which atoms to allow to occupy different locations in the ground and metastable states. The closer the ground and metastable positions are, the more important rigid-body constraints for the ground state become. On the one hand, significant changes have been observed in some crystal structures outside the immediate photoisomerism region, such as changes in the metal-ligand bond length *trans* to the photoisomerising ligand.[69,96] On the other hand, most atoms will not move substantially upon excitation; this method therefore risks using two essentially superposed ADP ellipsoids to "mop up" any residual electron density in the vicinity of the atom modelled, potentially leading to distortion of the metastable-state model. The relative merits of these choices have been discussed in the specific context of spin-crossover compounds.[97]

Finally, it should be noted that, in principle, it is possible to distinguish a random distribution of the photoexcited state from one in which excited centres cluster together.[98] In the limit of a completely random distribution, the structure factors F from each component sum to give the total reconstructed from the observed data. In the limit where ground and photoexcited states are entirely separate, the situation is as if two separate crystals are separately diffracting X-rays, so that it is the intensities, or F^2 values, which sum. Inspection of intensity statistics can suggest which of these extremes is more relevant to a particular data set. There is no evidence of clustering in the present work, however, and the distribution will be modelled as completely random.

2.2 Density-functional theory

2.2.1 *Overview*

Photocrystallography as a technique is rapidly developing, challenging to perform, and often demanding in terms of experimental resources such as synchrotron beamtime. As such, computational simulations can provide vital support at both the preparation and analysis stages of an experiment. Recent advances in both computing power and the algorithms used for *ab initio* calculations have made it tractable to model relatively large systems, such as the complexes studied here. This section will provide a brief overview of the density-functional theory (DFT) techniques used in this thesis.

2.2.2 *Background*

The complete time-independent many-body wavefunction for a system containing N electrons is a function of $3N$ variables, a position in three dimensions for each electron. However, it has famously been shown by Hohenberg and Kohn that the external (*i.e.*, nuclear) potential V acting upon such a system is uniquely determined by the ground-state electron density $n(\mathbf{r})$, a function of only three variables.[99] Since the kinetic energy operator in the Schrödinger equation is known, this potential in turn defines the Hamiltonian for the relevant system, which can be inserted into the Schrödinger equation to solve for the ground-state wavefunction . This determines all observable properties of the ground state of the system, and we can thus conclude that all such properties – and in particular the ground-state energy E – are unique functionals of the ground-state electron density:

$$E = E \;\, n(\mathbf{r}) \tag{2.1}$$

In practice, the exact form of the functional $E[n]$ is not known; indeed, since it is so highly nonlocal, it will be sufficiently complex that it would require the use of major approximations to be of any practical use even if it were. We thus rely upon an approximation scheme in which as many contributions as possible to the total energy are treated exactly, leaving a comparatively small (although physically very significant) term to be approximated by various means.

Using a construction due to Kohn and Sham,[100] we consider an auxiliary system of *non-interacting* particles with the same ground-state density of the system under consideration, moving in a potential defined by

$$V_{\text{KS}} = V_{\text{ext}} + \frac{\quad}{n(\mathbf{r})} \quad \frac{1}{2} \quad \frac{n(\mathbf{r})n(\mathbf{r}\;)}{\mathbf{r} \quad \mathbf{r}}\, \mathrm{d}\mathbf{r}\, \mathrm{d}\mathbf{r} \;\, + E_{\text{xc}}[n] \Big\} \tag{2.2}$$

(where atomic units have been used in which $\hbar$, m_e, e, and $4\;\;\,_0$ are all numerically equal to 1). The first term on the right-hand side represents the electrons' energy of interaction with the ions and any other external potential; the second gives the Coulombic repulsion energy between the electrons in their average positions. The final "exchange-correlation" functional is necessary to account for forces which occur naturally in the real system but must be specifically included in the auxiliary one: repulsion between electrons of the same spin due to Fermi statistics (exchange) and Coulombic repulsion between pairs of electrons in their instantaneous rather than average positions (correlation).

Because the N particles in the auxiliary system do not interact, the Schrödinger equation for this system reduces to N one-particle equations

$$\left\{ \frac{1}{2} \quad {}^{2} + V_{\mathrm{KS}} \right. \quad {}_{i} = \quad {}_{i} \quad {}_{i} \qquad i = 1, \ldots, N \tag{2.3}$$

to be solved self-consistently. By construction, the Kohn-Sham orbitals $_i$ give the correct total electron density:

$$n(\mathbf{r}) = \sum_{i=1}^{N} \quad {}_{i}(\mathbf{r}) \quad {}^{2} \; . \tag{2.4}$$

The total Kohn-Sham energy $E_{\mathrm{KS}} = {}_{i=1}^{N} \quad {}_{i}$ is a variational functional of $n(\mathbf{r})$, which can then be calculated by suitable variation of the trial electron density $n(\mathbf{r})$ to minimise E_{KS}. It is related to the true energy by[100]

$$E_{\mathrm{true}} = E_{\mathrm{KS}} \quad \frac{1}{2} \quad \frac{n(\mathbf{r})n(\mathbf{r}\ )}{\mathbf{r} \quad \mathbf{r}} \, d\mathbf{r} \, d\mathbf{r} \; + E_{\mathrm{xc}}[n(\mathbf{r})] \qquad \frac{E_{\mathrm{xc}}[n]}{n(\mathbf{r})} n(\mathbf{r}) \, d\mathbf{r} \; . \tag{2.5}$$

So far, this approach has been exact, and the only term for which an explicit recipe has not been given is the exchange-correlation functional $E_{\mathrm{xc}}[n]$. This is necessarily highly nonlocal and must be approximated if this line of analysis is to proceed further. The simplest possible approximation is to take the exchange-correlation energy at any point to be that of a homogenous electron gas with the same density throughout as found at that point. Although this is a fairly drastic approximation (Kohn and Sham themselves commented that they "[did] not expect [it to yield] an accurate description of chemical bonding"), it is surprisingly accurate, in part because it obeys the correct "sum law", with the exchange-correlation hole containing exactly one electron:[101]

$$n_{\mathrm{xc}}(\mathbf{r}, \mathbf{r} \quad \mathbf{r}) \, d\mathbf{r} \; = \quad 1 \; . \tag{2.6}$$

This is the basis of the *local density approximation*, often abbreviated LDA. More complex approximations take into account higher-order terms in the polynomial expansion of the electron density any given point, and are for this reason known as *generalised gradient approximations* (GGA).

The spin of the electron has conveniently been ignored in the above discussion. Since none of the Hamiltonians used in this thesis depend explicitly on the spin, its only relevance is in ensuring that the correct fermionic statistics are obeyed. As such, spin is modelled in these calculations simply by treating the spin-up and spin-down electron densities as independent variables which interact *via* the Coulomb potential.

2.2.3 The plane-wave pseudopotential approach

Despite the fact that the electron density rather than the wavefunction is the central quantity of density-functional theory, in the Kohn-Sham formalism the density is nonetheless represented as the sum of squares of one-electron orbitals, as shown above. In common with other computational electronic structure methods, DFT therefore requires a set of basis functions to represent these orbitals. A bewildering variety of basis sets, localised and non-local, are available; however, the CASTEP code used in this project uses a comparatively simple set in which each basis function is a three-dimensional plane wave.

To completely represent a general electron density in space, an uncountable number of plane waves are required. However, if we consider a periodic system such as an infinite crystal, by Bloch's theorem we need only consider wavevectors which are vectors of the reciprocal lattice, a countable set.[103] Thus, truncating the basis set at a suitable energy (or equivalently, wavenumber) makes this set finite and hence useable in numerical calculations.

The important features which differentiate a plane-wave basis set from alternatives are as follows:

First, the basis set is characterised by a single number, the energy cutoff, and therefore the only convergence check necessary is with respect to this single quantity. Moreover, unlike localised basis sets, a plane wave basis set is in principle complete, so that we can represent a wavefunction to any desired accuracy by choosing a suitably high energy cutoff.

Second, all space is modelled equally well, so it is not necessary to predict in advance the levels of representational accuracy required by different regions of space, and basis set superposition errors do not occur. (On the other hand, for identical reasons, vacuum is just as computationally expensive to model as regions with many atoms.)

Third, since this method relies upon periodic boundary conditions, it is particularly suitable for dealing with solid-state calculations. Indeed, because of the reliance on Bloch's theorem discussed above, plane wave basis sets are formally incapable of dealing with non-periodic systems, although in practice it is straightforward to perform gas-phase calculations by placing the molecule of interest in a large, artificial unit cell in such a way that the vacuum between periodic images prevents any interaction between them. (In the terminology of plane wave calculations, such a unit cell is often called a "supercell"; note however that this differs from the crystallographic "supercell", a collection of multiple copies of the lattice unit cell.)

Fourth, since plane waves, unlike localised basis functions, are entirely unphysical in that they bear no resemblance to any wavefunction found in a system of atoms, considerably more basis elements are needed than in calculations using localised basis sets. This requirement is compensated for in terms of computational efficiency by extremely efficient Fourier transformation algorithms, which permit rapid transformations between real and reciprocal space.

A further increase in computational efficiency arises from the fact that the Kohn-Sham wavefunctions will vary most near atomic nuclei, and hence require the highest-energy basis functions for an accurate representation there; on the other hand, the interactions of most significance in describing chemical bonding occur in the regions between nuclei. As such, if the core electrons and nucleus are replaced by a smoothly varying *pseudopotential*, chosen such that its eigenfunctions are identical to those of the true potential outside a given cutoff radius, the size of the basis set needed to accurately represent the system can drop dramatically.[104] Further gains are possible from the use of *ultrasoft* pseudopotentials.[105] These are made smoother by relaxing the constraint that the potential should integrate to the true core charge, which is compensated for by the addition of an "augmentation function". This formulation is particularly useful in cases such as $2p$ and $3d$ orbitals, which have no radial nodes, so that significant amounts of localised electron density must be retained if the norm is to be conserved. It typically enables the basis set cutoff to be around half that needed for a norm-conserving pseudopotential.[106]

2.2.4 *Excited states*

At this point it should be noted that density-functional theory is explicitly a ground-state theory. Certainly, it is possible to calculate virtual Kohn-Sham orbitals. However, the Kohn-Sham construction is formally only a mathematical representation of the *ground-state* electron density; thus in contrast to the case of the occupied orbitals, no part of the Hohenberg-Kohn theorem guarantees that these virtual orbitals model the system under consideration with any degree of accuracy.

In practice, however, the situation is less dire than the above analysis may make it appear: certainly, despite the lack of formal justification, it is not unusual to interpret virtual Kohn-Sham eigenstates as excited states of the system being modelled.[101] In particular, the relative energies of the excited states are often well described by the virtual orbitals. On the other hand, the energies of the excited states with respect to the ground state – that is, the band gap in insulators – are notoriously underestimated by calculations using the simplest possible density functional, the LDA.[107] This can be ameliorated by using more sophisticated functionals: for example, by combining the LDA or GGA correlation functionals with an "exact exchange" term. However, in practice this may not be necessary: often, the relative energies of the excited states are the crucial parameters of interest, and if necessary these can be related to the ground-state energy by a rigid shift, or "scissor operator", of magnitude determined by some other means.

An alternative approach to accessing some excited-state information is to artificially alter the total spin of the model system. As mentioned above, the spin-up and spin-down electrons are modelled as two separate populations. For a diamagnetic system such as those studied here, one would naturally set the total electronic spin to zero when modelling the ground state. However, it is trivial to “flip” one electron so that the total spin is 1, producing a triplet state; under these circumstances the “ground” state of the model system will correspond to the first triplet excited state of the system under investigation. This second approach is taken in the discussion of the excitation process in Section 5.4.3.

2.3 X-ray absorption spectroscopy

As discussed in the previous sections, single-crystal X-ray diffraction is an extremely powerful tool for investigating photoisomerism, allowing detailed models to be constructed while making few prior assumptions about the nature of the excitation. Nonetheless, this technique suffers from several disadvantages. It can only give indirect information (from coordination distances) on the partial oxidation state change expected upon photoisomerisation, which is an important property of these materials. It requires single crystals to be grown, which is not always possible. Even when these are available, the use of single crystals of optically dense compounds can lead to problems with poor optical penetration depth, and appropriate irradiation conditions may be difficult or impossible to achieve.

In the work described here, X-ray absorption spectroscopy (XAS) was performed in an attempt to overcome these restrictions. As the name suggests, this technique involves measuring the absorption of X-rays by the target sample in the region around an X-ray absorption edge – that is, in an energy range around that required to ionise a core electron from the target element. In the energy region immediately above the target edge, the ejected photoelectron is left with a very low kinetic energy, and hence backscatters from the surrounding atoms, returning to the originating atom in such a way as to influence the absorption probability itself.

XAS spectra can be roughly divided into X-ray absorption near-edge spectroscopy (XANES) and extended X-ray absorption fine structure (EXAFS) regions. In the XANES region, which immediately surrounds the edge, photoelectron energies are so low that special care must be taken to account for multiple scattering when predicting the absorption. The EXAFS region lies further above the edge, where single scattering paths usually dominate the observed absorption. The XANES region is directly sensitive to changes in oxidation state and coordination geometry, whereas the EXAFS region is sensitive to the local structure, particularly the bond lengths to the target atom's nearest neighbours.

XAS is a well-established technique which has previously been applied *in situ* to photomagnetic[108] and other photoinduced transitions in solids,[109] although no instances of its use to study photolinkage isomerism complexes appear to have been published. It has also been successful in probing ultrafast photoexcitation in liquids.[110,111]

2.4 Other techniques

Various other techniques have been used to study photoisomerism materials: these have included differential scanning calorimetry[16,39,55] and Mössbauer,[16] vibrational,[39,70] and optical spectroscopies.[112] The use of NMR spectroscopy has also been proposed, since this has successfully been applied in the solid state to studies of fast systems including photosynthetic bacteria.[113] Careful preliminary experiments, however, would be needed to determine what nucleus it would be best to focus on and which pulse sequence to use.

CHAPTER 3

PHOTOCRYSTALLOGRAPHIC EXPERIMENTS

> The citizens of Hobart have been long impressed with the fact that their city is none too brightly illuminated. Apart from supplementary electric lights placed in the central thoroughfares, the lighting system in present use does not do much more than make the darkness visible. Again, there are many new thoroughfares and by-ways which the march of improvement has called into existence where more light is absolutely necessary. . .
>
> – *The Mercury*, Monday, 3 July, 1905

3.1 Background

The advantage of studying the [Ru(SO_2)(NH_3)$_4$**X**]**Y** family is that changing the *trans* ligand **X** and counterion **Y** is chemically simple, but can result in a substantial change in the packing properties and hence crystal structures of these complexes. That said, not all **X**, **Y** pairs readily form single crystals.

A series of syntheses was attempted as summarised in Table 3.1: in brief, a variety of new components was combined with the "standard" counterions chloride and tosylate and *trans* ligand water. Of these, only compounds **1** (**X** = isonicotinamide, **Y** = tosylate) and **2** (**X** = water, **Y** = tosylate) yielded single crystals suitable for X-ray diffraction. The synthetic procedures developed for these compounds are presented in Appendix A.

Syntheses of several compounds in which the equatorial NH_3 ligands were replaced by bi- or tridentate *N*-donor ligands were also conducted; however, attempts to grow single crystals of these complexes were unsuccessful. During this process, single crystals of the novel complex [Ru(HSO_3)$_2$(CO)(terpyridine)] were inadvertently formed. As this compound does not appear in the Cambridge Structural Database, its synthesis and crystallographic details are

Table 3.1: Summary of synthesis attempts made in terms of **X** and **Y**. Red squares represent syntheses that successfully yielded crystals suitable for X-ray diffraction. Blue dots indicate attempted syntheses that failed to yield crystals suitable for X-ray diffraction. Black circles denote previously known compounds.

	X													
Y	water	chloride	pyridine	3-phenylpyridine	4-phenylpyridine	3-benzylpyridine	4-benzylpyridine	3-picoline	4-picoline	3-chloropyridine	isonicotinamide	thioisonicotinamide	4-mercaptopyridine	3-pyridinesulfonicacid
chloride		○	●	●	●	●	●	●	●	●	●	●	●	●
tosylate	○			●	●		●		●		■	●		●
sulfanilate	●													
2,4-dinitrobenzenesulfonate	●													
3-aminobenzenesulfonate	●													
3-pyridinesulfonate	●													●
4-chlorobenzenesulfonate	●													
1-naphthalenesulfonate	●													
4-amino-1-naphthalenesulfonate	●													
( )-camphor-10-sulfonate	■										●			
1*S*-camphor-10-sulfonate	●													
4-cyanobenzoate	●													

presented in Appendix C.

This chapter reports the ground and metastable state structures of compounds **1** and **2**, obtained through a series of experiments using synchrotron and laboratory sources.

3.2 Experimental procedure

3.2.1 *Synchrotron experiments*

Single-crystal X-ray diffraction data were collected on beamline I19 at Diamond Light Source, using radiation of wavelength 0.68890(14) Å, a Crystal Logic 4-circle kappa goniometer, and a Rigaku Saturn 724+ CCD detector. The temperature was controlled by nitrogen flow from an Oxford Cryosystems Cryostream Plus. Data were collected from 12 -scans, each containing around 200 frames of width 0.5 . Each frame was collected over 0.5 s.

3.2.2 *Laboratory experiments*

Single-crystal X-ray diffraction data were collected using a Rigaku diffractometer equipped with Saturn 724 CCD detector, AFC-Kappa four-axis goniometer, and SHINE optics. Mo *K* radiation (= 0.71075(2) Å) was generated from a 3 kW sealed tube. The temperature was controlled by nitrogen flow from an Oxford Cryosystems Cryostream Plus. Data were collected from a series of -scans (5 scans for compound **1**, 2 scans for compound **2**), each containing 60 to 260 frames of width 0.5 . Each frame was collected over 20 s.

3.2.3 *Photoexcitation procedure*

For each sample, the collection procedure was as follows: first, a crystal was mounted and flash-cooled to 100 K in the dark, and a full structure determination was performed. Next, the crystal was irradiated *in situ* for two hours. Broadband, unpolarised light was delivered *via* an optic fibre to a lens, which focused it to a spot of approximate diameter 0.5 mm. The apparatus was adjusted by hand to situate the focal point as close to the mounted crystal as possible. The radiation sources used were a 270 W Jobin Yvon tungsten-halogen lamp (for compound **1**; see figure 3.1(a)) and an Ocean Optics PX-2

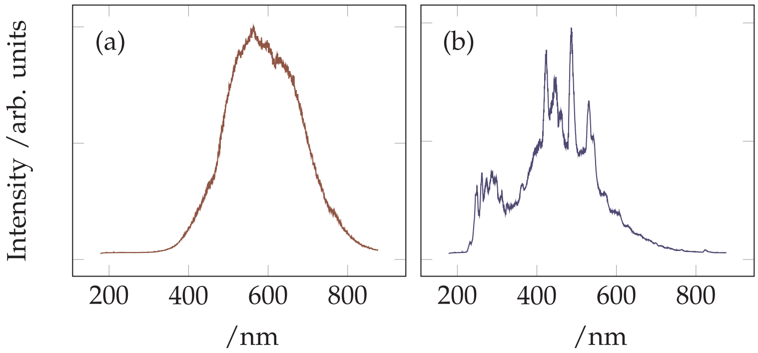

Figure 3.1: Spectra of (a) the tungsten-halogen lamp and (b) the xenon lamp used to irradiate the samples.

pulsed xenon lamp operating at *ca* 10 W, delivering 5 µs pulses at a rate of *ca* 100 Hz (for compound **2**; see figure 3.1(b)). Previous experiments have shown that the photoexcitation process is relatively insensitive to the spectrum of the light source provided there is significant flux in the metal-ligand charge transfer band at 450 nm to 500 nm. The sample was rotated about the axis continually during irradiation, to ensure uniform exposure to the light. The irradiation setup is shown in Figure 3.2. Finally, the light source was removed and, after waiting 10 minutes to ensure the dissipation of any heat due to the irradiation, exactly the same collection of frames was performed as for the dark structure.

At the synchrotron, the temperature was subsequently raised in broad steps (of 25 K for compound **1**, 50 K for compound **2**) and data collection repeated once at each temperature until no further evidence for the excited states was observed. When repeating these experiments in the lab, the temperature was raised in a single step at 300 K hr^{-1} to a given final temperature, and the data collection repeated at that temperature until no further change in the structure was observed.

3.2.4 *Data processing*

The data were integrated, reduced, and the Lorentz, polarisation, and absorption corrections applied using D*TREK as implemented within CRYSTALCLEAR 1.4.0;[114] they were subsequently scaled, merged, and sorted using XPREP.[115]

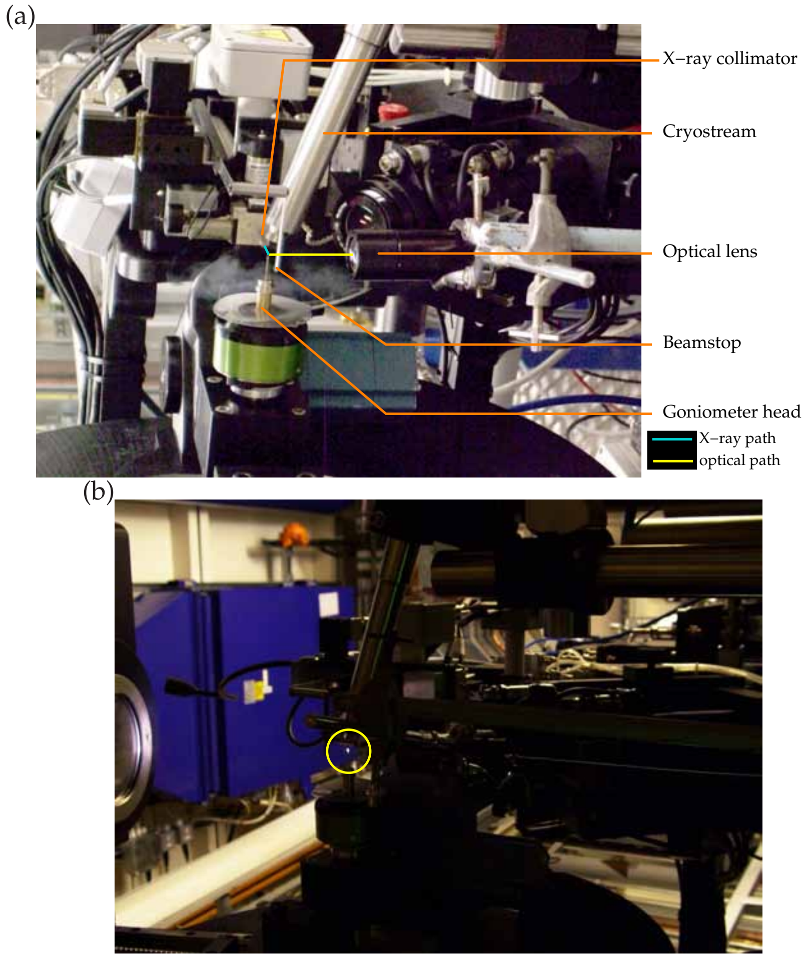

Figure 3.2: Experimental apparatus for irradiating the crystal *in situ*: (a) setting up; (b) during irradiation: the light shining on the crystal is emphasised. Note that for convenience both images have been rotated by 90°.

The dark structures were solved by direct methods using SIR92[116] and all structures refined using SHELXL-97,[117] both programs as implemented within WINGX 1.70.01.[118]

The structures after irradiation were solved by refining the dark model against the excited-state data, allowing both ground and metastable state parameters (including occupancy and ADPs) to refine independently. Treating the ground state model as a collection of rigid bodies able only to translate and rotate, as recommended in previous work (using smaller data sets from laboratory instruments),[84] made no significant difference to the parameters of interest. In particular, the excited-state occupancies did not vary within

Table 3.2: Crystallographic details common to all structural refinements.

compound	**1**	**2**
X	isonicotinamide	water
Y	tosylate	( )-camphorsulfonate
Formula	$RuC_{20}H_{32}O_9N_6S_3$	$RuC_{20}H_{44}O_{11}N_4S_3$
M /g mol^{-1}	697.77	713.84
Crystal system	triclinic	monoclinic
Space group	$P\bar{1}$ (no. 2)	$C2/c$ (no. 15)
Z	4	8
Z	2	1

experimental error. The excited positions of the SO_2 groups were identified as peaks in the Fourier difference map: this was relatively straightforward as these positions do not overlap any atom in the ground-state structure.

3.3 Ground-state structures

The structure of compound **1** was solved in space group $P\bar{1}$. Interestingly, it contains two crystallographically independent photoexcitation centres (*i.e.*, $Z\ = 2$), which will be labelled `Ru01` and `Ru51`. As a result, the metastable-state geometries and populations achieved at these sites are formally independent but, within a given experiment, result from the same excitation conditions. This allows direct comparison between the excitation achieved at the two centres, which is explored further in Chapter 5.

The structure of compound **2** was solved in space group $C2/c$. In this structure, $Z\ = 1$, but, as there are two camphorsulfonate counterions in the molecular formula, there are nonetheless two camphorsulfonate sites in the crystal structure. Of these, one is chiral, occupied by only one enantiomer of the camphorsulfonate ion – although of course every such site is mapped by the c glide plane into an equivalent site of opposite chirality, so that the overall structure is achiral. The other site, however, is disordered, occupied by an equal proportion of each enantiomer. Weak restraints were applied to make the atomic displacement parameters (ADPS) approximately isotropic, the bonds approximately rigid (*i.e.*, in pairs of bonded atoms, the components of the ADPS parallel to the bond were restrained to be equal), and equivalent bond lengths and 1,3-distances in the two structures the same. These conditions

Table 3.3: Selected crystallographic details which change with irradiation for compound **1**. All data are collected at 100 K. The columns represent, in turn: the dark structure; data in which only MS2 and GS are present; data in which MS1, MS2 and GS are present, refined against a model including only MS2 and GS; the same data as the previous column, refined against a full model; and the best available laboratory data for comparison.

Run	dark	**1**.3	**1**.1	**1**.1	**1**.2
Source	synchrotron	laboratory	synchrotron	synchrotron	laboratory
Model	full	MS2 only	MS2 only	full	full
a /Å	14.142(7)	14.148(12)	14.135(5)	14.135(5)	14.176(9)
b /Å	15.275(8)	15.297(12)	15.228(6)	15.228(6)	15.271(11)
c /Å	15.590(7)	15.525(12)	15.550(5)	15.550(5)	15.591(10)
/	110.254(4)	110.019(6)	110.349(4)	110.349(4)	110.130(7)
/	99.6330(10)	99.864(7)	99.772(4)	99.772(4)	99.647(7)
/	110.128(8)	109.782(7)	109.693(5)	109.693(5)	109.821(9)
V /Å^3	2805(2)	2810(4)	2794.2(17)	2794.2(17)	2823(3)
Measured reflections	87108	29968	87391	87391	28299
Unique reflections	16787	11428	16762	16762	11377
Restraints	0	264	170	566	524
Parameters	715	786	793	850	840
R_{int}	0.0250	0.0726	0.0251	0.0251	0.0664
R (F, $I > 2$)	0.0320	0.0987	0.0359	0.0350	0.0916
R (F, all)	0.0329	0.1162	0.0369	0.0360	0.1051
$wR2$ (F^2, $I > 2$)	0.0801	0.2270	0.0906	0.0844	0.1631
$wR2$ (F^2, all)	0.0806	0.2548	0.0912	0.0850	0.1719
S	1.119	1.138	1.151	1.104	1.180
highest peak /e Å^{-3}	1.027	1.161	1.174	0.859	0.780
deepest hole /e Å^{-3}	1.010	1.422	1.007	0.992	1.214
(MS2, `Ru01`A)	0	0	0.096(8)	0.078(6)	0
(MS2, `Ru01`B)	0	0.052(9)	0.030(5)	0.052(4)	0.027(8)
(MS2, `Ru01`C)	0	0.102(4)	0.047(6)	0.052(5)	0.133(4)
(MS1, `Ru01`)	0	0	0	0	0.038(5)
(MS2, `Ru51`D)	0	0.226(15)	0.239(4)	0.207(3)	0.253(4)
(MS2, `Ru51`E)	0	0	0	0.042(2)	0.114(9)
(MS2, `Ru51`F)	0	0	0	0.042(3)	0

Table 3.4: Selected crystallographic details which change with irradiation for compound **2**. All data are collected at 100 K. The columns represent, in turn: the dark structure; data in which no MS1 is present; data in which MS1 is present, refined against a model without this state; the same data as the previous column, refined against a full model; and the best available laboratory data for comparison.

Run	dark	**2**.5	**2**.1	**2**.1	**2**.4
Source	synchrotron	laboratory	synchrotron	synchrotron	laboratory
Model	full	MS2 only	MS2 only	full	full
a /Å	33.915(7)	33.99(2)	33.949(7)	33.949(7)	33.82(2)
b /Å	14.571(3)	14.654(10)	14.633(3)	14.633(3)	14.735(10)
c /Å	12.300(3)	12.456(8)	12.372(3)	12.372(3)	12.474(9)
/	90	90	90	90	90
/	97.11(3)	97.479(12)	97.09(3)	97.09(3)	97.480(13)
/	90	90	90	90	90
V /Å^3	6032(2)	6151(7)	6099(2)	6099(2)	6163(7)
Measured reflections	92602	18904	97071	97071	19076
Unique reflections	11282	6246	9304	9304	4376
Restraints	317	356	215	522	522
Parameters	504	532	533	561	561
R_{int}	0.0389	0.0753	0.0522	0.0522	0.0834
R (F, $I > 2$)	0.0413	0.1064	0.0632	0.0649	0.1033
R (F, all)	0.0437	0.1193	0.0643	0.0660	0.1346
$wR2$ (F^2, $I > 2$)	0.1166	0.1865	0.1241	0.1310	0.1833
$wR2$ (F^2, all)	0.1256	0.1945	0.1248	0.1318	0.2045
S (restrained)	1.155	1.110	1.248	0.801	1.045
highest peak /e Å^{-3}	1.041	0.681	1.620	1.591[a]	0.777
deepest hole /e Å^{-3}	0.966	0.857	1.205	1.267[a]	0.826
(MS2)	0	0.106(12)	0.114(6)	0.098(6)	0.122(11)
(MS1)	0	0	0	0.031(4)	0.132(8)

[a] These comparatively high figures represent Fourier ripples around the Ru atom from high-resolution synchrotron data. When the data are truncated at 0.85 Å, to match laboratory work, the highest peak and deepest hole shrink respectively to 0.89 e Å^{-3} and 0.55 e Å^{-3}.

were not necessary to obtain a stable, sensible refinement against the "dark" data, but they were included for consistency with the "light" refinement, where they proved helpful.

In both compounds, there was some evidence for rotational disorder of the sulfonate groups on the counterions; this varied between samples. A split-atom model of these moieties was used where appropriate.

The major crystallographic parameters for the "dark" and "light" structure determination are presented in Tables 3.2, 3.3, and 3.4; full details can be found in Appendix B.

3.4 Preliminary metastable-state analysis

Upon irradiation, the cell parameters did not change markedly (Tables 3.3 and 3.4). This is perhaps unsurprising given the successful data collection, since crystal shape changes are the result of internal strain which can also result in crystal cracking[84] or loss of long-range order and hence high-angle data,[119] although substantial photoinduced crystal shape changes are certainly known.[81]

When a ground-state model was refined against the data collected after irradiation at 100 K, peaks in the Fourier difference maps for both compounds revealed a non-zero MS2 population. These maps are calculated by subtracting the modelled electron density from that reconstructed from the observed structure factors. When the majority of the structure – here, the ground state – has been correctly modelled, almost all the phases will be correct. This is especially likely to be true in a centrosymmetric space group, where only two phases (0 and) are possible. Thus residual electron density not accounted for in the model can be accurately located.

It was immediately apparent that the metastable state populations achieved varied markedly between experiments. Every attempt was made to keep the irradiation conditions as similar as possible; nonetheless, some variation occurred in the focusing of the lamp (and hence the intensity delivered to the crystal), the orientation of the crystal with respect to both the lamp and the axis, and the crystal size. All discussion of metastable state data will be labelled with a run number: *e.g.*, run **2**.1 is the first excitation experiment on compound **2**. These numbers can be cross-referenced against the crystallographic data in Table 3.7 and Appendix B.

A fractional MS2 population was added with atomic positions initially set to the peaks in the Fourier difference map (Figure 3.3); this gave a stable refinement. However, peaks substantially above background remained in the Fourier maps at the centre of the ground-state SO$_2$ groups at `Ru51` in compound **1** and in compound **2** (Figure 3.4). Moreover, multiple-temperature analysis of the excited compounds gave anomalous results. It was expected that the MS2 populations should gradually decrease with increasing temperature, due to the state's decreased stability. However, in both compounds the population

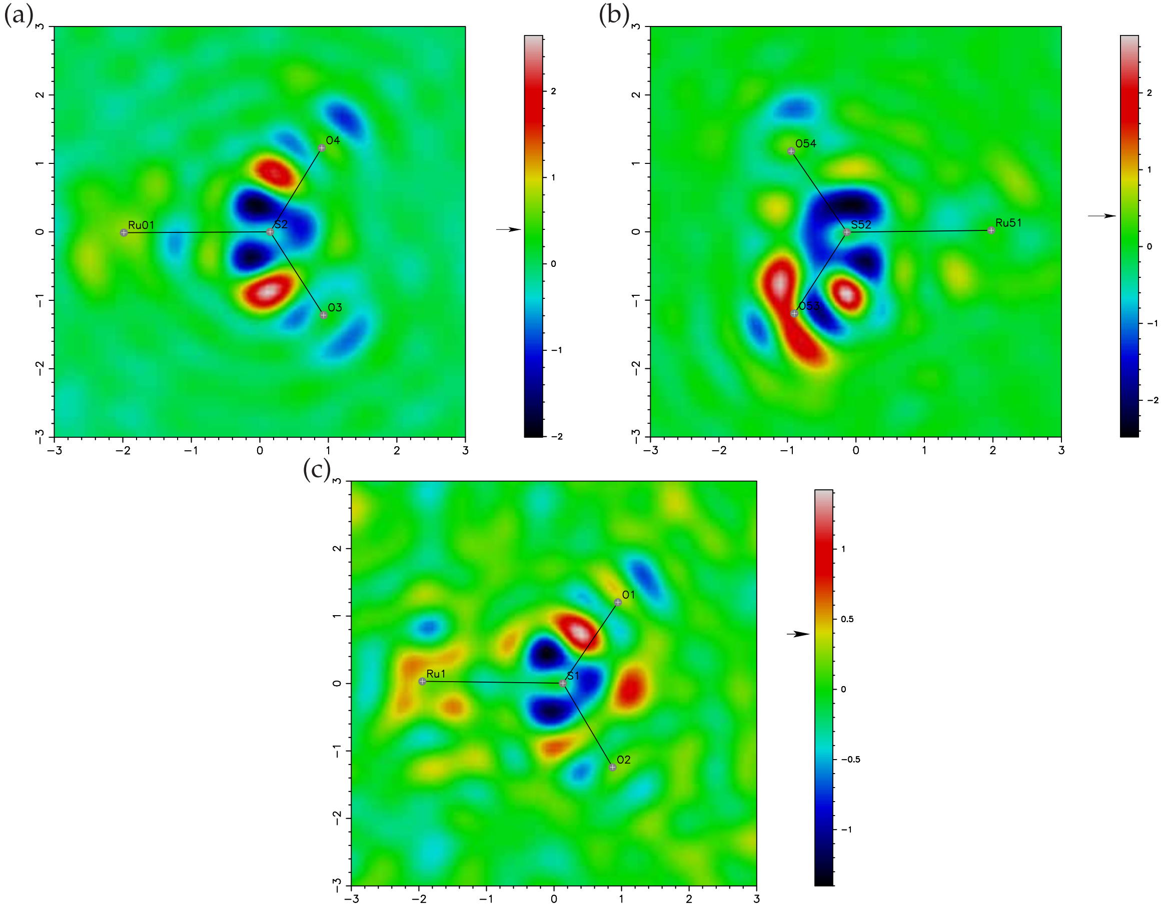

Figure 3.3: Fourier difference maps for compound **1**: (a) site `Ru01`, (b) site `Ru51`; and (c) compound **2** based on models including only ground-state components. In all three maps the troughs around the ground-state atoms and nearby peaks in the correct locations for a side-bound linkage indicate a significant MS2 population. In particular, the new S atom sites are clearly visible as the highest residual density peaks (two sites in (a), one each in (b) and (c)). For both compounds, synchroton data are taken from the respective runs 1. The position of the ground-state $RuSO_2$ group is indicated for reference. Length scales are in Å, colour scale in e Å^{-3}. For ease of comparison between the different colour scales, the colour corresponding to 0.4 e Å^{-3} is indicated with an arrow on the legend of each map.

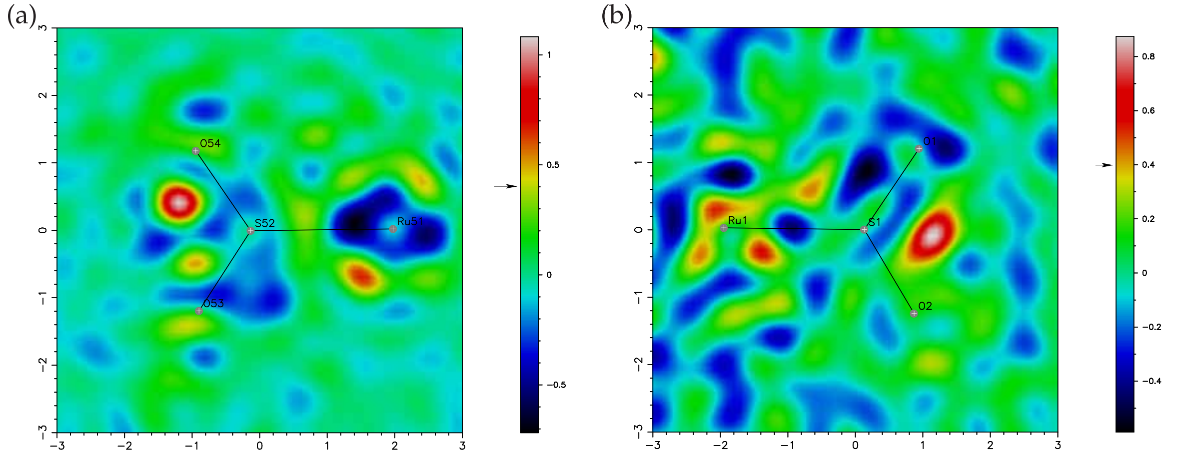

Figure 3.4: Fourier difference maps for (a) compound **1**, site `Ru51`, and (b) compound **2** based on models including only GS and MS2 components. Two MS1 S atoms are clearly visible in (a) and one in (b). In both cases synchroton data are taken from the respective runs 1. The position of the ground-state $RuSO_2$ group is indicated for reference. Length scales are in Å, colour scale in e Å^{-3}. For ease of comparison between the different colour scales, the colour corresponding to 0.4 e Å^{-3} is indicated with an arrow on the legend of each map.

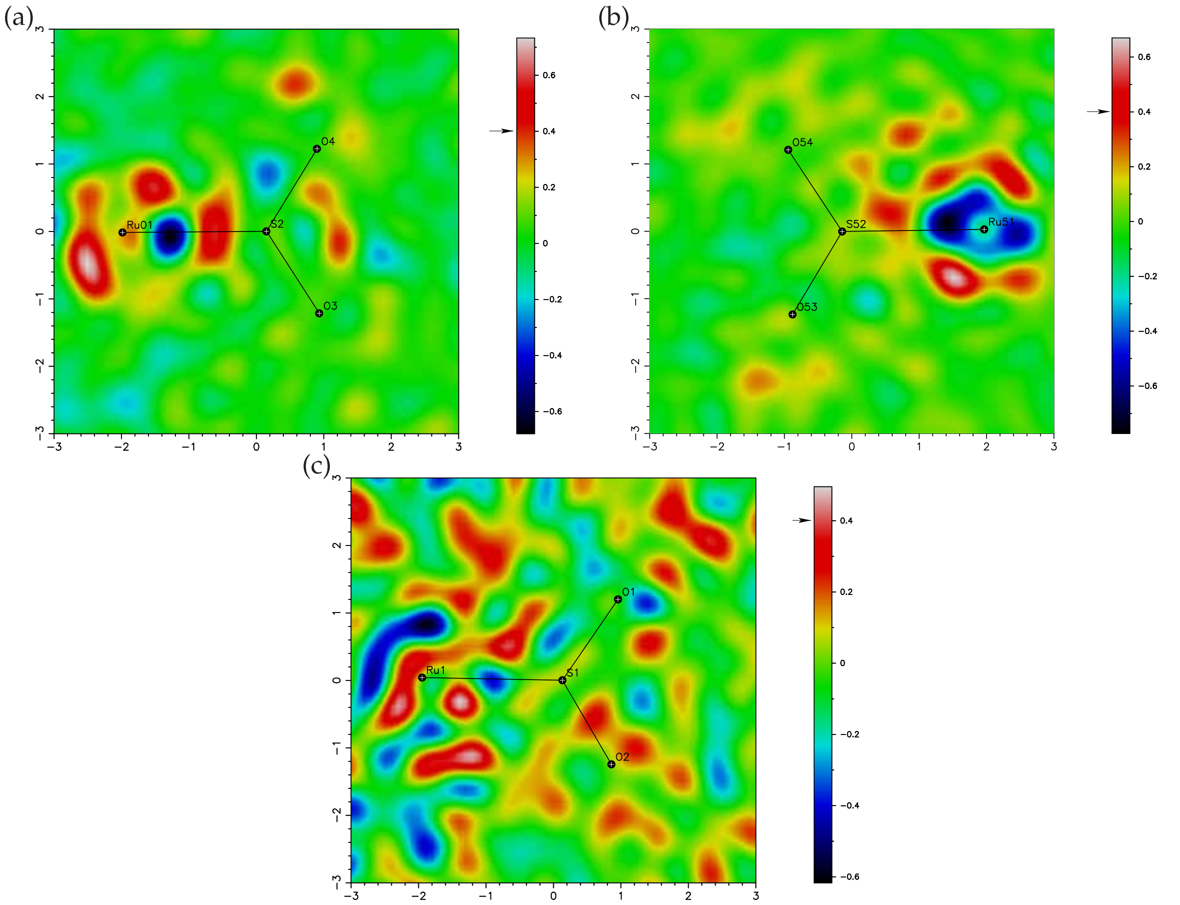

Figure 3.5: Fourier difference maps for compound **1**: (a) site `Ru01`, (b) site `Ru51`; and (c) compound **2** based on the final complete models. The maps are in general featureless apart from obvious Fourier ripples; a peak that could conceivably be due to an MS1 S atom is visible at `Ru01` (a), but this was not sustainable in a refinement. For both compounds, synchroton data are taken from the respective runs 1. The position of the ground-state $RuSO_2$ group is indicated for reference. Length scales are in Å, colour scale in $e\,Å^{-3}$. For ease of comparison between the different colour scales, the colour corresponding to $0.4\,e\,Å^{-3}$ is indicated with an arrow on the legend of each map.

increased to a maximum before decreasing again. Most prominently, at site `Ru51` in compound **1**, the population increased by 10% (Figure 3.6(a)).

To resolve these problems, the experiment was repeated multiple times using a laboratory source. Analysis of these data revealed that the peaks observed in the difference maps are in fact S sites in MS1, the O-bound metastable state, which has hitherto only been observed at 13 K.[71] Accordingly, MS1 was incorporated into the refinement model. This demonstrated that the unexpected increase in population with temperature results from the presence of MS1, which decays into the more stable MS2. Thus the data presented in Figure 3.6(a) are in fact better modelled as in Figure 3.6(b). The Fourier difference maps calculated from the final model are presented in Figure 3.5.

As an example of the effect of the changed model, the third and fourth columns in Tables 3.3 and 3.4 compare models fitted to the same synchrotron data with and without allowance for MS1. These models are further discussed in Chapter 4, in which the inclusion of MS1 is justified by the Bayesian analysis presented there; this conclusion is pre-empted by the substantial improvement in the crystallographic statistics for the "full" model. Note that the effect of including MS1 is in some cases to diminish the apparent population of MS2; this is partly a consequence of the constraint that the total SO_2 population should be 100% and partly due to the proximity of the *Ru*-bound O atom in MS1 to the S atom in MS2, so that some electron density is reattributed from MS2 to MS1. Indeed, the troughs visible in Figure 3.4 suggest that the MS2 S atoms have too high a population in these models.

Before the multiple-temperature data can be discussed further, the revised model for the metastable states generated at 100 K must be presented.

3.5 Revised metastable-state structures

The complete models for the "light" structures are shown in Figures 3.8 and 3.9, with parameters tabulated in Tables 3.2, 3.3, and 3.4 and in Appendix B. The uncertainties in metastable state populations indicated in these tables originate directly from the least-squares analysis; they are thus known to be too small, since they do not take into account off-diagonal terms in the restraints matrix, which will be significant due to the high correlation between, for example, the

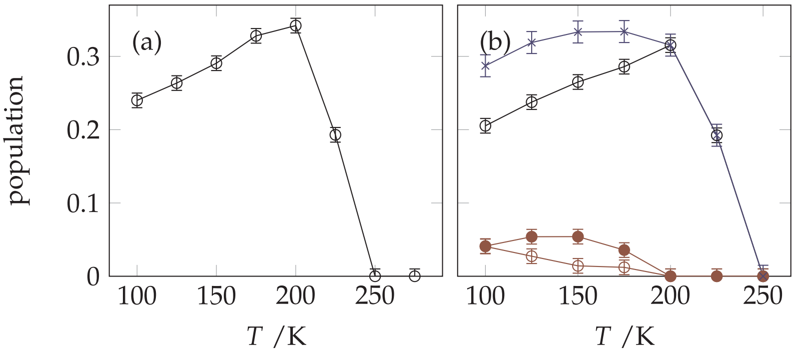

Figure 3.6: Population of metastable states at `Ru51` in compound **1** as a function of temperature. (a) A preliminary model including only MS2 (black circles), in which the MS2 atoms are modelled isotropically, shows a substantial rise in population over the range 100 K to 200 K. (b) A complete model also including two geometries of MS1 (red circles and dots), with full anisotropic refinement under appropriate restraints, yields a more reasonable total metastable population (blue crosses). Note, however, that there is still a small rise in population at low T: see discussion in text.

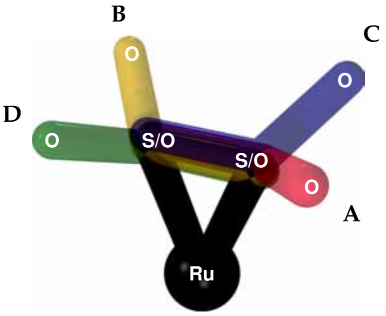

Figure 3.7: Schematic of the four possible MS2 geometries, labelled **A**–**D**. For full discussion, see Chapter 5.

ADPs and the occupancy fractions. Where more realistic values are required they are estimated. Further comment on the reliability of refining occupancy fractions can be found in reference 90. Despite the hazards of simultaneously refining ADPs and occupancy, however, the excited-state atomic positions do not substantially overlap with the ground state, thus making this system easier to model than, for instance, NO complexes.

In compound **1**, the excitation observed varied substantially between the two Ru centres. If the orientation of the side-bound S O bond and the Ru O S O torsion angle are regarded as fixed, there are four possible MS2 geometries, which will be labelled **A–D** (Figure 3.7; see also discussion in

Chapter 5). At `Ru01`, three of these geometries were observed (Figure 3.8(a)), while at `Ru51` only one was initially generated (Figure 3.8)(c)). However, a second MS2 geometry was formed from the decay of MS1 when the temperature was raised to 175 K (Table 3.7). The reasons why only some plausible geometries were observed were explored using DFT calculations, which are reported in Chapter 5.

Synchrotron data showed two MS1 geometries at `Ru51` (Figure 3.8(d)) but none at `Ru01`. One laboratory run, however, allowed an MS1 geometry to be refined at `Ru01` (Figure 3.8(b)). MS1 geometries will be labelled **E** and, where necessary, **F**; however, unlike the labels **A–D** for MS2, these are intended neither to represent an exhaustive set of local energy minima, nor to be compared between runs of the experiment. The position of the S atom in MS1 at `Ru01` is clear, but those of the O atoms are somewhat uncertain, so that the model has an unusual shape compared to the higher-population model at `Ru51` and previous observations of this state (Table 3.5). In particular, the O S O angle is probably unreasonably small (*cf.* literature values 116 to 120 ; Table 3.5).

In compound **2**, a single MS2 and a single MS1 geometry were observed (Figure 3.9). Again, the position of the S atom in MS1 was always clear, while the O positions were not as obvious at small populations. Thus the synchrotron data gave a much wider O S O angle than expected (Table 3.5).

It is interesting to note that there are discrepancies between the MS1 geometries observed in these compounds and those previously reported in compound **4** at 13 K.[71] In particular, the Ru O bond length in all the present data is substantially longer than previously observed, while in compound **2** the S O bond lengths are shorter. As discussed above, some of these effects will be artifacts arising from modelling marginally small populations. For the 100 K data, no restraints were placed on the positions of the MS1 atoms, in order to demonstrate that the data provide evidence for this state rather than having it forced upon them. However, at higher temperatures, these restraints may be applied essentially without affecting the refinement statistics: as an example, in the 175 K data for run **1**.1, the S O bond lengths were very weakly restrained to 1.5 Å and the O S O angle to 120 . This is simply because, at this temperature and for this data set, unlike the S atom, the fractionally populated O sites are commensurate with the background noise level and can therefore move without substantially affecting the refinement. However, other data sets – models **1**.1 and **2**.4 in particular – appear to yield more trustworthy O positions. Further investigation of effects which may give rise to this discrepancy would therefore be interesting. By contrast, the MS2 geometries are in good agreement with those previously reported (Table 3.6).[69–71]

As shown in Tables 3.3 and 3.4, a large number of weak restraints were used to refine the "light" models. Most of these served to prevent the disordered regions of the crystal structure from refining to unphysical parameters as previously discussed. In the disordered regions, which include all SO_2 photoexcitation centres as well as the disordered camphorsulfonate site in compound **2**, the atoms were restrained to have approximately isotropic ADPs on which rigid-bond restraints were placed. Finally, atoms closer together than 1.7 Å were restrained to have identical ADPs, regardless of whether or not they belonged to the same disordered component. Some of these restraints have more physical significance than others. For instance, the rigid-bond condition is chemically likely to be approximately true, while nearby atoms in different disordered components are no likelier to have similar ADPs than any two atoms in the same crystal at the same temperature. The common aim of all these restraints, however, is to overcome the strong negative correlations between the ADPs of nearby atoms, which naturally arise since they represent electron density in the same region of space. In refinements without these restraints, some atoms are likely to become unphysically large and others correspondingly small.

In addition to these restraints on the ADPs, corresponding bond lengths and 1,3-distances were restrained to be approximately identical where the same molecule or moiety featured in multiple disordered settings: *i.e.*, wherever two or more MS1 or MS2 geometries were refined in a single model, and for the two molecules on the disordered camphorsulfonate site. In compound **2**, restraints were placed on the positions of the two hydrogen atoms on the *trans* water ligand; unlike the other hydrogen atoms in the molecule, they could not be placed automatically using idealised bond lengths, since they are not coplanar with the Ru O bond.

Finally, at site `Ru01` in compound **1**, which exhibits three MS2 geometries, the two atoms comprising the side-bound (^{2}) linkage were constrained to occupy the same positions regardless of which is sulfur and which oxygen – for instance, the sulfur atom in metastable geometry **A** occupies exactly the same position as an oxygen atom in geometry **B** (Figure 3.8). Although this constraint does not follow from bonding considerations in the gas phase, the electron clouds of these atoms overlap to such a considerable extent that they cannot meaningfully be resolved by these data, and attempting to do so renders the model unstable to an iterative refinement.

In order not to bias the refined model, it was decided not to place any restraints on the atomic positions based on prior information about the geometry of the metastable states. In fact, most of the restraints in these refinements are on the ADPs, but of the remainder, most restraints and constraints on atomic positions purely encourage internal consistency. Thus, although at first glance the number of restraints appears large, their effect is merely to prevent the refinement from collapsing into physically implausible minima, rather than to directly influence the important scientific parameters: namely, the geometry and population of the metastable states. Externally derived restraints may enable better refinements at very low populations, but, particularly for the case of high-temperature MS1, it would be unconvincing to introduce restraints based on other observations of this state before demonstrating that it is definitely present in the data obtained here.

3.6 Decay with temperature and time

The lifetime of the metastable states investigated in this study varies, as might be expected, with temperature. Previous time- and temperature-resolved work on compound **4** using IR spectroscopy has shown that MS2 in this compound obeys first-order Arrhenius kinetic behaviour over the temperature range 255 K to 280 K. Extrapolating to room temperature would give a half-life of 78 s at 300 K,[70] although preliminary results obtained in our group indicate that first-order kinetics may not persist in this temperature range, with the

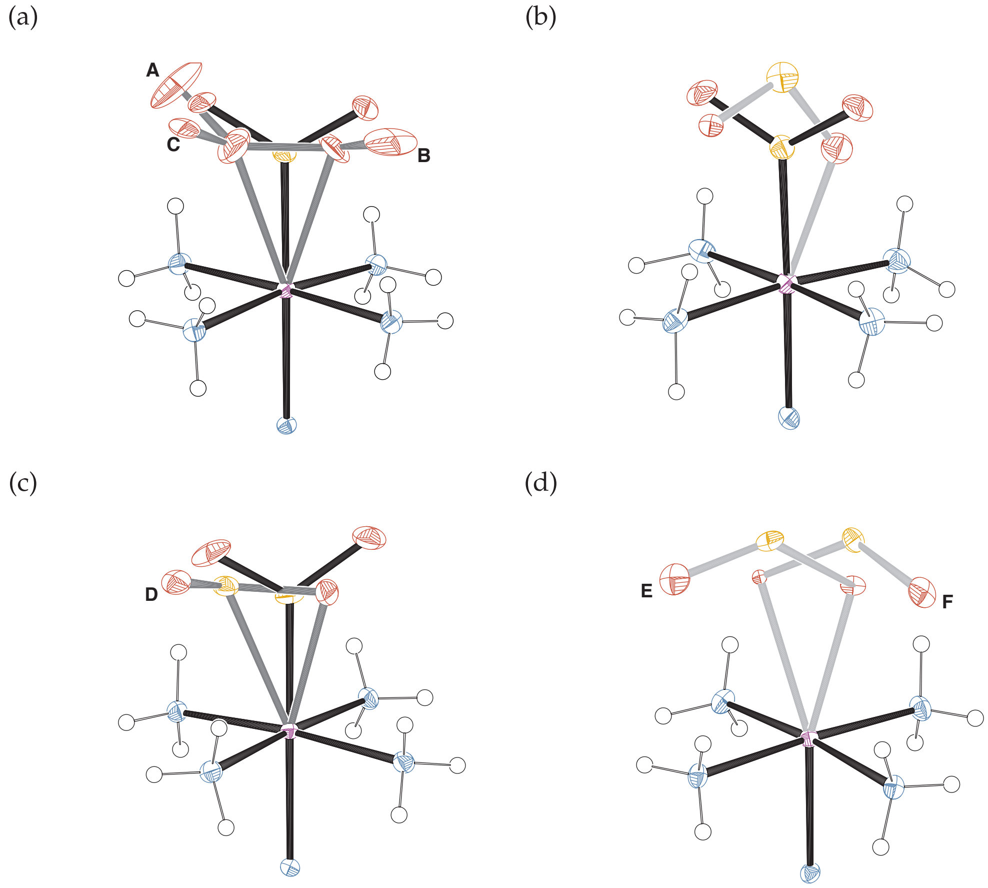

Figure 3.8: "Light" model for compound **1**. Ru atoms are shown in purple, S in yellow, O in red, N in blue, and H in white. Ground-state bonds are shown in black, MS1 (*O*-bound) in light grey, and MS2 (^{2}-bound) in dark grey. For clarity, only the Ru-bound N atom of the isonicotinamide ligand is shown. Unless otherwise stated all diagrams are based on synchrotron data from run **1**.1. Site `Ru01`, (a) full model; (b) data from laboratory run **1**.2 showing MS1 at this site. The positions of the O atoms are somewhat dubious; see discussion in text. Site `Ru51`: (c) ground-state and MS2 components; (d) MS1 components.

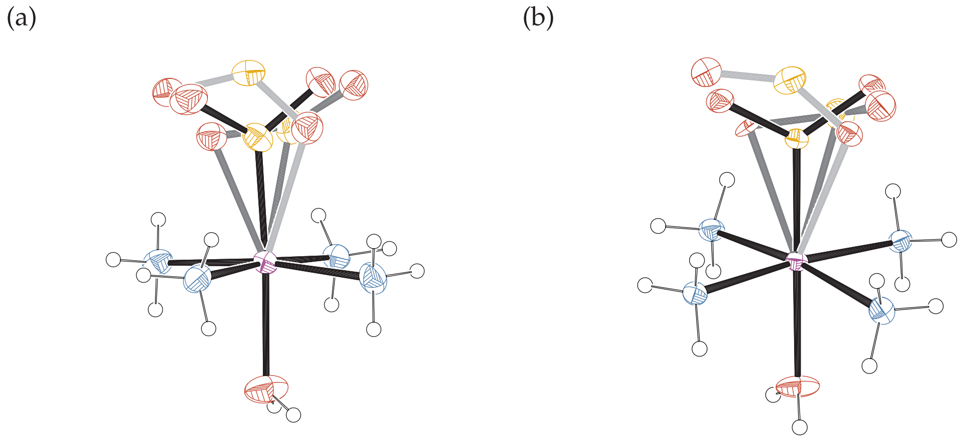

Figure 3.9: “Light” model for compound **2**. Ru atoms are shown in purple, S in yellow, O in red, N in blue, and H in white. Ground-state bonds are shown in black, MS1 (*O*-bound) in light grey, and MS2 (^{2}-bound) in dark grey. (a) Laboratory data from run **2**.4, which had the highest population of MS1 of all data obtained. (b) Synchrotron data from run **2**.1; the lower population of MS1 here makes especially the oxygen atom positions in this state less reliable.

Table 3.5: Geometric parameters for observed MS1 states. These are compared to the same state as reported in the literature and to stable literature examples of O-bound SO_2. Bond lengths are denoted d, angles , torsion angles . All data are reported at 100 K unless otherwise stated.

Structure	d(M O)	d(O$_{bound}$ S)	d(S O$_{free}$)	O S O	(Ru O S O)
1.1, `Ru51E`	2.38(4)	1.55(3)	1.53(3)	131(2)	0(4)
1.1, `Ru51F`	2.40(17)	1.55(3)	1.55(3)	126(2)	22(15)
1.2, `Ru01`	2.23(16)	1.50(9)	1.37(6)	102(5)	19(16)
2.4	2.34(9)	1.33(8)	1.36(11)	124(6)	9(8)
2.1	2.50(10)	1.27(10)	1.32(15)	144(8)	32(16)
4, 12 K[71]	1.923(11)	1.514(10)	1.426(15)	116.2(8)	2[a]
SbF_5 OSO, ambient[120]	2.13[a]	1.45[a]	1.28[a]	119.2[a]	
$[Mn(OPPh_3)_4(OSO)_2]I_2$, ambient[121]	2.282(4)	1.448(4)	1.410(6)	116.2(4)	

[a] No error quoted.

Table 3.6: Geometric parameters for observed MS2 states. These are compared to the same state as reported in the literature and to stable literature examples of ^{2}-bound SO_2. Bond lengths are denoted d, angles , torsion angles . All data are reported at 100 K unless otherwise stated.

Structure	d(M S)	d(M O)	$d(O_{bound}$ S)	d(S O_{free})	O S O	(Ru O S O)
1.1, `Ru01A`	2.406(6)	2.337(7)	1.485(12)	1.383(12)	126.6(12)	125.(2)
1.1, `Ru01B`	2.337(7)	2.406(6)	1.485(12)	1.410(12)	122.7(11)	116.(2)
1.1, `Ru01C`	2.406(6)	2.337(7)	1.485(12)	1.392(12)	124.8(10)	123.9(18)
1.1, `Ru51D`	2.439(4)	2.229(15)	1.501(12)	1.422(8)	121.1(7)	108.6(5)
1.1, `Ru51B`[a]	2.45(3)	2.34(9)	1.41(8)	1.46(6)	135.(5)	92.(6)
2.1	2.490(18)	2.39(3)	1.45(4)	1.38(4)	113.(2)	109.(2)
4, 90 K[70]	2.365(8)	2.08(2)	1.49(2)	1.44(2)	127.(1)	101.3[b]
Ambient-temperature data:[122]						
$[Rh(NO)(SO_2)(PPh_3)_2]$	2.326(2)	2.342(5)	1.493(5)	1.430(5)	115.1(4)	100.3(3)
$[RuCl(NO)(SO_2)(PPh_3)_2]$	2.337(2)	2.144(6)	1.504(5)	1.459(5)	113.7(3)	110.3(3)
$[Mo(CO)_3(phen)(SO_2)]$[c]	2.532(3)	2.223(5)	1.468(5)	1.435(8)	117.3(4)	108.1(3)
$[Rh(CO)_2(bipy)(SO_2)_2]$[d]	2.496(2)	2.111(4)	1.550(4)	1.452(5)	113.4(3)	103.4(4)

[a] At 175 K, generated from the decay of MS1. [b] No uncertainty quoted. [c] phen = 1,10-phenanthroline. [d] bipy = 2, 2 -bipyridyl. Values quoted are the average of two SO_2 groups.

actual lifetime being shorter than this. It is clear in any case that at room temperature this state is not visible on the timescale of conventional Bragg diffraction techniques. Extrapolating downwards in temperature, on the other hand, gives the experimental result that this state persists indefinitely at 100 K.

The experiments in which the temperature was raised after excitation were originally intended to monitor the decay of MS2; however, they proved to give useful information about the decay of MS1 at lower temperatures. As shown in Table 3.7, the effect of raising the temperature was often to cause MS1 to decay to MS2. In one case (run **1**.1), this even produced an orientation of MS2 which was not originally observed after irradiation at 100 K; the different possible orientations of MS2 are discussed further in Section 5.5.

In many cases, the decrease in MS1 population is commensurate with an increase in MS2 population, giving remarkable agreement, well within experimental error, between the total (MS1 + MS2) metastable-state population at 100 K and a higher temperature. In other cases, however, the higher-temperature total photoinduced metastable occupancy is greater by up to about 3% than the 100 K figure. (In run **1**.3, at `Ru51` the increase is an exceptional 9%.) Consider, for instance, the multiple-temperature data presented in Figure 3.6; the inclusion of MS1 in the models mitigates the dramatic rise but does not account for it altogether. The most plausible reason for this is perhaps the presence of undetected MS1 geometries in small (3%) populations. It is generally accepted that it is difficult to detect metastable-state populations below a few percent;[123] indeed, in the present work, the repeated data collections at 120 K discussed below demonstrate empirically that below this level, it is very difficult to detect this state against a MS2 background (see the unphysical "kink" in the occupancy over time displayed in Figure 3.10). Other possible explanations exist: for instance, the excitation process could be slightly cooperative, so that Ru SO_2 groups near an MS2 site themselves have lowered MS2 energy with respect to the ground state, and upon warming transfer to this state. However, the conclusion that the increase in population on warming is due to unobserved MS1 states is plausible and consistent with these observations; this would therefore have to be thoroughly disproven before these data could be taken as evidence of cooperativity.

The data collected allow the timescale of MS1 decay to be roughly estimated (although the time-step involved is large, since the focus of these experiments was on collecting detailed structural information). In particular, run **2**.4, in which full data sets were repeatedly collected at 120 K after irradiation, shows the MS1 population slowly decaying before apparently dropping abruptly to zero as it passes below the threshold for successful modelling at t 8 hr (Figure 3.10, red). Only four data points were obtained before this threshold, so the exact form of the decay cannot be determined from these data. However, it seems reasonable to assume that, as for MS2, this state decays following first-order kinetics.[70] A decaying exponential was therefore fitted to the four non-zero MS1 populations at the final temperature; it corresponds to a half-life of 4.4(10) hr. We can assume, on the basis of the observations above, that the total MS population is constant over the entire experiment. Accordingly, the kinetic parameters determined from MS1 were then held constant while the total MS population was fitted to all MS2 population data at the final temperature – of which there are more since the data after the MS1 observation threshold can be used. This gave a good fit (Figure 3.10, blue) corresponding to a total MS population of 0.232(4); encouragingly, this is well within experimental error of the total MS population, 0.254(14), observed at 100 K (Table 3.7).

Similar data, albeit of poorer quality, could be obtained for MS1 at `Ru51` in run **1**.2 (Figure 3.10, inset). Here, only three points were available: the same analysis was performed for completeness, although a fit to so few points must clearly be viewed with caution. The best fit corresponded to a half-life of 8(2) hr and total population of 0.364(2) (compare the 100 K total 0.367(10)).

These results demonstrate that the lifetime of MS1 at 120 K is of the order of hours, so that this state is persistent within the timescale of a single-crystal diffraction experiments. Other experimental methods such as IR spectroscopy might allow the decay kinetics to be more accurately determined. However, previous DFT calculations suggest that the vibrational frequencies of MS2 and MS1 are very similar (symmetric stretch 934 $\mathrm{cm^{-1}}$ and 945 $\mathrm{cm^{-1}}$; antisymmetric stretch 1208 $\mathrm{cm^{-1}}$ and 1206 $\mathrm{cm^{-1}}$ respectively), so that high-resolution measurements would be needed to distinguish them.[70]

Table 3.7: Summary of excitation achieved under various conditions. Each pair of rows represents the same experiment on the same crystal, which was first irradiated at the lower temperature. A full data set was then collected before raising to the higher temperature and collecting another.

Run code	**Radiation**					**Population,**					**Temperature** /K
Compound 1		MS2 `Ru01A`	MS2 `Ru01B`	MS2 `Ru01C`	MS1 `Ru01`	total `Ru01`	MS2 `Ru51D`	MS1 `Ru51E`	MS1 `Ru51F`	total `Ru51`	
1.1	synchrotron	0.078(6)	0.052(4)	0.052(5)	0	**0.182(9)**	0.207(3)	0.042(2)	0.042(3)	**0.291(5)**	100(2)
		0.122(5)	0.078(4)	0.020(4)	0	**0.220(8)**	0.287(5)	0.018(3)	0.044(4)[a]	**0.349(7)**	175(2)
1.2	laboratory	0	0.027(8)	0.133(4)	0.038(5)[b]	**0.198(10)**	0.253(4)	0.114(9)	0	**0.367(10)**	100(2)
		0	0.053(8)	0.192(4)	0	**0.245(9)**	0.319(4)	0.057(8)	0	**0.376(9)**	120(2)
1.3	laboratory	0	0.052(9)	0.102(4)	0	**0.154(10)**	0.226(15)	0	0	**0.226(15)**	100(2)
		0	0.070(11)	0.091(4)	0	**0.161(12)**	0.295(15)	0	0	**0.295(15)**	140(2)
1.4	laboratory	0	0.044(7)	0.131(4)	0.020(5)[b]	**0.195(9)**	0.204(3)	0.094(7)	0	**0.298(8)**	100(2)
		0	0.070(8)	0.132(4)	0	**0.202(9)**	0.327(12)	0	0	**0.327(12)**	160(2)
Compound 2		MS2	MS1			total					
2.1	synchrotron	0.098(6)	0.031(4)[b]			**0.129(7)**					100(2)
		0.119(9)	0			**0.119(9)**					200(2)
2.2	synchrotron	0.037(3)	0.021(2)[b]			**0.058(4)**					100(2)
		0.072(4)	0			**0.072(4)**					150(2)
2.3	laboratory	0.102(11)	0			**0.102(11)**					100(2)
2.4	laboratory	0.122(11)	0.132(8)			**0.254(14)**					100(2)
		0.187(14)	0.071(7)			**0.258(16)**					120(2)
2.5	laboratory	0.106(12)	0			**0.106(12)**					100(2)
		0.100(11)	0			**0.100(11)**					140(2)
2.6	laboratory	0.095(10)	0			**0.095(10)**					100(2)
		0.125(12)	0			**0.125(12)**					160(2)

[a] This population refines to MS2 geometry B; see discussion in text.

[b] For these small populations the refined geometry is suspect; see discussion in text.

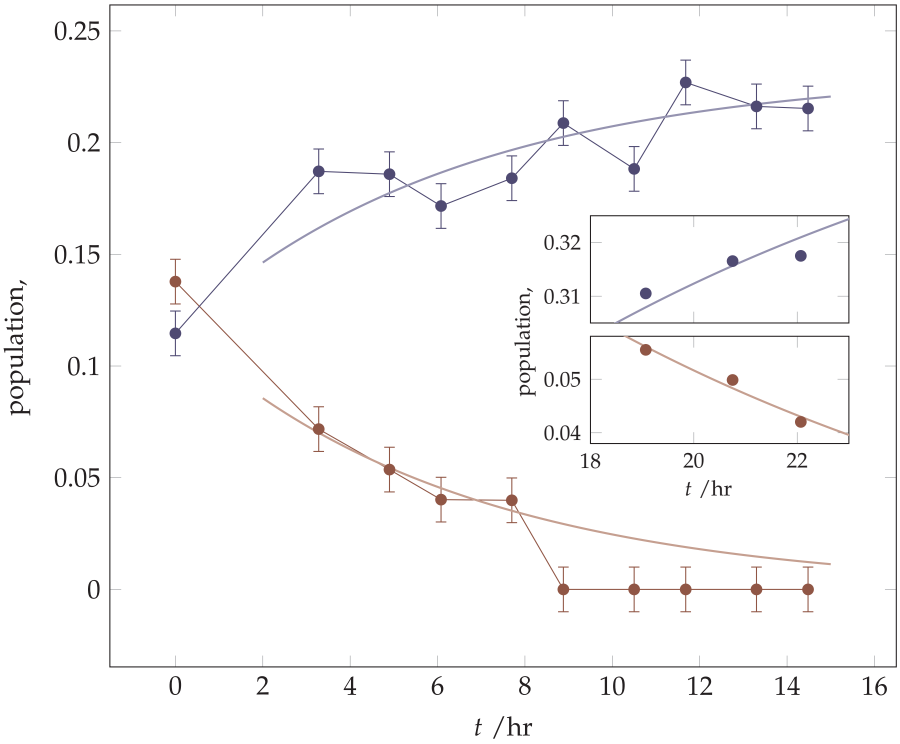

Figure 3.10: Population of metastable states (red: MS1; blue: MS2) in run **2**.4 as a function of time. The temperature was raised in a single step from 100 K to 120 K after the first ($t = 0$) data collection. The time attributed to each population is the midpoint of the relevant data collection. The red and blue lines are fits to first-order kinetics: see discussion in text. Inset: the equivalent data for run **1**.2.

CHAPTER 4

BAYESIAN ANALYSIS OF PHOTOCRYSTALLOGRAPHIC DATA

> Every judicious person will be sensible that the problem now mentioned is by no means merely a curious speculation in the doctrine of chances, but necessary to be solved in order to a sure foundation for all our reasonings concerning past facts, and what is likely to be hereafter.
>
> – Letter from Richard Price to John Canton, introducing Bayes' original paper on "inverse probability", 10 November, 1763

4.1 How do we know this is true?

In the previous chapter we have discussed crystallographic models involving as many as four metastable-state geometries coexisting at a single ruthenium centre. The question naturally arises whether, in introducing such a complex model, we are in fact over-fitting the available data. Indeed, the question of whether or not there is sufficient evidence to introduce a metastable geometry into the crystallographic model of "light" data is a particular case of a more general data-fitting problem well known in crystallography and across the sciences. Adding a new parameter to a model cannot increase the best-fit sum-of-squares statistic, and in practice invariably decreases it, regardless of whether or not the added parameter has any physical meaning.

Of course, a single sum-of-squares value is a rather crude measure of the goodness-of-fit of a given model, and experts in a field will have an intuitive sense of what a well-converged model looks like. For instance, in crystallography, large residual peaks in the Fourier difference density will be suspicious no matter how good the model's R factor. It is also possible to gain some appreciation for the accuracy of a particular refinement by generating theoretical data based on the model used, adding simulated experimental noise at an appropriate level, and then refining against the resulting "observed" intensities to see how accurately the original model can be reproduced.[90] This chapter, however, will examine the question of how big a drop in R (or equivalent change in other statistics) is required in order to be statistically significant.

The standard approach to this problem is to use an F-test, or a crystallographically convenient variation such as the $\mathcal{R}$-test.[124] These tests are applicable to *nested* models, in which the null model H_0 consists of a more general model H_1 with the addition of a linear hypothesis. That is, H_0 contains additional linear constraints compared to H_1, and therefore has fewer independent parameters. Hamilton, for instance, gives the example of comparing isotropic and anisotropic refinements, in which H_0, the isotropic model, consists of H_1, the anisotropic model, with the addition of the linear constraints that $U_{11} = U_{22} = U_{33}$ and $U_{12} = U_{13} = U_{23} = 0$ for all atoms (where (U_{ij}) is the atomic displacement tensor).[124] If q parameters are constrained in this way, and if H_0 is true, the best-fit likelihood ratio $L(H_0)/L(H_1)$ converges under certain conditions to a ^{2} distribution with q degrees of freedom as the number of data points goes to infinity.[125] Thus the hypothesis H_0 can be tested by comparing the observed likelihood ratio with a suitable ^{2} distribution. A statistic which is very unlikely under this distribution is interpreted as evidence against H_0.

An important technicality, however, has been glossed over in the discussion above. Among the "certain conditions" for the ^{2} distribution to be obtained is the topological requirement that the parameter set $_0$ of H_0 must be in the interior of the parameter set $_1$ of H_1 and that both must be open. In other words, if the null hypothesis H_0 is a boundary case of H_1, the likelihood ratio distribution is not guaranteed to converge to a ^{2} distribution, and the F- and $\mathcal{R}$-tests are inappropriate. In particular, in photocrystallographic experiments, among other parameters such as the locations of the atoms in the metastable state, the metastable state occupancy fraction is refined. Since H_0 has $= 0$ (*i.e.*, no metastable state present) and cannot be negative, the topological condition above is not met and Hamilton's $\mathcal{R}$-test should not be used.

This topological condition has recently been discussed in the astrophysics literature,[125] where analysis analogous to the above applies to the possible presence of a new peak in a spectrum. However, this result does not appear to be widely used in crystallography, perhaps because refinement from boundary cases in this way is comparatively rare. Certainly, it is not mentioned in the section on statistical significance tests in the International Tables for Crystallography.[127]

As a result of the topological criterion, a statistical test suitable to detect the presence of a metastable state must be sought elsewhere. One promising avenue is the field of Bayesian statistics, which have been applied to many aspects of crystallography,[128] and which have been suggested as a means to overcome the boundary-case problem in astrophysics.[125,129] Rather than calculating the probability that a null hypothesis is capable of explaining the observed data, these methods proceed by estimating the relative likelihood of two given models, given the observed data.

4.2 Theory

The following analysis follows the method of Gull,[130] as presented by Sivia.[132] The alternative models will now be labelled A and B to emphasise that, in this analysis, they are on an equal footing (or rather, the analysis can be weighted in either direction, if necessary, to reflect prior knowledge), unlike the tests discussed previously. To be precise, let A be the model with no metastable state present and B the model including some fraction of the metastable state. Thus B has more parameters than A; we will consider first the case where there is a single such parameter before generalising to multiple parameters.

The aim of this analysis is to estimate the ratio $\mathcal{P}(A\ D)/\mathcal{P}(B\ D)$ (where $\mathcal{P}$ denotes probability and D the observed data). Applying Bayes' theorem to numerator and denominator gives

$$\frac{\mathcal{P}(A\ D)}{\mathcal{P}(B\ D)} = \frac{\mathcal{P}(D\ A)}{\mathcal{P}(D\ B)}\ \ \frac{\mathcal{P}(A)}{\mathcal{P}(B)}\ . \tag{4.1}$$

The second term here reflects our relative belief in the two models irrespective of (prior to considering) the data. An agnostic position as to the success or failure of the experiment will be adopted by setting this ratio to 1.

To evaluate $\mathcal{P}(D\ B)$, the extra variable must be taken into account:

$$\mathcal{P}(D\ B) = \quad \mathcal{P}(D\quad ,B)\mathcal{P}(\quad B)\,\mathrm{d}\quad . \tag{4.2}$$

The first term in this integral is the probability of observing the data for a given value of . Approximating this by a Gaussian distribution centred on the best-fit value $_0$, with standard deviation estimated by the fitting procedure, yields

$$\mathcal{P}(D\quad ,B) = \mathcal{P}(D\quad _0,B)\ \exp\ \frac{(\qquad _0)^2}{2\ (\ )^2}\ . \tag{4.3}$$

The second term is the prior likelihood of the parameters . For simplicity this may be taken as constant over some range $_{\min} \approx \quad \approx \ _{\max}$. Provided that $_0$ lies comfortably within this range, the integral (4.2) evaluates to

$$\mathcal{P}(D\ B) = \frac{\mathcal{P}(D\quad _0,B)}{_{\max}\qquad _{\min}} \qquad \exp\ \frac{(\qquad _0)^2}{2\ (\ )^2}\ \ \mathrm{d} \tag{4.4}$$

$$= \frac{\overline{2}\quad (\ )}{_{\max}\qquad _{\min}}\ \mathcal{P}(D\quad _0,B)\ . \tag{4.5}$$

Generalising to the case of multiple parameters $= (\ ^1,\ ^2,\dots)$ gives

$$\mathcal{P}(D\ B) = \mathcal{P}(D\quad _0,B) \quad _i\ \frac{\overline{2}\quad (\ ^i)}{^i_{\max}\qquad ^i_{\min}}\ . \tag{4.6}$$

The assumption that the Gaussian is not severely truncated by the prior, so that the relevant integral is over the entire real line, is likely to hold for all parameters except the occupation fraction (*i.e.*, the edge case motivating this analysis in the first place). In this case, where the Gaussian may be truncated by the requirement that $\quad 0$, the integral is evaluated, still assuming that the right tail is not significantly truncated by the upper bound $_{\max}$, by

$$\mathcal{P}(D\quad _0,B) = \frac{\mathcal{P}(D\quad _0,\ \ _0,B)}{_{\max}\quad 0}\quad _0\ \exp\ \frac{(\qquad _0)^2}{2\ (\ )^2}\ \ \mathrm{d} \tag{4.7}$$

Under the standard assumptions for least-squares analysis (independent data and Gaussian noise), the probabilities of observing data D under the two models can be expressed in terms of the residuals of these models. The notation is intended to reflect that, once particular values of the parameters have been specified, these equations are identical for the two models.

$$\mathcal{P}\quad F_{\mathrm{o}}^2 \quad \overset{A}{\underset{0,\ \ 0,B}{}}\Big)\Big(= \frac{1}{\overline{2}\ \ (F_{\mathrm{o}}^2)}\ \exp\ \frac{(F_{\mathrm{o}}^2\quad F_{\mathrm{c}}^2)^2}{2\ \ (F_{\mathrm{o}}^2)^2} \tag{4.8}$$

$$\mathcal{P}\quad D \quad \overset{A}{\underset{0,\ \ 0,B}{}}\Big)\Big(= \underset{k}{}\ \frac{1}{\overline{2}\ \ (F_{\mathrm{o}k}^2)}\ \exp\Big)\ \underset{k}{}\ \frac{(F_{\mathrm{o}k}^2\quad F_{\mathrm{c}k}^2)^2}{2\ \ (F_{\mathrm{o}k}^2)^2}\Big(\tag{4.9}$$

Note that restraints are deliberately *not* included in these equations: they are treated as an integral part of their respective models.

The values in (4.9) are taken from the weighting scheme generated by default in the least-squares analysis. As an example, consider the SHELX scheme:[133]

$$\frac{1}{{}^2(F_{\mathrm{o}}^2)} = w = \frac{1}{{}^2(F_{\mathrm{o}}^2) + (aP)^2 + bP} \tag{4.10}$$

where w is the weight used by SHELX; is the equivalent standard deviation, used in the following analysis; is the standard deviation estimated during data collection; a and b are chosen to achieve a flat analysis of variance (*i.e.*, a ^{2} value roughly independent of intensity or resolution); and $P = \frac{1}{3}\max(0, F_{\mathrm{o}}^2) + \frac{2}{3}F_{\mathrm{c}}^2$. The sum over the observations in (4.9) is then related to the reduced goodness-of-fit S reported by SHELX by

$$S = \overline{\quad \frac{1}{n\quad p}\ \underset{k}{\overset{n}{}}\ \frac{(F_{\mathrm{o}k}^2\quad F_{\mathrm{c}k}^2)^2}{2\ \ (F_{\mathrm{o}k}^2)^2}\quad}\ . \tag{4.11}$$

The product in (4.9), on the other hand, refers solely to the observed data, which are common to both models, and which thus cancel out when the probability ratio is taken. Thus

$$\frac{\mathcal{P}(D\ \ A)}{\mathcal{P}(D\ \ \ 0,\ \ 0,B)} = \exp\Big\{\quad \tfrac{1}{2}|\,(n\quad p_A)S_A^2\quad (n\quad p_B)S_B^2 \tag{4.12}$$

where n is the number of observations, p the number of parameters, and S the non-restrained goodness-of-fit at the optimised values of all parameters.

Finally, combining equations 4.1, 4.6, 4.7 and 4.12 gives the result that

$$\begin{aligned}\frac{\mathcal{P}(A\ \ D)}{\mathcal{P}(B\ \ D)} = \exp\Big\{\quad &\tfrac{1}{2}|\,(n\quad p_A)S_A^2\quad (n\quad p_B)S_B^2 \\ &\overset{p_B\quad p_A}{\underset{i}{}}\ \frac{\overset{\text{prior}}{}\ \ {}^{i}}{\overline{2}\ \ (\ \ {}^{i})}\ \frac{\overset{\max}{}}{\underset{0}{}\ \exp\ \frac{(\qquad {}_0)^2}{2\ (\ \ )^2}\ \ \mathrm{d}}\ .\end{aligned} \tag{4.13}$$

It is convenient to work with logarithms rather than directly with the probability ratio. Breaking (4.13) into two parts thus gives

$$F = \quad \tfrac{1}{2} | (n \quad p_A) S_A^2 \quad (n \quad p_B) S_B^2 \tag{4.14a}$$

$$O = \ln \;\; {}^{p_B \quad p_A}_{\quad i} \; \frac{\text{prior} \;\; {}^{i}}{\overline{2} \quad (\;\; {}^{i})} \; \frac{\text{max}}{{}_{0} \;\; \exp \;\; \frac{(\qquad {}_{0})^2}{2 \; (\;\;)^2} \;\; \mathrm{d}} \Bigg) \Bigg(\; . \tag{4.14b}$$

The "fit" term F reflects the relative goodness-of-fit values for the models. The model with more parameters, B, will be favoured by this term since these parameters allow a smaller S value. However, the "Ockham factor" O acts to penalise B for introducing more parameters. Which model is preferable depends on the relative magnitude of these two terms. If the sum of these terms is positive, model A is more probable; if it is negative, then B is more probable.

A quick check of these factors confirms that they behave qualitatively as they should. A low S value for either model favours that model. It appears at first that increasing $n \quad p$ for a particular model will counterintuitively count against that model, but in practice any such change in a good model will be compensated for by a decrease in S: this factor is simply compensating for the "reduction" performed in calculating S in the first place. A large prior range for the parameters in B will count against it: the less one is prepared to say about any parameter, the more it is simply being used as a "fudge factor". On the other hand, a *small* uncertainty in the refined value of any parameter counts against B: if the value of a parameter is not well known, more evidence is required to nail it down to a precise value than to state an approximate figure.

4.3 An example: evidence for MS2

To illustrate this analysis in action, consider two data sets collected from the same crystal of compound **2**. As shown in the previous chapter, this material has a single MS2 geometry at 100 K. As in the previously presented work, the first data set was collected after the crystal had been cooled to 100 K in the dark; the second was collected after irradiation at 100 K with a Xe lamp for

Table 4.1: Comparison of the ground-only (A) and ground-plus-metastable (B) models for a "dark" and "light" data set.

	"Dark" data		"Light" data	
Model	A	B	A	B
n	7499	7499	7488	7488
p	470	498	470	498
S	1.049	1.049	1.056	1.046
$_0$		0.0088		0.0364
$(\ _0)$		0.0044		0.0051
F		15.4		89.1
O		21.9		21.7
Total		6.5		67.4

2 hours. This particular run was chosen since refinement of the "light" data with SHELX indicated the presence of MS2 at a fraction of only $= 3.6(5)\%$. It is therefore important to check whether this is real or an artefact of an overmodelled data set.

In order to evaluate (4.14), a suitable $_{\text{prior}}\ ^i = \ ^i_{\text{max}}\quad ^i_{\text{min}}$ must be determined for each extra parameter ^{i} associated with the metastable-state model. There are 28 such parameters: three for the position and six for the anisotropic displacement parameter of each of the three atoms in the SO_2 unit, plus the excitation fraction . Here let $_{\text{max}} = 0.5$ (otherwise we would be looking for traces of the ground state against a background of the metastable one). Setting to 1 Å for atomic positions and 0.05 Å^2 for displacement parameters reflects the fact that the approximate positions of the metastable-state atoms are well known, but their precise electron distribution less so. In this simple analysis the complication is ignored that multiple possible geometries might need to be taken into account: these could be included by the use of a more sophisticated prior, but will not change the qualitative conclusions of the present analysis.

The results of this analysis are shown in Table 4.1. As expected, in both cases the "fit factor" F favours model B, while the "Ockham factor" O favours model A. Note that, because of the definition of the reduced goodness-of-fit, an equal S value in a model with more parameters indicates a better fit. In the case of the "dark" data, the Ockham factor outweighs the fit factor, indicating that it is roughly 650 times more probable that there is no metastable state present than that a 0.9% excitation has genuinely been achieved. However, in the case of the “light” data, despite the relatively small excitation percentage achieved, this analysis shows that it is vastly (31 orders of magnitude) more probable that the metastable state had indeed been generated than that the crystal remained entirely in the ground state. Moreover, these results are robust to any sensible variation in the priors used: varying these to favour model *A* demonstrates, for instance, that the “light” data do contain enough information to deduce the presence and geometry of the excited state even if this were not previously known.

4.4 An application: evidence for MS1

Having seen that the test confirms crystallographic intuition in a case where it is relatively clear that this is correct, a more complex situation may be considered. In the previous chapter, evidence was presented for high-temperature persistence of MS1 in these compounds. Tables 3.3 and 3.4 present, for compounds **1** and **2** respectively, statistics for refinements of synchrotron data with and without including MS1 in the models.

The same procedure as above was applied to give the data shown in Table 4.2. For compound **1**, 57 new parameters were introduced in model *B*: nine parameters for each of six atoms (*i.e.*, two geometries of MS1) plus three occupancy parameters. The third occupancy, for the ground state, reflects the fact that in SHELX, two parameters can be constrained to sum to unity while three or more parameters must be restrained to a constant sum. The inclusion of this extra restraint, however, ensures that the extraneous parameter does not bias the test in favour of model *A*. For compound **2**, as in the example in the previous section, model *B* required 28 new parameters. The same priors were used for the different types of parameters as in the previous example. The resulting evidence is overwhelmingly in favour of the models including MS1 (as pre-emptively presented in chapter 3).

Table 4.2: Comparison of models without (A) and with MS1 (B), for "light" data collected from compounds **1** and **2**.

Compound	**1**		**2**	
Model	A	B	A	B
n	16762	16762	9304	9304
p	793	850	533	561
S	1.151	1.104	1.248	0.801
$_0$(MS1)		0.040[a]		0.031
($_0$)		0.004		0.004
F		879.0		4025.7
O		95.9		30.3
Total		783.1		3995.4

[a] Two geometries, with populations equal within experimental error.

4.5 Discussion

It is worth noting that evaluating the integral in (4.7) does not make a large difference to the Ockham factor (4.14b), changing it by only 0.02 in the case of the "dark" data, where the refined value is very close to zero, and not at all significantly in the case of any "light" data set. This may indicate that the problems with Hamilton's $\mathcal{R}$ test are in practice not as important to this example as the formal analysis above suggests. Indeed, applying the $\mathcal{R}$ test to the MS2 data produces the same result: there is evidence for the metastable state (at the 5% significance level) in the "light" data but not the "dark". Nonetheless, it is reassuring to be able to place this empirical conclusion on a sturdy theoretical footing.

In these examples, the results of the proposed test accord with crystallographic intuition: when the sample has not been exposed to light, the test shows no evidence of the metastable state; but it concludes that there is good evidence for photoexcitation in the "light" data sets despite the low refined populations. This test may prove most useful in marginal situations where very low populations make it necessary to use very strong restraints to stabilise the refinement. In such situations, more restrictive prior distributions of the parameters may be necessary. For instance, in these examples, little prior information about the expected U values was used. In multiple-temperature experiments, it may be possible to determine U values at low temperatures where the fraction of the metastable state is high, extrapolate to higher temperatures, and use this prediction to detect remnant traces of the metastable state.

It should be noted, however, that the “very strong restraints” referred to above in practice make the refinement much more brutal than is typically considered acceptable. As shown in section 3.6, the background noise in the difference Fourier map makes conventional refinements (with only reasonably soft restraints on ADPs and none on bond lengths or angles) unstable at populations below about 3%. If this method is to be useful in detecting populations below this threshold, it will need to be carefully demonstrated that the restraints involved do not force an unjustified model upon the data.

This in turn will probably require a full Bayesian analysis of the relevant model. The test proposed here is a hybrid between Bayesian and conventional frequentist analysis, in that the likelihood function $\mathcal{P}(D\quad)$ is approximated based on the results of a standard least-squares refinement (4.3). This makes the test very easy to use, as only easy analytical calculations based on the goodness-of-fit S, output by any standard crystallographic software, are required. However, this approach neglects the correlation between parameters in the refinement, which will be significant. This problem could potentially be overcome using a purely Bayesian refinement process, which would yield the full posterior function and hence a better picture of the conclusions that can legitimately be drawn from a given data set. In contrast to the simple calculations presented here, this approach would require a Monte Carlo or similar procedure to evaluate the multidimensional integrals involved. Such calculations, however, are becoming routine in many scientific applications; their application to single-crystal refinements is a promising avenue for further investigation.

CHAPTER 5

STRUCTURAL CALCULATIONS

> The conference proved that hardly a science or branch of technology lacks problems for the computers. Physicists, chemists, aircraft designers had plenty of them to offer. So did psychologists and physiologists. Even sociologists wanted to use the machines, though they did not quite know how to go about it.
>
> – *Time*, Monday, 26 September, 1949

5.1 How can we influence metastable state populations?

If materials that exhibit photoisomerism are to be useful in optical data storage, then controlled, ideally complete, conversion to their photoisomers is important for ease of data reading. However, only two recently reported systems have approached 100% conversion.[90,134] Unlike spin-crossover systems, for instance, there is little evidence of cooperativity between excited centres. Various factors are known to contribute to the low conversion achieved, including limited optical penetration and the confines imposed by a relatively rigid crystal structure on the nuclear motion.[84]

Comparison of gas-phase with solid-state calculations has previously shown that in NO complexes, the crystal surroundings have a small but important influence over the energy landscape of isomerisation. In particular, they affect the barriers associated with rotation about the metal-ligand axis in the side-bound state.[135] By comparison, in triatomic ligands such as SO_2, the additional, free oxygen atom greatly increases the likelihood of steric interactions between the side-bound state and its crystal surroundings. The “reaction cavity” in which the ligand rotates is capable either of increasing or decreasing observed photoexcitation levels, as work on NO_2 complexes has demonstrated.[136,137]

Table 5.1: Summary of photoexcitation experiments on the $[\mathrm{Ru(SO_2)(NH_3)_4}\mathbf{X}]\mathbf{Y}$ family. The Voronoi volume V of the SO_2 group is also indicated.

X	**Y**	Population,	$V(\mathrm{SO_2})$ /Å^3	T /K	Reference
Cl	Cl	0.100(1)	41.52	90(2)	Kovalevsky *et al.*[69]
H_2O	benzenesulfonate$_2$	0.111(1)	38.32	90(2)	Kovalevsky *et al.*[69]
H_2O	tosylate$_2$	0.201(4)	40.32	90(2)	Kovalevsky *et al.*[70]
triflate	triflate	0.373(5)	40.33	90(2)	Kovalevsky *et al.*[70]
isonicotinamide	tosylate$_2$:				
	`Ru01`	0.182(6)	45.80	100(2)	present work (**1**: `Ru01`)
	`Ru51`	0.207(3)	45.07	100(2)	present work (**1**: `Ru51`)
H_2O	( )-camphorsulfonate$_2$	0.098(6)	39.25	100(2)	present work (**2**)

The dynamics of photoexcitation depend on the interplay between the energy costs of distorting the local and long-range structures. It is known that isomerisation can cause sufficient strain on the lattice to crack a crystal.[58] The calculations presented in this chapter were designed to probe the reverse effect: how the lattice in turn can constrain the specific excited-state geometry seen in any particular case. In particular, the effects of the structures of compounds **1** and **2** are compared. Each of these contain elements which might help to prevent steric hindrance around the SO_2 ligand: in compound **1**, the long isonicotinamide *trans* ligand **X** forms rigid hydrogen-bonded pairs, while in compound **2**, the bulky camphorsulfonate counterions **Y** pack relatively poorly.

Although, as for the rest of this thesis, the focus is on ruthenium-sulfur dioxide complexes, some calculations were also performed on the cobalt-nitrogen dioxide complex $[Co^{III}(NO_2)(NH_3)_5]^{2+}$, which was chosen as a well-studied triatomic reference system (*cf.* section 1.3.3). This system is also interesting because, unlike the ruthenium-sulfur dioxide complexes, the transient species observed on photoirradiation in low-temperature IR spectroscopic measurements have never been crystallographically observed.[57]

5.2 Reaction coordinates

Previously, the isomerism of diatomic ligands such as NO has been extensively explored in the gas phase. Explorations of the multidimensional reaction surface have either treated this as a one-dimensional problem, mapping energies as a function of M N O bond angle,[31] or as two-dimensional by also considering variation in M NO distance.[46]

Similarly, the parameters involved in triatomic ligand variation can be projected onto a small-dimensional surface. If the effects of bond length variation are ignored, the rotation of a bent triatomic ligand can be described by three parameters, but these will not contribute equally to the energy. In the results presented here, the primary variable was taken to be the Ru S O (Co N O) angle. For the ruthenium system, the Ru O S O torsion angle would have been equally suitable; for the cobalt system, however, the Co O N O torsion angle would have been less convenient due to the stability of both *endo* and *exo* coordination modes (Section 5.4). The second variable was taken to be rotation about the bond between the metal and the photo; this was not explored uniformly but only at values known to be local minima in energy (Section 5.5).

5.3 Computational details

The work reported here used the CASTEP code, version 5.0, academic release.[138] This is distinguished by its use of the plane-wave-pseudopotential approach and by its use of conjugate-gradient algorithms as an alternative to explicitly diagonalising the Hamiltonian.[139] Ultrasoft pseudopotentials were generated "on-the-fly" based on all-electron calculations at the appropriate level of theory. The exchange-correlation functional was given by the local density approximation, except for the $[Co(NO_2)(NH_3)_5]^{3+}$ ion, where calculations were repeated using the Purdew-Burke-Ernzerhof potential (a GGA potential) for comparison.[140]

Gas-phase geometry optimisations were performed on the $[Ru(SO_2)(NH_3)_4(H_2O)]^{2+}$ and $[Co(NO_2)(NH_3)_5]^{3+}$ ions. In each case the ion was enclosed in a 12 12 12 Å supercell, at which size the energy difference between ground and metastable states had converged to within 4 10 ^{3} eV. The Broyden-Fletcher-Goldfarb-Shanno (BFGS) method was iterated until the forces on free atoms were at most 0.05 eV Å^{-1} and, between subsequent iterations, no atom was displaced by more than 1 10 ^{3} Å and the energy per atom changed by at most 2 10 ^{5} eV. The plane-wave basis set was truncated at an energy of 490 eV. The qualitative results were unchanged if the basis set cutoff was increased, the supercell enlarged, or the *trans* ligand H_2O replaced with isonicotinamide (as in compound **1**).

The optimised geometry and corresponding energy were then recalculated while holding the Ru S O (Co N O) angle fixed. Starting positions were chosen so that this angle ranged from 120 (corresponding to GS) to 0 (corresponding to MS1).

Constrained geometry optimisations were then performed on compound **1** in the solid state. The initial positions and constraints were determined as described in section 5.5. The BFGS method was again used, with the same

	DFT	Literature[58]	% difference	CSDS Co^{III} N
Co NO$_2$	1.8980	1.922(6)	1.2%	1.97(4)
Co NH$_3$ (*cis*)	1.9437	1.974(4)	1.5%	
Co NH$_3$ (*trans*)	1.9933	1.996(5)	0.14%	
N O	1.2367	1.251(5)	1.1%	
O N O	122.4	117(6)	4.6%	
Co N O	118.7	120.0(4)	1.1%	

Table 5.2: Selected bond lengths (Å) and angles ( ) for [Co(NO$_2$)(NH$_3$)$_5$]$^{2+}$, as determined by the gas-phase calculations reported here and from literature crystallographic determinations, with the percentage difference. The final column shows the average Co^{III} N bond length, with standard deviation, from a search of all crystal structures in the Cambridge Structural Database.

convergence parameters described above. The plane-wave basis set was again truncated at an energy of 490 eV, at which value the difference in energy between the ground and metastable states had converged to within 5 10 ^{4} eV. The Brillouin zone was sampled at only; this represents a relatively fine grid because the cell parameters are relatively large (*cf.* Tables 3.3 and 3.4; smallest real lattice spacing: 14.1 Å; largest reciprocal lattice spacing: 0.45 Å^{-1}). Moreover, in an ionic crystal the bands will display little dispersion, so that this sampling is sufficient to model this system reliably. Indeed, sampling the Brillouin zone on a 2 2 2 Monkhorst-Pack grid changed the relative energy of the excited states by less than 1 10 ^{3} eV.

No attempt was made to model fractional occupancy of the excited states; all calculations assumed populations of 100% of the relevant geometries.

5.4 Gas-phase sanity checks

5.4.1 *Bond lengths and angles*

Selected bond lengths and angles from the literature and the presently reported crystallographic experiments and gas-phase calculations are compared in Tables 5.2 and 5.3. Agreement is reasonable despite the comparison of gas-phase calculation with solid-state experiment.

	Crystallography	DFT	Literature	% difference	CSDS Ru^{II} S
Ru SO$_2$	2.0868(9)	2.0696	2.0892(5)	0.94%	2.33(5)
Ru NH$_3$	2.124(4)	2.1016	2.1171(16)	0.73%	
Ru OH$_2$	2.119(2)	2.1295	2.1283(14)	0.06%	
S O	1.445(3)	1.4329	1.4368(16)	0.27%	
O S O	115.29(12)	119.6	116.06(9)	3.1%	
Ru S O	122.35(13)	120.4	121.80(9)	1.1%	

Table 5.3: Selected bond lengths (Å) and angles ( ) for $[RuSO_2(NH_3)_4H_2O]^{2+}$, as determined by the gas-phase calculations and synchrotron crystallography (on compound **2**) reported here, and from literature crystallographic determinations, with the percentage difference between the DFT and literature experimental values. The final column shows the average Ru^{II} S bond length, with standard deviation, from a search of all crystal structures in the Cambridge Structural Database.

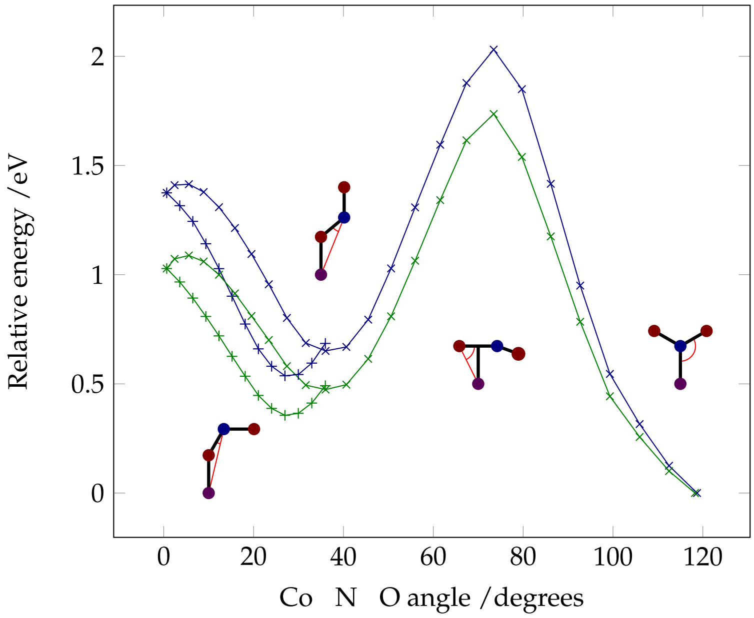

Figure 5.1: Energies of geometry-optimised configurations of the $[Co(NH_3)_5NO_2]^{2+}$ ion as a function of constrained Co N O angle, for the *exo* ( ) and *endo* (+) geometries. The exchange-correlation potentials used are the LDA (blue) and the PBE (green).

5.4.2 *Rotation in the NO_2 plane*

In the Co NO_2 system (Fig. 5.1) the ^{2} geometry corresponds to an energy *maximum*, and the two excited-state minima shown here correspond to *exo* and *endo* MS1 linkages. Moreover, the *endo* geometry was found to have a slightly lower energy than the *exo*, despite the fact that the *endo* is the form obtained by direct synthesis of the *O*-bound isomer and observed in previous photocrystallographic experiment.[58] However, the energy difference is sufficiently small that considerably more work is needed before it can be claimed to be significant. It may be noted in passing that the *exo* geometry is stabilised by hydrogen bonding between the NH_3 ligands and NO_2 N atom, which is not possible for the softer S atom.

The peak around 70 indicates strongly that the species observed in the low-temperature photoexcited IR spectrum was not, as assumed, an ^{2}-linked state. To determine its true identity, further exploration of the gas-phase reaction surface would be helpful. Figure 5.1 could be extended to a second dimension by considering the Co O N O torsion angle as a second variable, which would make the search for local minima more thorough. It may, however, be that this intermediate owes its stability to interactions within the solid state and is therefore not visible in gas-phase calculations, or even that its original observation was in error.

The Co NO_2 system was also used for a comparison between the LDA and PBE exchange-correlation functionals, represented in Fig. 5.1 by the blue and green curves respectively. As can be seen, the PBE gives a slightly higher barrier to excitation from the ground state, but the two functionals are otherwise highly consistent in their representation of the energy landscape: certainly, the difference between the two methods is comparable to the error introduced by performing a gas-phase rather than a solid-state calculation. The use of the LDA in the remainder of these calculations is thereby justified.

5.4.3 *Rotation in the SO_2 plane*

In the Ru SO_2 system, by contrast, minima corresponding to the known ground and two excited states are clearly visible (Fig. 5.2, red curve). The relative energies of the three minima are consistent with the temperatures at

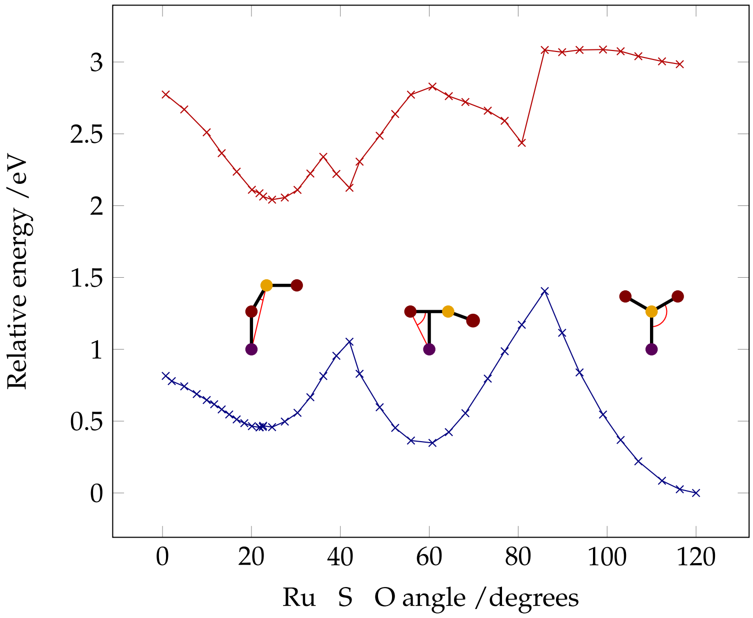

Figure 5.2: Energies of geometry-optimised configurations of the $[Ru(SO_2)(NH_3)_4(H_2O)]^{2+}$ ion as a function of constrained Ru S O angle, for the first singlet (blue) and triplet (red) states.

which these structures are crystallographically observed, in that the minimum of highest energy (and lowest energy barrier to decay) is observed at the lowest temperature. The activation energy for decay from the *O*-bound state to the ^{2} state is 0.596 eV. This is equal to $277kT$ at 25 K, where this structure is known to be stable, and $58kT$ at 120 K, where it decays within hours (Section 3.6), suggesting that this value is slightly overestimated.

The activation energy for decay from the ^{2} state to the ground state is 1.060 eV ($= 137kT$ at 90 K), which is again overestimated in comparison with a value of 651 meV observed from time-resolved crystallographic studies at varying temperatures.[70] This discrepancy is likely a result of the simple exchange-correlation potential used.

For this system the optimised geometries from this first step were used for a new single-point calculation in which the total spin was forced to 1; in other words, the energy of the first triplet state was calculated, as a first approximation to the photoexcited state which leads to the isomerisation reaction (green curve). Although this is clearly a somewhat naïve model for photoexcitation on this material, it encouragingly captures the important point that GS in this state can relax to MS2 and MS1, exactly as observed experimentally.

5.4.4 Rotation about the Ru SO$_2$ bond

In ruthenium-sulfur dioxide systems the barrier to rotation about the Ru (SO) bond (that is, to change of the N Ru S O torsion angle) is known to be low, so that crystal packing effects are important in determining the preferred orientation of the bound S O linkage in the ^{2} excited state.[70,135] As a result, one would expect to find two local energy minima, 180 apart, for the bound S and O atoms. Associated with each of these are a further two minima for the free O atom, as expected by the pseudo-symmetry of the geometry. This gives a total of four local minima for the free O atom, related approximately by reflection in the Ru S O plane and 180 rotation about the Ru (SO) bond. Referring back to the crystallographic results, it can be seen that in compound **1** at `Ru01` three of these possible positions are visible (Figure 3.8(a)), while only one is visible at the `Ru51` site (Figure 3.8)(c)) and in compound **2** (Figure 3.9(a)).

This analysis was confirmed by DFT calculation. Starting from the optimised excited-state configuration of the $[Ru(SO_2)(NH_3)_4(H_2O)]^{2+}$ ion (as in **2**), gas-phase geometry optimisations were performed with the Ru O S O torsion angle (*i.e.*, the position of the free oxygen atom) fixed at evenly spread values over the range of physically accessible positions. The Ru O S angle was held constant throughout to ensure that the SO$_2$ ligand remained in its ^{2} configuration. The results confirmed that, for a given orientation of the bound O and S atoms, in the absence of crystal packing effects there are two local minima with essentially equal energies at around 99 . (Figure 5.3).

It is interesting to note that if these calculations are performed without fixing the Ru O S angle, at several torsion angles the system becomes unstable with respect to the MS1, the highest-energy metastable geometry. This suggests that suitable physical restraints on the attainable values of the torsion angle – arising, for instance, from steric repulsion – may encourage or inhibit formation of this isomer in different crystal structures.

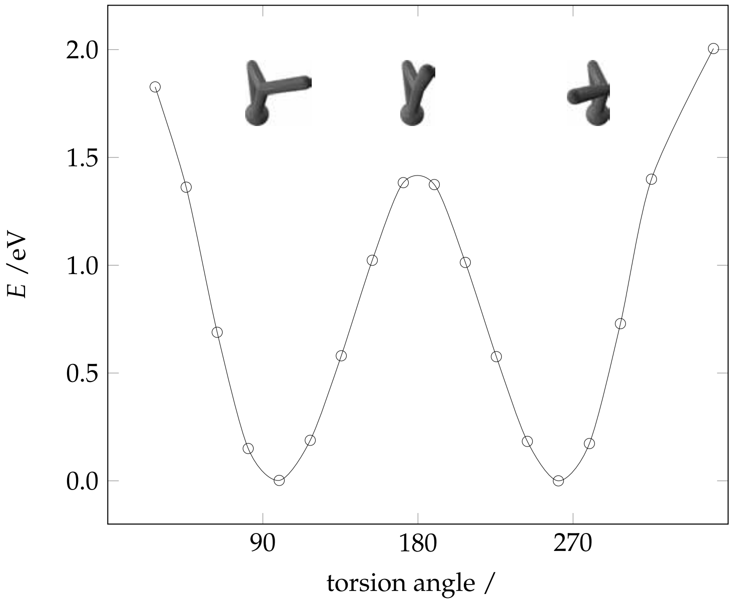

Figure 5.3: Relative energies of geometry-optimised configurations of the $[Ru(SO_2)(NH_3)_4(H_2O)]^{2+}$ ion as a function of constrained Ru O S O torsion angle. Torsion angles around zero are not physically sensible since they force the free O atom too close to the ammine ligands.

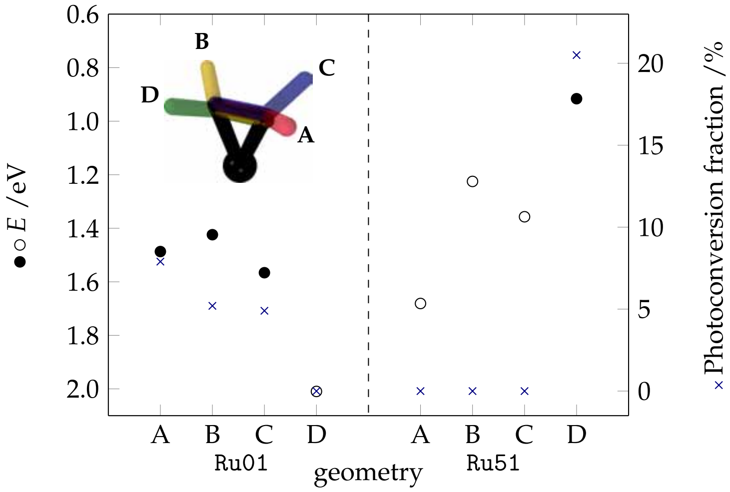

Figure 5.4: DFT energies E relative to the ground state (filled circles if geometries are experimentally observed, open circles if not) and experimental photoexcitation efficiencies (crosses) for the four possible excited-state geometries at each of the two Ru sites in compound **1**. Note that the energy scale increases downwards, so that on both vertical scales points closer to the top of the figure represent more favourable geometries.

5.5 Solid-state calculations

Subsequent DFT calculations were performed in the solid state in order to elucidate the reasons for the particular orientations of MS2 observed. This comparison relies upon the two independent Ru sites in compound **1**: since they are exposed to almost identical irradiation conditions, the substantial difference in photoexcitation observed can be attributed to the difference in local crystal packing. The slight difference in irradiation conditions between the sites arises from the fact that, as for NO complexes, the photoexcited state population will depend on anisotropy introduced during the irradiation process, such as the polarisation and orientation of the light.[90,112] However, this effect is unlikely to be significant in this experiment, due to the use of an unpolarised source and rotation about the diffractometer axis during irradiation, and because the two Ru SO_2 moeities are almost exactly antiparallel to one another (Ru S vectors 175.01(2) apart, $RuSO_2$ planes 13.53(13) apart).

The unit cell parameters and positions of most non-hydrogen atoms were held constant at their crystallographically determined values (from the "light" data), while the positions of the SO_2 ligands and the hydrogen atoms were optimised from the ideal gas-phase geometry. This gives an idealised model which assumes 100% excitation in a single geometry at the relevant site, with zero excitation at the other.

The results show good agreement with experiment at 100 K (Figure 5.4): in general, the geometries with the greatest observed occupation percentage are those where the position of the free oxygen atom comes at the lowest energy cost. Furthermore, the new geometry seen at `Ru51` at 175 K from the decay of MS1 (Section 3.6) is **B**, the most stable of the geometries at that site not observed at 100 K.

These results suggest that the timescale of excitation is long enough that the SO_2 ligand can equilibrate to the lowest energy geometry available to it. Indeed, given the broadband irradiation, the metastable state will certainly have been itself excited, and in some fraction photochemically returned to the ground state, during the course of irradation.

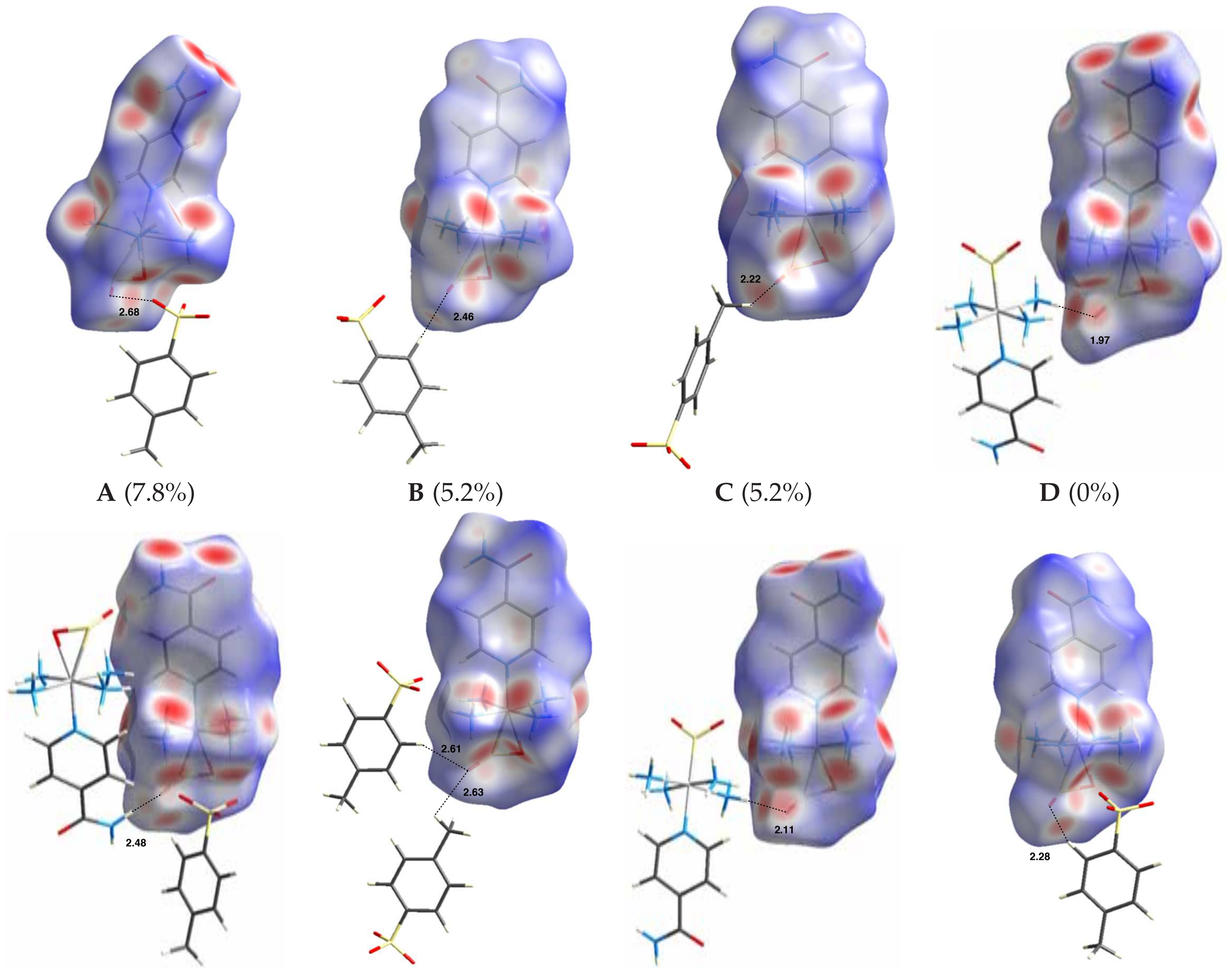

A (7.8%) **B** (5.2%) **C** (5.2%) **D** (0%)

A (0%) **B** (0%) **C** (0%) **D** (20.7%)

Figure 5.5: Hirshfeld surfaces for the $[Ru(SO_2)(NH_3)_4(isonicotinamide)]^{2+}$ ion in each of the four metastable geometries possible at `Ru01` (above) and `Ru51` (below) in compound **1**, as determined by DFT calculation. Blue regions correspond to positive values of d_{norm} (see equation 5.1 in text), white to zero, and red to negative values. The nearest molecules to the SO_2 group are also shown, and the closest distance between them and the free O atom indicated. The excitation percentages achieved experimentally are given for ease of comparison.

5.6 Geometric calculations

5.6.1 *Hirshfeld partitioning*

The steric interactions which give rise to the calculated energetic differences can be visualised using the Hirshfeld surfaces of the possible excited-state geometries (Figure 5.5). These isosurfaces are defined as enclosing the region where the contribution due to the complex ion dominates (*i.e.*, is at least half of) the total crystalline electron density.[141] The program CRYSTALEXPLORER 2.1 was used to plot the normalised contact distances d_{norm} on these surfaces, where

$$d_{\mathrm{norm}} = \frac{d_{\mathrm{i}} \quad r_{\mathrm{i}}^{\mathrm{vdW}}}{r_{\mathrm{i}}^{\mathrm{vdW}}} + \frac{d_{\mathrm{e}} \quad r_{\mathrm{e}}^{\mathrm{vdW}}}{r_{\mathrm{e}}^{\mathrm{vdW}}} \,. \tag{5.1}$$

Here d_{i} is the distance to the nearest nucleus *inside* the surface and $r_{\mathrm{i}}^{\mathrm{vdW}}$ the van der Waals radius of that atom. Similarly, d_{e} and $r_{\mathrm{e}}^{\mathrm{vdW}}$ refer to the nearest *external* nucleus. Thus regions where $d_{\mathrm{norm}} < 0$, shown in red in Figure 5.5, indicate abnormally close contact.[142,143]

At `Ru01` (Figure 5.5, top row), in the three observed geometries **A–C** the closest approach to the free O atom is from a hydrocarbon group, with contact distance only slightly less than the sum of the van der Waals radii. (Closest approach: geometry **C**; $d = 2.22$ Å; *cf.* van der Waals radii[144] H = 1.20 Å, O = 1.52 Å.) In the geometry **D** which is not observed, however, the closest approach to the free O atom is an $\mathrm{NH_3}$ group, with normalised contact distance similar to that in the hydrogen bonding between pairs of isonicotinamide ligands, visible at the top of the same diagram. ($d_{\mathrm{O\quad H}} =$ 1.97 Å; $d_{\mathrm{O(\quad H\quad)N}} = 2.72$ Å. Amide hydrogen-bonded pair: $d_{\mathrm{O\quad H}} = 1.82$ Å; $d_{\mathrm{O(\quad H\quad)N}} = 2.87$ Å.) It thus appears that hydrogen bonding with the adjacent nitrogen atom distorts this geometry sufficiently to render it energetically less stable than the remaining three (Figure 5.4).

At `Ru51`, the situation is slightly less obvious. Again, the closest contact for the observed geometry **D** is with a CH group ($d = 2.28$ Å); and again, for two of the non-observed geometries **A** and **C**, the closest contact to the free O atom is with a NH group so that hydrogen bonding can influence the geometry. (**A**: $d_{\mathrm{O\quad H}} = 2.48$ Å; $d_{\mathrm{O(\quad H\quad)N}} = 3.13$ Å; **C**: $d_{\mathrm{O\quad H}} = 2.11$ Å; $d_{\mathrm{O(\quad H\quad)N}} = 2.82$ Å.) However, the reason why geometry **B** is higher in energy is not clear. Indeed, of the three geometries *not* observed at 100 K at this site, it is the lowest in energy, and as previously noted, it is populated at 175 K from the decay of MS1.

Nonetheless, comparison of Figure 5.5 with the DFT results in Figure 5.4 show that the energy differences obtained can indeed largely be attributed to the interactions of the free O atom in the metastable state with its crystal surroundings.

5.6.2 Voronoi-Dirichlet partitioning

In addition to specific steric effects, the metastable state occupancy may conceivably depend on the total volume of the reaction cavity – the space available for the SO_2 ligand to rotate in. Accordingly, the program TOPOS 4.0 was used to partition space into Voronoi-Dirichlet polyhedra, so that each point is assigned to the atom closest to it.[145,146] This gives a volume for the SO_2 group of 39.25 $Å^3$ in compound **2**, which is very similar to that in previously described members of this family (Table 5.1). Compound **1**, on the other hand, has a significantly increased volume (*ca.* 45 $Å^3$) at both of its SO_2 sites. Examination of the crystal structure shows that this appears to be due to the rigid rod-like structural elements formed when hydrogen bonds between pairs of amide groups join two ruthenium complexes.

It is notoriously difficult to predict the effects of changes in a molecule's structure on its crystal packing; but it is nonetheless interesting to note that in this example, rigid elements (as in compound **1**) were more effective at creating space within the crystal structure than poorly packing ones (as in compound **2**). This increased volume, however, does not lead necessarily to a greater excitation fraction; as shown in the previous section, specific intermolecular interactions are more important than net volume in influencing the excitation.

CHAPTER 6

X-RAY ABSORPTION SPECTROSCOPY

> Plaything of the General Electric staff is their monstrous x-ray farm on the laboratory roof. C. P. Haskins exposed grapefruit, orange, aster and cotton seeds to x-rays from two to 16 minutes. The grapefruit blossomed five weeks after planting. In nature first blossoming requires five years' growth. On the contrary, sweet orange seed grew into a twisted, two-leaf plant. As grotesque was a sour orange plant with no green chlorophyll in its stem or leaves. The aster and cotton plants were gnarled dwarfs.
>
> – *Time*, Monday, 27 June, 1932

6.1 Background

This chapter describes X-ray absorption near-edge spectroscopy (XANES) experiments performed with two principal aims. First, the changes upon exposure to light in the XANES spectra of complexes known to exhibit photoisomerism were investigated, with a particular view towards understanding the partial oxidation state change expected as a result of the photoisomerisation. Second, this technique made it possible to investigate the behaviour of complexes of which single crystals are not available. As an exemplar, the complex with **X** = pyridine was chosen; this is readily synthesised but has not yielded suitable crystals with any counterion **Y**.

The Ru $L_{2,3}$ edges were selected for two reasons: first, the K edge requires harder X-rays than were available on the beamline used for the experiment. Second, the short core-hole lifetime of K edges notoriously results in increased uncertainty in energy and hence a broadened, lower-resolution spectrum.[147]

Table 6.1: Samples whose XANES and EXAFS spectra were measured. The number of repeated spectra (with identical acquisition parameters) averaged to give the data presented here, and the source of the compounds, are also indicated.

	Compound		Repetitions	Source
References	$[Ru^{III}(acac)_3]^a$		1	Aldrich
	$[Ru^{II}(bipy)_2(bipydc)](PF_6)_2{}^b$		1	Solaronix
	$[Ru^{II}(NH_3)_4(HSO_3)_2]$		1	synthesised[c]
Samples	Ru$[(SO_2)(NH_3)_4$**X**]**Y**			synthesised[c]
1	**X** = isonicotinamide	**Y** = tosylate$_2$	3	
2	**X** = H_2O	**Y** = ( )-camphorsulfonate$_2$	1	
3	**X** = pyridine	**Y** = $(CF_3SO_3)_2{}^{d,e}$	3	
4	**X** = H_2O	**Y** = tosylate$_2$	3	

[a] acac = $(CH_3CO)_2CH^-$ [b] bipy = 2,2 -bipyridine; bipydc = 2,2 -bipyridine-4,4 -dicarboxylic acid
[c] See Appendix A. [d] Not available as single crystals. [e] Contains substantial contamination from chloride ions; see discussion in text.

6.2 Experimental

6.2.1 *Procedure*

The experiment was performed at beamline B18 at Diamond Light Source, UK. The ring energy was 3.0 GeV and the ring current 200 mA. Spectra were taken in total electron yield mode, using a Si(111) monochromator with an estimated resolution of $E/E = 1.4 \quad 10^{4}$. I_0 values were obtained by measuring the drain current from an aluminised mylar foil placed in the beam immediately upstream of the sample. The beam was collimated and focused with Cr-coated Si mirrors at an incidence angle of 2.3 mrad. High-energy harmonics were rejected using two Ni-coated Si mirrors at 10 mrad incidence angle.

The energy scale was calibrated the day before the experiment using Ti foil; the position of the first maximum in the derivative of the K-edge spectrum was set to 4966 eV. The accuracy of measurements at the much lower energies used in these experiments was estimated to be *ca.* 1 eV.

Both XANES and EXAFS spectra were measured at the Ru L_2 and L_3 edges: a total energy range from 2780 eV to 3215 eV was covered, with approximate step sizes 1 eV in the pre-edge regions and 0.25 eV thereafter.

The samples were ground to powder and held in place with conducting (graphite) tape such that the radiation was incident at an angle of *ca.* 45 . The sample chamber was pumped to vacuum and cooled to the base temperature of the cryostat, 91(5) K. Data collection for each compound then proceeded as follows: a "dark" spectrum was first collected, then the sample was irradiated *in situ* with the tungsten lamp for 2 hours. The lamp was then extinguished and a "light" spectrum collected. Reference spectra for Ru(II) and Ru(III) were collected in the dark as summarised in Table 6.1.

Where repeated runs were made of the same spectrum, these were averaged. Linear backgrounds were then fitted to the pre- and post-edge regions of each spectrum using SIXPACK.[148] These were used to normalise the spectra in the standard way, to achieve a mean of zero in the pre-edge region and unity in the post-edge region.

The experimental apparatus and samples are shown in Figure 6.1.

6.2.2 *Overlapping spectra*

The Cl K edge at 2822 eV lies almost directly underneath the Ru L_3 edge at 2838 eV, so that any Cl present in samples will interfere with the Ru spectra examined here. Unfortunately, the standard synthesis of members of the target family is from the compound **X** = **Y** = Cl^- (Appendix A). The Cl^- ligand is easily replaced by N- or O-donor ligands to yield a variety of compounds with **X** = neutral donor, **Y** = $(Cl^-)_2$.[149,150] In the case of compounds which can be crystallised, the Cl^- counterion **Y** may also be replaced by adding a suitable counterion (*e.g.*, tosylate or camphorsulfonate), leaving crystals to form, and draining off the chloride ions with the mother liquor. However, compounds which do not crystallise – such as compound **3** in the present work – are typically precipitated by the addition of a large volume of acetone, which is filtered off once the solid has formed. In this case there is no opportunity to remove the chloride ions.

In an attempt to circumvent this problem for compound **3**, solid $AgCF_3SO_3$ was added to a water solution of the pyridine complex in an attempt to precipitate out the chloride counterions as AgCl (Appendix A). $AgCF_3SO_3$ was chosen for its solubility in acetone, so that the complex could be precipitated as normal by the method described above, without fear of contamination from the remaining silver compound. This attempt, however, was at best partially successful; the presence of Cl in the sample of compound **3** was obvious

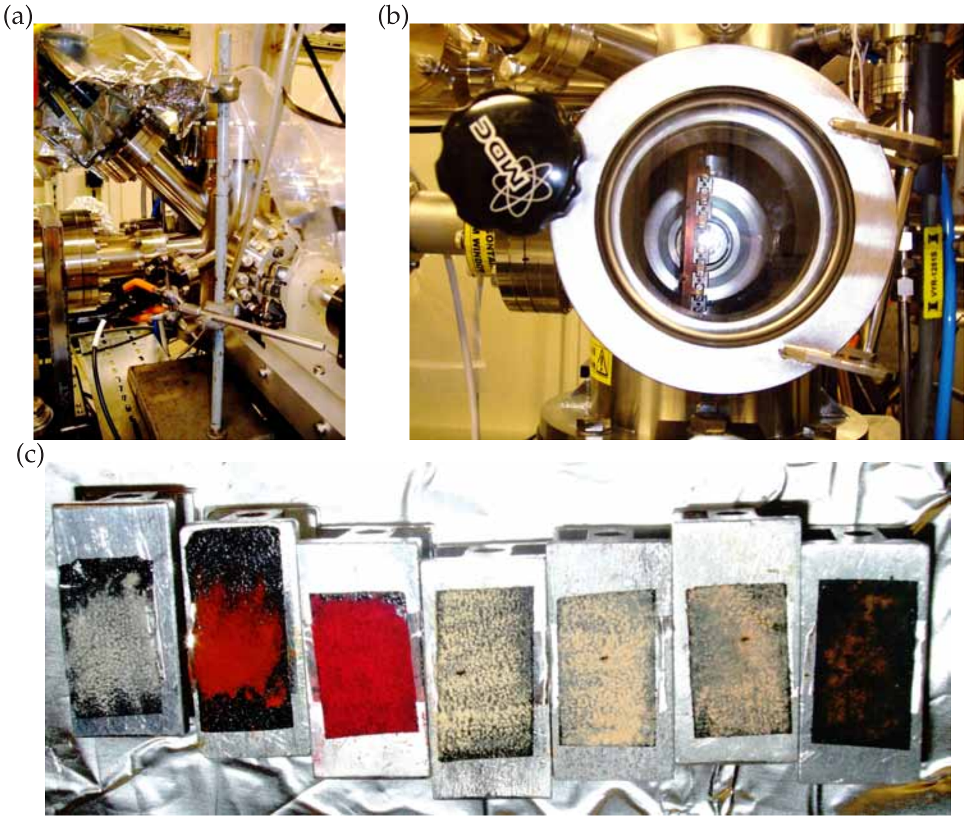

Figure 6.1: Experimental setup: (a) the exterior of the vacuum chamber, showing the lens to focus optical light on the samples; (b) the interior of the chamber, showing mounted samples; the vertical position was adjusted to move different samples into the beam. (c) The samples after irradiation, from left: [Ru(acac)$_3$], [Ru^{II}(bipy)$_2$(bipydc)](PF$_6$)$_2$, [Ru^{II}(NH$_3$)$_4$(HSO$_3$)$_2$], and compounds **4**, **1**, **2**, and **3**. (For key to ligand abbreviations, see Table 6.1.) Some irradiation damage is visible on samples **1**, **2** and **4**.

in its L_3 spectrum. As discussed below, this could be accounted for in the subsequent analysis; however, this is not ideal, and alternative methods for removing Cl$^-$ counterions should be explored in future work.

6.3 XANES vs EXAFS

It was found that the differences between the light and dark spectra of the same compound were only visible in the XANES region of the spectrum, with very little difference above *ca.* 30 eV above the white-line peak (Figure 6.2; *e.g.*, root-mean-square deviation above 2870 eV for compound **4**: $= 4.5 \quad 10^{4}$, which is negligible in comparison with the expected error in each point in the normalised spectra). Moreover, it was very difficult to fit a background to the spectra in the EXAFS region that resulted in a reasonable Fourier transform. Finally, due to the high degree of crystallinity of the samples, the EXAFS oscillations decayed rapidly ($k \quad 8\,\text{Å}^{-1}$) after even the L_2 edge (the L_3 spectrum, of course, is cut short by the L_2 edge). For these reasons we decided to focus on the XANES region in the following analysis.

6.4 Reference materials

The XANES spectra of the reference materials are shown in Figure 6.3. Some features appear to be associated with different oxidation states, such as the pre-edge peak centred at 2839 eV in the $\mathrm{Ru}^{\mathrm{III}}$ complex and the peak centred at 2851 eV in the $\mathrm{Ru}^{\mathrm{II}}$ complexes. There is no clear trend in the white line intensity, although a systematic difference here would be easily masked by imperfect background subtraction.

Comparing the "dark" and "light" spectra of the samples reveals changes in the features identified in the references. The "light" and "dark" spectra of all four samples are presented in Figure 6.2. In general, the feature at 2851 eV diminishes on exposure to light, and a pre-edge shoulder at 2839 eV forms. This is consistent with the partial oxidation expected as the Ru moves from binding through the softer Lewis base S to the harder Lewis base O.

6.5 Principal component analysis

6.5.1 Rationale

In the absence of either an experimental or a theoretical reference matching the data closely, it was decided to subject the data to *principal component analysis*, which does not depend upon such a reference. Rather, it determines the minimum number of independent components needed to account for variation within a series of data sets – in this case, spectra. It is sometimes possible to extend this analysis to determine physically meaningful components, such as the spectra of individual compounds in a mixture. However, determining the number of components is often a scientifically relevant result in its own right.

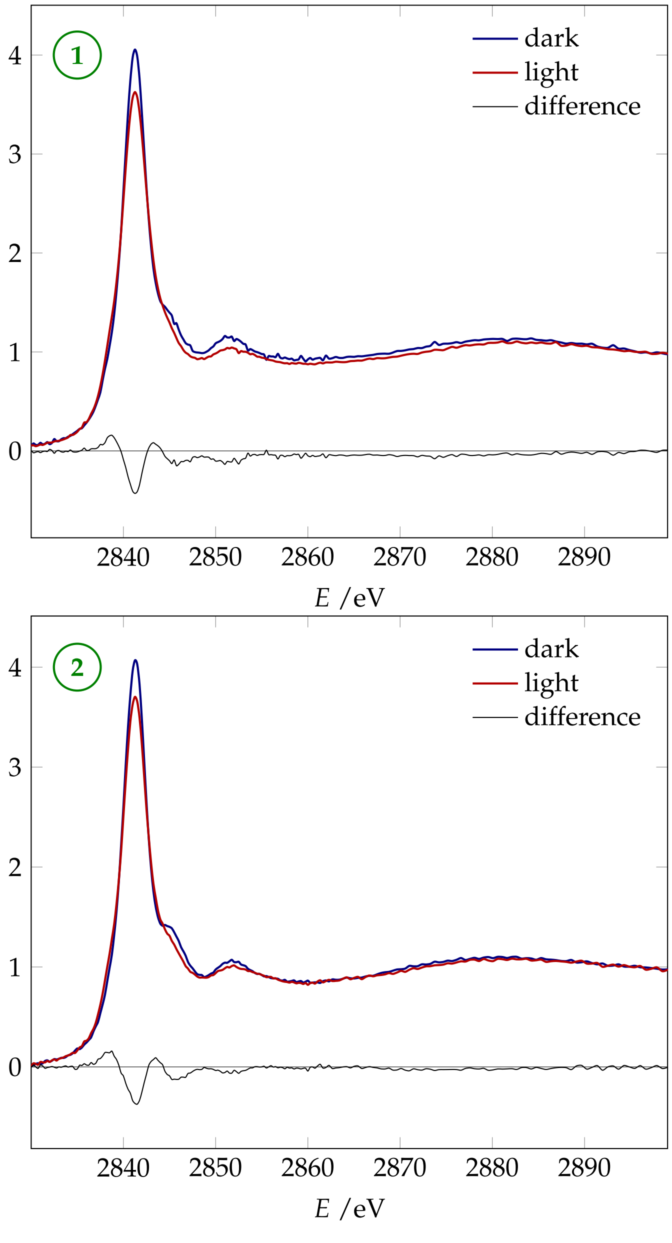

Figure 6.2: Comparison of the light and dark spectra of compounds **1** to **4** (indicated in top left corner of each graph).

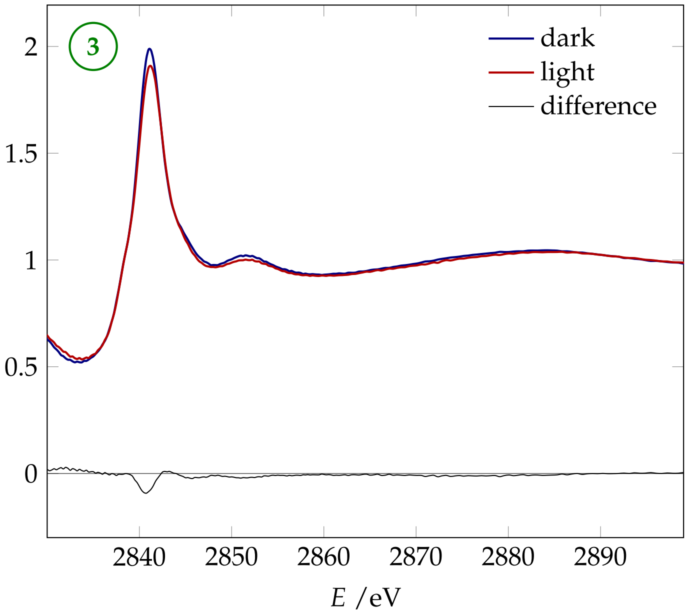
③
dark
light
difference
2
1.5
1
0.5
0
2840
2850
2860
2870
2880
2890
E /eV

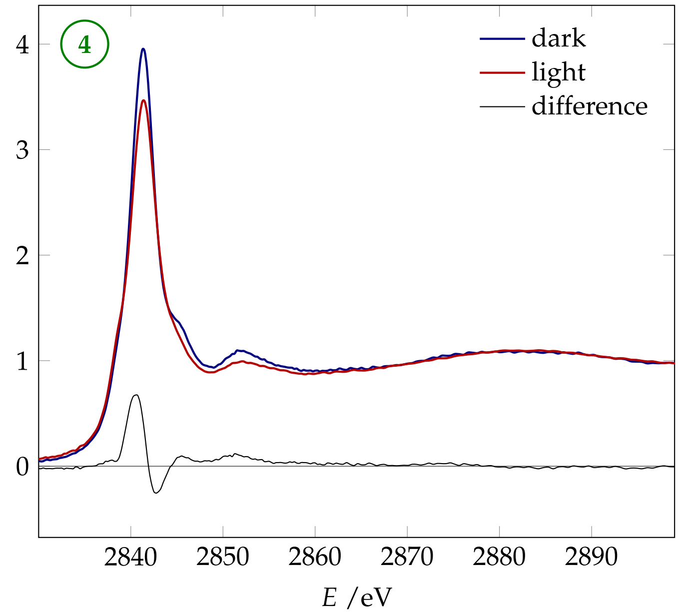
④
dark
light
difference
4
3
2
1
0
2840
2850
2860
2870
2880
2890
E /eV

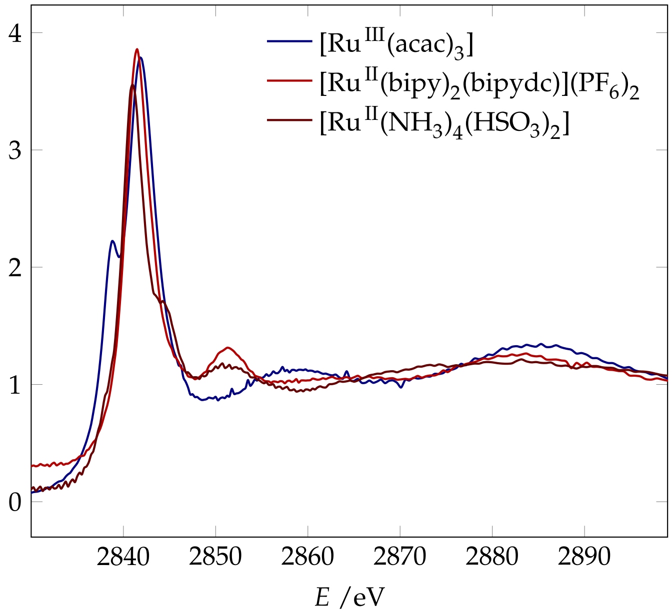

Figure 6.3: Spectra of the reference compounds.

Principal component analysis was first used with XANES data to identify the number of distinct Mo surface environments in a Mo/TiO$_2$ catalyst.[151] It has since become increasingly popular. Over the past decade, it has often been used to analyse time-resolved data collected during chemical reactions: a data set with only two large principal components indicates evidence for only the reactant and product, while a third large principal component reveals the presence of an intermediate.[152] Recent advances in theoretical modelling have made it possible to extract quantitative information about the structure of such intermediates.[153,154]

The virtue of this technique for analysing this experiment is that, rather than relying on experimental or theoretical references, this technique effectively draws the reference from the samples themselves. Moreover, it does not require an experimental spectrum representing 100% photoexcitation to be effective – which is helpful since such a spectrum is not available.

6.5.2 *Mathematical background*

Principal component analysis is based upon the mathematical procedure of *singular value decomposition* of a matrix.[155] Suppose we have an r c matrix $\mathbf{A}$

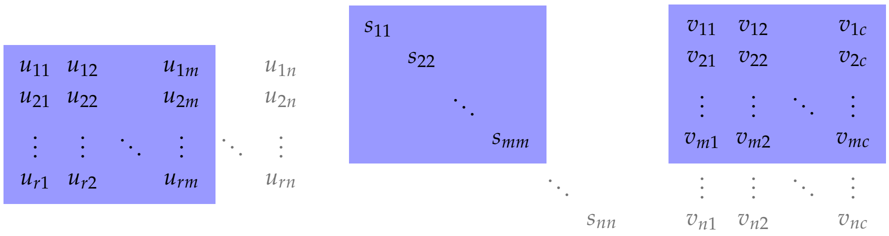

Figure 6.4: Schematic diagram of the matrix multiplications in equations 6.1 and 6.2. If the singular values s_{ii} 0 for $m < i \approx n$, then truncating the matrices to the portions highlighted in blue will still give an accurate reconstruction of the original data. For clarity, zero entries in the diagonal matrices **S** and **S** (centre) are not explicitly shown.

consisting of row vectors spanning an n-dimensional space (so that clearly $n \approx r$). We can then write

$$\underset{r\ \ c}{\mathbf{A}} = \underset{r\ \ n}{\mathbf{U}}\ \underset{n\ \ n}{\mathbf{S}}\ \underset{n\ \ c}{\mathbf{V}^{\dagger}} \tag{6.1}$$

where **U** and **V** are unitary and **S** is an $n \quad n$ diagonal matrix whose entries are known as the *singular values* of **A**. It is common to arrange these values in descending order; if this is specified then **S** is unique (although **U** and **V** are not).

Consider the experimental data as such an $r \quad c$ matrix **D**, where the r rows each represent a particular experiment and the c columns the (normalised) absorbance at a particular energy. In the following discussion it will be assumed that $r < c$, which will be true except in the unlikely case that many spectra are collected over a small energy range (or at poor resolution); the argument may be easily modified to fit this case. Under this assumption, due to the presence of experimental error, in general $n = r$. However, if, in the absence of error, the data span an m-dimensional space, $m < n$, then the lowest $n \quad m$ singular values will be very small, and truncating the decomposition to

$$\underset{r\ \ c}{\mathbf{D}} \quad \underset{r\ \ c}{\mathbf{D}} = \underset{r\ \ m}{\mathbf{U}}\ \underset{m\ \ m}{\mathbf{S}}\ \underset{m\ \ c}{\mathbf{V}^{\dagger}} \tag{6.2}$$

will give a good approximation to the measured data (Figure 6.4). Indeed, since this truncation removes random variation, the resulting matrix may be a better approximation to the true values under consideration than the original measurements!

The relevance of this method to the present analysis is that the logic above may be applied in reverse: if the data are well represented by m principal components but no fewer, this is good evidence that they span an m-dimensional space. In particular, if the data represent a mixture of compounds (in a system where contributions combine linearly), this is evidence for the presence of m chemical components in the mixture. Depending on the purpose of the analysis, this result alone may be sufficient, or further techniques may be used to identify these components.

The question naturally arises of how to determine when a singular value can be considered “very small”. A number of statistical techniques are available; in the present analysis, however, the qualitative approach is taken of including successive components until the reconstructed spectra visually match the originals. When this occurs there is a clear sudden drop in the root-mean-square residual, which typically falls from around $2.4 \quad 10^{\ 3}$ to less than $1 \quad 10^{\ 3}$ (Figure 6.5).

6.6 Results

Principal component analysis was initially performed on the dark and light spectra of the three compounds (**1**, **2**, and **4**) for which single-crystal data is available. For this analysis, as expected, $m = 2$ principal components sufficed to model all six spectra well. This is demonstrated by the good fit of reconstructions from two components (Figure 6.5(a)).

The same analysis was then performed on the same six spectra with the addition of the dark spectrum of compound **3** (Figure 6.5(b)). For a visibly adequate reconstruction of the original spectra, three components are now necessary. The third component mainly acts to adjust the white line peak shape. The need for this component may reasonably be attributed to interference from the Cl K-edge absorbance; despite truncating the energy as close as possible to the Ru L_3 white line, it appears that the Cl K-edge still influences the spectrum.

Finally, to these seven spectra was added the light spectrum of compound **3**, and principal component analysis performed once again (Figure 6.5(c)). Again, a three-component analysis suffices to reconstruct the original spectra. In

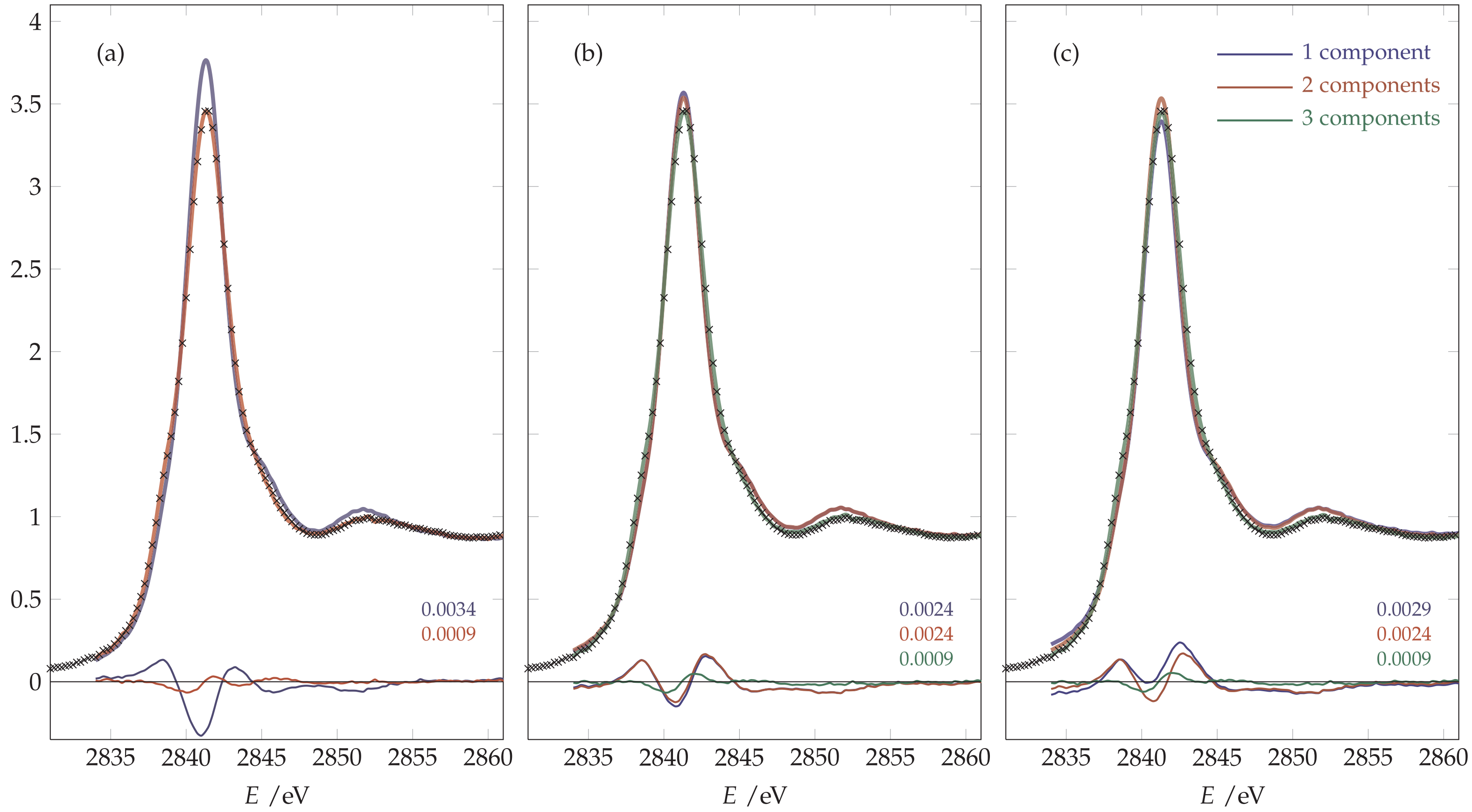

Figure 6.5: (a) Reconstruction of the light data for compound **4** from principal component analysis (PCA) of the light and dark data for compounds **1**, **2** and **4** (six spectra total). A single-component reconstruction (blue) visibly deviates from the experimental data (black crosses) whereas one using two components (red) fits these data well. The differences between the observed and reconstructed spectra are also shown, with the root-mean-square deviation displayed. (b) Reconstruction of the same data from PCA now including, in addition, the dark spectrum of compound **3**. A three-component reconstruction (green) is now required for a visibly accurate fit. (c) Reconstruction of the same data from PCA now including, in addition, both the dark and light spectra of compound **3**. A three-component reconstruction still yields a visibly accurate fit with rms deviation $< 1 \quad 10^{3}$.

other words, the shape of the light spectrum for compound **3** is fully explained by the dark spectra for the other compounds, the (crystallographically known) effects of photoexcitation on these compounds, and the distortion due to the Cl present in the sample. We can conclude that the photoexcitation behaviour in compound **3** is identical to that crystallographically observed in the other compounds.

6.7 Prospects

The data presented here show in principle that XANES is a viable technique for studying photoisomerism; indicate directly that there is a partial oxidation state increase upon isomerisation in this family of compounds; and demonstrate that the same changes occur in compound **3** as in those compounds which have been crystallographically studied as single crystals. There are at least two potential avenues for future work on these systems. First, collection of *K*-edge spectra may complement the work presented here, enabling more quantitative EXAFS data to be collected and changes in coordination geometry may be quantitatively investigated, although care will be needed to avoid problems due to core-hole lifetime broadening. Second, in future work on compounds which are not readily crystallised, alternative methods should be used to remove the Cl counterions. For instance, ion chromatography may prove more successful than the precipitation method attempted here. On the basis of the above analysis, it can be predicted that a similar principal component analysis using spectra without contamination from the Cl *K* edge should yield just two principal components, rather than the three needed here.

CHAPTER 7

CONCLUSIONS AND FURTHER WORK

> There is enough work in sight to absorb the energies of many experimenters, and there is sure to be far more than we can see.
>
> – W. H. Bragg
> discourse delivered at the Royal Institution
> 5 June, 1914

7.1 Conclusions

The work presented here has focused on the structural changes which take place when members of the $[Ru(SO_2)(NH_3)_4\mathbf{X}]\mathbf{Y}$ family are irradiated with light. Two of the members of this family, compounds **1** and **2**, have both ground and metastable-state structures reported here for the first time. Two features of their metastable-state structures are particularly interesting: first, MS1, the *O*-bound state, is found to persist on crystallographic timescales at temperatures up to 120 K, although it has previously only been observed at 13 K. Second, in compound **1**, the crystallographically independent Ru sites display differing excitation properties which vary with the the local crystal packing arrangement. These results concord well with the *ab initio* energies of optimised potential metastable state geometries.

On a technical level, these results demonstrate that good photocrystallographic data can be obtained even for structures which are in some way suboptimal due to low symmetry (compound **1**) or disorder (compound **2**), and from laboratory as well as synchrotron sources. The evidence for the presence of disordered components with low fractional occupancy has been investigated using a novel test based on Bayesian analysis, which provides an unprecedented means of assessment of the validity of very low populations in crystallographic refinement. This test confirms the statistical significance of the metastable states observed.

Finally, compound **3** has been shown by XANES to exhibit the same photolinkage isomerism behaviour as the other members of the family, although only a powder sample was available. This further demonstrates that XANES is a viable and valuable technique for detecting photoinduced linkage isomerism – and in particular the partial oxidation state changes associated with isomerism –in these systems.

7.2 Further work

Of course, these results raise at least as many questions as they answer. For clarity, these are divided into three general categories: those pertaining to potential applications of these materials, those relating to fundamental computational work on them, and those concerning experimental exploration of their properties.

7.2.1 Relevance to applications

The extent to which these photoinduced changes are cooperative remains an open question. No crystallographic evidence was observed for correlation between excitation at neighbouring sites in these materials, in contrast to the very striking cooperative effects such as macroscopic crystal deformation observed in certain other photoactive systems. A theoretical investigation into the differences between the internal stresses in these systems may therefore yield interesting results. It should be noted that such a calculation would require an accurate treatment of the comparatively weak intermolecular interactions, probably *via* the inclusion of semi-empirical dispersion forces (such as, for example, the DFT+D method). The importance of cooperativity goes beyond academic interest: making excitation cooperative would likely increase the fraction of the metastable state generated and hence make the resulting material more attractive for technological applications. The demonstrated influence of the reaction cavity on excitation suggests that it may be possible to "crystal engineer" materials in which there is very little steric hindrance to excitation, which may also result in increased metastable state populations.

Another device-relevant feature of the materials presented here is the fact that they are not active at room temperature. Further work aimed at increasing the stability of the metastable state with temperature is therefore desirable. It is not immediately clear, however, how this can be achieved within this family of materials, and it may be best simply to continue to explore related photolinkage isomerism systems (*i.e.*, different **X** and **Y** moieties).

The structural results presented here will be of most value when they are correlated with optical properties. It would thus be useful to attempt to write gratings into thin films impregnated with these compounds, and to measure their holographic properties. These experiments, like those reported in this thesis, will need to be undertaken at low temperatures.

7.2.2 *Computation and data analysis methods*

The DFT results presented here projected the reaction surface on which the SO_2 ligand moves onto a single dimension. Retaining several dimensions would give a fuller picture of its energetic environment than either of the approaches used here: the previously mentioned curve and point measurements at theoretical geometries. In particular, three dimensions suffice to fully describe the rotation of this ligand, considered as a rigid body. A three-dimensional surface, however, would be both difficult to display and very time-consuming to calculate. As suggested earlier, a judicious choice of two dimensions, such as the Ru S O angle and Ru O S O torsion angle, might prove an effective compromise.

The reliability of complex crystallographic refinements is obviously central to this field, and there is considerable further work to be done on the interpretation of marginal data. In particular, calculating multidimensional posterior likelihoods for the parameters would reveal the true extent to which correlation between them increases their uncertainty. A full Bayesian analysis appears particularly promising in this regard, as it would allow assumptions regarding reasonable values for refined parameters to be explicitly taken into account.

7.2.3 *Development of experimental techniques*

The work presented here focused for simplicity on broadband, unpolarised irradiation delivered in as isotropic a manner as possible (*e.g.*, by rotating the sample during irradiation); however, investigation of the excitation achieved as a function of the wavelength, polarisation and orientation of the incident light has the potential to lead to substantially greater understanding of the mechanisms for photoexcitation.

In theory, EXAFS should enable the local coordination geometry and in particular the bond lengths around the Ru atom to be monitored. It would be worthwhile to persevere with this technique, perhaps considering the Ru or S *K* edges. These would have the added advantage that there would be no need to attempt to remove Cl counterions. Similarly, preliminary measurements in thin films using UV/visible spectroscopy and transmission electron microscopy gave encouraging results, suggesting that further work on these techniques would be useful.

The high-temperature persistence of the *O*-bound state MS1 merits further investigation. In particular, kinetic studies, perhaps using IR spectroscopy, would help to clarify at which temperatures it can be expected. It would also be possible to perform similar calculations on this state to the ones presented here on MS2, which would be expected to reveal a similar influence from the local crystal surroundings on the excitation achieved.

Finally, photocrystallography is now being used over increasingly faster timescales using choppers timed to the intrinsic time structure available at synchrotrons. From the point of view of technique development, the $[Ru(SO_2)(NH_3)_4\mathbf{X}]\mathbf{Y}$ family of materials would provide excellent test samples for these experiments, since the metastable state structure is well known and its lifetime can be tuned by adjusting the temperature. Such experiments would also be of fundamental interest: evaluating the kinetics of de-excitation over a wide temperature range would act as a probe of the energy surface discussed above, shedding new light upon the versatile and unexpected behaviour of these remarkable materials.

APPENDIX A

SYNTHESES

A.1 $[Ru(SO_2)(NH_3)_4(NC_5H_4CONH_2)](C_7H_7SO_3)_2$ (compound 1)

Tetraammineisonicotinamide(sulfur dioxide)ruthenium(II) tosylate was synthesised by a modification of the literature synthesis of the triflate.[156] Isonicotinamide (125 mg) was dissolved in 3.5 ml water, and $[Ru(NH_3)_4(SO_2)Cl]Cl$ (50 mg), prepared as above, was then added to form a bright red solution. A solution of *para*-toluenesulfonic acid (200 mg in 0.5 ml to 1 ml water) was added dropwise, causing small yellow crystals of $[Ru(SO_2)(NH_3)_4(NC_5H_4CONH_2)]$-$(CH_3C_6H_4SO_3)_2$ to precipitate out within a day. No attempt to quantify the yield was made.

A.2 $[Ru(SO_2)(NH_3)_4(H_2O)]((\ \ )\text{-}C_{10}H_{15}SO_4)_2$ (compound 2)

Tetraammineaqua(sulfur dioxide)ruthenium(II) ( )-camphorsulfonate was synthesised by a slight modification of literature syntheses of the tosylate.[70,157] $[Ru(NH_3)_5Cl]Cl_2$ (1.0 g) was dissolved in 40 ml water at 75 C with stirring. In this solution was dissolved $NaHSO_4$ (1.5 g). Sulfur dioxide gas was then slowly bubbled through, with the solution maintained at 75 C for about 30 minutes, and then removed from the heat and left for about 1 hour to cool to room temperature. $[Ru(NH_3)_4(HSO_3)_2]$ (0.7 g) was isolated as a mass of small, pale yellow crystals. These were dissolved in 80 ml 1:1 HCl by heating to boiling. The solution was filtered hot and left to cool overnight, yielding dark red needles of $[Ru(NH_3)_4(SO_2)Cl]Cl$ (0.3 g). Finally, ( )-camphorsulfonic acid (0.26 g) was dissolved in water (5 ml) at 90 C, to which $[Ru(NH_3)_4(SO_2)Cl]Cl$ (50 mg) was added and stirred to dissolve. The yellow solution was allowed to cool to room temperature to produce small yellow-orange plates of $[Ru(SO_2)(NH_3)_4(H_2O)](C_{10}H_{15}SO_4)_2$ suitable for X-ray diffraction experiments. Again, no attempt was made to quantify the yield.

A.3 $[Ru(SO_2)(NH_3)_4(C_5H_5N)]Cl_2$ (compound 3)

Tetraamminepyridine(sulfur dioxide)ruthenium(II) chloride was synthesised by published methods.[150] A slight modification was attempted whereby excess $AgCF_3SO_3$ was added, and the resulting AgCl precipitate filtered off, before precipitating out the complex by the addition of acetone. However, the XANES spectrum of the resulting precipitate clearly revealed the persistence of chloride ions. No further characterisation was undertaken.

APPENDIX B

CRYSTALLOGRAPHIC DATA

Full details of the photocrystallographic experiments referred to in the thesis text, including tables of observed intensities, are provided on the attached CD: "dark" structure determinations for compounds **1** and **2**, all "light" structure determinations reported in Table 3.7, and the structure of the non-photoactive compound [Ru$(HSO_3)_2$(CO)(terpy)] reported in Appendix C.

APPENDIX C

[Ru(HSO_3)$_2$(CO)(terpyridine)]

The published synthesis of [Ru(terpy)(SO_2)(CO)Cl]Cl 2 H_2O (terpy = terpyridine) was followed and the solution kept refrigerated for several weeks.[158] Orange crystals suitable for X-ray diffraction formed but appeared from diffraction studies in fact to be [Ru(HSO_3)$_2$(CO)(terpy)]. No further characterisation, however, was undertaken.

$RuC_{16}H_{13}O_7N_3S_2$, 522.49 g mol^{-1}, triclinic, $P\bar{1}$, $Z = 2$. $a = 9.520(3)$ Å, $b = 10.407(3)$ Å, $c = 10.526(3)$ Å, $= 67.65(3)$, $= 67.92(3)$, $= 71.13(3)$. $V = 873.7(5)$ Å^3. 7457 reflections measured of which 2276 unique, $R_{\text{int}} =$ 0.0348. 262 parameters refined with no restraints. $R(F) = 0.0602$ $(I > 2\ \ )$, 0.0632 (all). $wR2(F^2) = 0.1783$ $(I > 2\ \ )$, 0.1827 (all). Highest peak (deepest hole) 1.276 (0.560) e Å^{-3}.

BIBLIOGRAPHY

> Wanted, a careful steady Man to act in the capacity of Captain's Steward and Gentleman's Servant.—Application to be made to the Printer.—*Note.* None but those of unquestionable character, with respectable references, need apply.
>
> – Advertisement, *The Sydney Gazette and New South Wales Advertiser*, Sunday, 8 March 1807

1. Röntgen, W. C. *Nature* **1896**, *53*, 274–276.
2. Sommerfeld, A. J. W. *Ann. Phys.* **1912**, *343*, 473–506.
3. Friedrich, W.; Knipping, P.; von Laue, M. *K. Bayer. Akad. der Wiss.* **1912**, 303–322.
4. Bragg, W. H. *Nature* **1914**, *93*, 494.
5. Dunitz, J. D.; Schomaker, V.; Trueblood, K. N. *J. Phys. Chem.* **1988**, *92*, 856–867.
6. Maverick, E.; Mirsky, K.; Knobler, C. B.; Trueblood, K. N.; Barclay, L. R. C. *Acta Cryst. B* **1991**, *47*, 272–280.
7. Phillips, A. E.; Halder, G. J.; Chapman, K. W.; Goodwin, A. L.; Kepert, C. J. *J. Am. Chem. Soc.* **2010**, *132*, 10–11.
8. Hemley, R. J.; Mao, H.-k.; Struzhkin, V. V. *J. Synchrotron Rad.* **2005**, *12*, 135–154.
9. Katrusiak, A. *Acta Cryst. A* **2008**, *64*, 135–148.
10. Halder, G. J.; Kepert, C. J. *Aust. J. Chem.* **2006**, *59*, 597–604.
11. Suh, M. P.; Cheon, Y. E. *Aust. J. Chem.* **2006**, *59*, 605–612.

12. Phillips, A. E.; Goodwin, A. L.; Halder, G. J.; Southon, P. D.; Kepert, C. J. *Angew. Chem. Int. Ed.* **2008**, *47*, 1396–1399.

13. Cohen, M. D.; Schmidt, G. M. J. *J. Chem. Soc.* **1964**, 1996–2000.

14. Irie, M. *Chem. Rev.* **2000**, *100*, 1685–1716.

15. Kumar, G. S.; Neckers, D. C. *Chem. Rev.* **1989**, *89*, 1915–1925.

16. Gütlich, P.; Garcia, Y.; Woike, T. *Coord. Chem. Rev.* **2001**, *219–221*, 839–879.

17. Irie, M. *Bull. Chem. Soc. Japan* **2008**, *81*, 917 – 926.

18. Balahura, R. J.; Lewis, N. A. *Coord. Chem. Rev.* **1976**, *20*, 109–153.

19. Burmeister, J. L. *Coord. Chem. Rev.* **1990**, *105*, 77–133.

20. Coppens, P.; Novozhilova, I.; Kovalevsky, A. *Chem. Rev.* **2002**, *102*, 861–883.

21. Coppens, P.; Zheng, S.-L.; Gembicky, M. *Z. Krist.* **2008**, *223*, 265–271.

22. Rack, J. J.; Winkler, J. R.; Gray, H. B. *J. Am. Chem. Soc.* **2001**, *123*, 2432–2433.

23. Schuy, A.; Woike, T.; Schaniel, D. *J. Sol-Gel Sci. Tech.* **2009**, *50*, 403–408.

24. Fomitchev, D. V.; Bagley, K. A.; Coppens, P. *J. Am. Chem. Soc.* **2000**, *122*, 532–533.

25. Fomitchev, D. V.; Novozhilova, I.; Coppens, P. *Tetrahedron* **2000**, *56*, 6813–6820.

26. Wei, H.-H.; Ho, L.-Z. *Inorg. Chem.* **1984**, *23*, 624–627.

27. Rachford, A. A.; Petersen, J. L.; Rack, J. J. *Inorg. Chem.* **2005**, *44*, 8065–8075.

28. Mockus, N. V.; Marquard, S.; Rack, J. J. *J. Photochem. Photobiol. A* **2008**, *200*, 39–43.

29. Mockus, N. V.; Rabinovich, D.; Petersen, J. L.; Rack, J. J. *Angew. Chem. Int. Ed.* **2008**, *47*, 1458–1461.

30. McClure, B. A.; Abrams, E. R.; Rack, J. J. *J. Am. Chem. Soc.* **2010**, *132*, 5428–5436.

31. Buchs, M.; Daul, C. A.; Manoharan, P. T.; Schläpfer, C. W. *Int. J. Quantum Chem.* **2003**, *91*, 418–431.

32. Prisant, L. M.; Carr, A. A.; Hawkins, D. W. *Postgrad. Med.* **1993**, *93*, 92.

33. Schaniel, D.; Woike, T.; Schefer, J.; Petříček, V. *Phys. Rev. B* **2005**, *71*, 174112.

34. Schaniel, D.; Woike, T.; Schefer, J.; Petříček, V.; Krämer, K. W.; Güdel, H. U. *Phys. Rev. B* **2006**, *73*, 174108.

35. Schefer, J.; Schaniel, D.; Petříček, V.; Woike, T. *Z. Krist.* **2008**, *223*, 259–264.

36. Carducci, M. D.; Pressprich, M. R.; Coppens, P. *J. Am. Chem. Soc.* **1997**, *119*, 2669–2678.

37. Coppens, P.; Fomitchev, D. V.; Carducci, M. D.; Culp, K. *J. Chem. Soc., Dalton Trans.* **1998**, 865–872.

38. Kovalevsky, A. Y.; King, G.; Bagley, K. A.; Coppens, P. *Chem. Eur. J.* **2005**, *11*, 7254–7264.

39. Schaniel, D.; Cormary, B.; Malfant, I.; Valade, L.; Woike, T.; Delley, B.; Krämer, K. W.; Güdel, H.-U. *Phys. Chem. Chem. Phys.* **2007**, *9*, 3717–3724.

40. Schaniel, D.; Woike, T.; Delley, B.; Biner, D.; Krämer, K. W.; Güdel, H.-U. *Phys. Chem. Chem. Phys.* **2007**, *9*, 5149–5157.

41. Bitterwolf, T. E. *Coord. Chem. Rev.* **2006**, *250*, 1196–1207.

42. Schaniel, D.; Woike, T. *Phys. Chem. Chem. Phys.* **2009**, *11*, 4391–4395.

43. Delley, B.; Schefer, J.; Woike, T. *J. Chem. Phys.* **1997**, *107*, 10067–10074.

44. Ishikawa, T.; Tanaka, K. *J. Chem. Phys.* **2005**, *122*, 74314.

45. Ishikawa, T.; Tanaka, K. *Chem. Phys. Lett.* **2005**, *412*, 164–170.

46. Ishikawa, T.; Tanaka, K. *Z. Krist.* **2008**, *223*, 334–342.

47. Sizova, O. V.; Lubimova, O. O.; Sizov, V. V.; Ivanova, N. V. *Z. Kristallogr.* **2008**, *223*, 343–355.

48. Hitchman, M. A.; Rowbottom, G. L. *Coord. Chem. Rev.* **1982**, *42*, 55–132.

49. Murmann, R. K.; Taube, H. *J. Am. Chem. Soc.* **1956**, *78*, 4886–4890.

50. Balzani, V.; Ballardini, R.; Sabbatini, N.; Moggi, L. *Inorg. Chem.* **1968**, *7*, 1398–1404.

51. Jackson, W. G.; Lawrence, G. A.; Lay, P. A.; Sargeson, A. M. *Inorg. Chem.* **1980**, *19*, 904–910.

52. Jackson, W. G.; Lawrence, G. A.; Lay, P. A.; Sargeson, A. M. *J. Chem. Soc., Chem. Commun.* **1982**, 70–72.

53. Jackson, W. G. *Inorg. Chem.* **1987**, *26*, 3857–3859.

54. Scandola, F.; Bartocci, C.; Scandola, M. A. *J. Phys. Chem.* **1974**, *78*, 572–575.

55. Eslami, A. *Thermochimica Acta* **2004**, *409*, 189–193.

56. Grenthe, I.; Nordin, E. *Inorg. Chem.* **1979**, *18*, 1869–1874.

57. Johnson, D. A.; Pashman, K. A. *Inorg. Nucl. Chem. Lett.* **1975**, *11*, 23–28.

58. Kubota, M.; Ohba, S. *Acta Cryst. B* **1992**, *48*, 627–632.

59. Boldyreva, E. V. *Mol. Cryst. Liq. Cryst.* **1994**, *242*, 17–52.

60. Virovets, A. V.; Podberezskaya, N. V.; Boldyreva, E. V.; Burleva, L. P.; Gromilov, S. A. *J. Struct. Chem.* **1992**, *33*, 890–898.

61. Boldyreva, E. V.; Virovets, A. V.; Burleva, L. P.; Dulepov, V. E.; Podberezskaya, N. V. *J. Struct. Chem.* **1993**, *34*, 602–614.

62. Virovets, A. V.; Boldyreva, E. V.; Burleva, L. P.; Dulepov, V. E.; Podberezskaya, N. V. *J. Struct. Chem.* **1994**, *35*, 236–241.

63. Dulepov, V. E.; Boldyreva, E. V. *React. Kinet. Catal. Lett.* **1994**, *53*, 289–296.

64. Boldyreva, E.; Kivikoski, J.; Howard, J. A. K. *Acta Cryst. B* **1997**, *53*, 394–404.

65. Boldyreva, E.; Kivikoski, J.; Howard, J. A. K. *Acta Cryst. B* **1997**, *53*, 405–414.

66. Schenk, W. A. *Angew. Chem. Int. Ed.* **1987**, *26*, 98–109.

67. Kubas, G. J. *Acc. Chem. Res.* **1994**, *27*, 183–190.

68. Johnson, D. A.; Dew, V. C. *Inorg. Chem.* **1979**, *18*, 3273–3274.

69. Kovalevsky, A. Y.; Bagley, K. A.; Coppens, P. *J. Am. Chem. Soc.* **2002**, *124*, 9241–9248.

70. Kovalevsky, A. Y.; Bagley, K. A.; Cole, J. M.; Coppens, P. *Inorg. Chem.* **2003**, *42*, 140–147.

71. Bowes, K. F.; Cole, J. M.; Husheer, S. L. G.; Raithby, P. R.; Savarese, T. L.; Sparkes, H. A.; Teat, S. J.; Warren, J. E. *Chem. Comm.* **2006**, 2448–2450.

72. van de Nes, A. S.; Braat, J. J. M.; Pereira, S. *Rep. Prog. Phys.* **2006**, *69*, 2323–2363.

73. Woike, T.; Kirchner, W.; Schetter, G.; Barthel, T.; Hyung-sang, K.; Haussühl, S. *Optics Commun.* **1994**, *106*, 6–10.

74. Cole, J. M. *Z. Kristallogr.* **2008**, *223*, 363–369.

75. Haussühl, S.; Schetter, G.; Woike, T. *Optics Commun.* **1995**, *114*, 219–222.

76. Hall, T. J.; Jaura, R.; Connors, L. M.; Foote, P. D. *Progr. Quant. Electr.* **1985**, *10*, 77–146.

77. Fally, M.; Imlau, M.; Rupp, R. A.; Ellabban, M. A.; Woike, T. *Phys. Rev. Lett.* **2004**, *93*, 243903–(1–4).

78. Imlau, M.; Haussühl, S.; Woike, T.; Schieder, R.; Angelov, V.; Rupp, R. A.; Schwarz, K. *Appl. Phys. B* **1999**, *68*, 877–885.

79. Goulkov, M.; Schaniel, D.; Woike, T. *J. Opt. Soc. Am. B* **2010**, *27*, 927–932.

80. Ostroverkhova, O.; Moerner, W. E. *Chem. Rev.* **2004**, *104*, 3267–3314.

81. Kuroki, L.; Takami, S.; Yoza, K.; Morimoto, M.; Irie, M. *Photochem. Photobiol. Sci.* **2010**, *9*, 221–225.

82. Nakanishi, H.; Jones, W.; Thomas, J. M.; Hursthouse, M. B.; Motevalli, M. *J. Chem. Soc., Chem. Comm.* **1980**, 611–612.

83. Cole, J. M. *Acta Cryst. A* **2008**, *64*, 259–271.

84. Cole, J. M. *Chem. Soc. Rev.* **2004**, *33*, 501–513.

85. Collet, E.; Lemée-Cailleau, M.-H.; Buron-Le Cointe, M.; Cailleau, H.; Wulff, M.; Luty, T.; Koshihara, S.-Y.; Meyer, M.; Toupet, L.; Rabiller, P.; Techert, S. *Science* **2003**, *300*, 612–615.

86. von Korff Schmising, C.; Bargheer, M.; Woerner, M.; Elsaesser, T. *Z. Kristallogr.* **2008**, *223*, 283–291.

87. Ohashi, Y. Structural determination of unstable species. In *Models, mysteries and magic of molecules*; Boeyens, J. C. A., Ogilvie, J. F., Eds.; Springer: Dordrecht, 2008; pp 109–135.

88. Adachi, S.; Inoue, K.; Oka, T.; Yagi, N.; Tanaka, Y.; Ishikawa, T.; Shiro, Y. Subnanosecond-resolved X-ray diffraction at the SPring-8 high flux beamline BL40XU. *Eighth International Conference on Synchrotron Radiation Instrumentation (SRI 2003)*, 2004; pp 1383–1386.

89. Wulff, M.; Kong, Q.; Cammarata, M.; Lo Russo, M.; Anfinrud, P.; Schotte, F.; Lorenc, M.; Ihee, H.; Kim, T. K.; Plech, A. Picosecond diffraction at the ESRF: How far have we come and where are we going? *Ninth International Conference on Synchrotron Radiation Instrumentation (SRI 2006)*, 2007; pp 1187–1194.

90. Cormary, B.; Malfant, I.; Valade, L.; Buron-Le Cointe, M.; Toupet, L.; Todorova, T.; Delley, B.; Schaniel, D.; Mockus, N.; Woike, T.; Fejfarová, K.; Petříček, V.; Dušek, M. *Acta Cryst. B* **2009**, *65*, 612–623.

91. Techert, S.; Zachariasse, K. A. *J. Am. Chem. Soc.* **2004**, *126*, 5593–5600.

92. Yeung, Y. M. C.; Pace, G.; Cole, J. M.; Phillips, A. E.; Friend, R. H. In preparation for *J. Chem. Phys.*

93. Gembicky, M.; Coppens, P. *J. Synch. Rad.* **2007**, *14*, 133–137.

94. Husheer, S. L. G.; Cole, J. M.; d'Almeida, T.; Teat, S. J. *Rev. Sci. Inst.* **2010**, *81*, 043905.

95. Ihee, H.; Wulff, M.; Kim, J.; Adachi, S.-i. *Int. Rev. Phys. Chem.* **2010**, *29*, 453–520.

96. Fomitchev, D. V.; Furlani, T. R.; Coppens, P. *Inorg. Chem.* **1998**, *37*, 1519–1526.

97. Legrand, V.; Pillet, S.; Weber, H.-P.; Souhassou, M.; Létard, J.-F.; Guionneau, P.; Lecomte, C. *J. Appl. Cryst.* **2007**, *40*, 1076–1088.

98. Vorontsov, I. I.; Coppens, P. *J. Synchrotron Rad.* **2005**, *12*, 488–493.

99. Hohenberg, P.; Kohn, W. *Phys. Rev.* **1964**, *136*, B864–B871.

100. Kohn, W.; Sham, L. J. *Phys. Rev.* **1965**, *140*, A1133–A1138.

101. Jones, R. O.; Gunnarsson, O. *Rev. Mod. Phys.* **1989**, *61*, 689–746.

102. Martin, R. M. *Electronic structure: basic theory and practical methods*; Cambridge University Press: Cambridge, 2004.

103. Ref. 102, p. 88.

104. Hamann, D. R.; Schlüter, M.; Chiang, C. *Phys. Rev. Lett.* **1979**, *43*, 1494–1497.

105. Vanderbilt, D. *Phys. Rev. B* **1990**, *41*, 7892–7895.

106. Segall, M. D.; Lindan, P. J. D.; Probert, M. J.; Pickard, C. J.; Hasnip, P. J.; Clark, S. J.; Payne, M. C. *J. Phys.: Condens. Matter* **2002**, *14*, 2717–2744.

107. Ref. 102, p. 43.

108. Cartier dit Moulin, C.; Villain, F.; Bleuzen, A.; Arrio, M.-A.; Sainctavit, P.; Lomenech, C.; Escax, V.; Baudelet, F.; Dartyge, E.; Gallet, J.-J.; Verdaguer, M. *J. Am. Chem. Soc.* **2000**, *122*, 6653–6658.

109. Yokoyama, T.; Takahashi, K.; Sato, O. *Phys. Rev. B* **2003**, *67*, 172104.

110. Chen, L. X.; Jäger, W. J. H.; Jennings, G.; Gosztola, D. J.; Munkholm, A.; Hessler, J. P. *Science* **2001**, *292*, 262–264.

111. Bressler, C.; Abela, R.; Chergui, M. *Z. Kristallogr.* **2008**, *223*, 307–321.

112. Schaniel, D.; Schefer, J.; Delley, B.; Imlau, M.; Woike, T. *Phys. Rev. B* **2002**, *66*, 085103.

113. Jeschke, G.; Matysik, J. *Chem. Phys.* **2003**, *294*, 239–255.

114. Rigaku Corporation, *CrystalClear: An Integrated Program for the Collection and Processing of Area Detector Data*, 2002.

115. BrukerAXS, *XPREP: data reduction software*, v. 5060, 2002.

116. Altomare, A.; Burla, M. C.; Camalli, G.; Cascarano, G.; Giacovazzo, C.; Gualiardi, A.; Polidori, G. *J. Appl. Cryst.* **1994**, *27*, 435.

117. Sheldrick, G. M. *SHELX97. Programs for crystal structure analysis*, University of Gttingen, Germany, 1997.

118. Farrugia, L. J. *J. Appl. Cryst.* **1999**, *32*, 837–838.

119. Cole, J. M. X-ray diffraction of photolytically induced molecular species in single crystals. In *Models, mysteries and magic of molecules*; Boeyens, J. C. A., Ogilvie, J. F., Eds.; Springer: Dordrecht, 2008; pp 29–61.

120. Moore, J. W.; Baird, H. W.; Miller, H. B. *J. Am. Chem. Soc.* **1968**, *90*, 1358–1359.

121. Gott, G. A.; Fawcett, J.; McAuliffe, C. A.; Russell, D. R. *J. Chem. Soc., Chem. Commun.* **1984**, 1283–1284.

122. Kubas, G. J.; Ryan, R. R.; McCarty, V. *Inorg. Chem.* **1980**, *19*, 3007–3010.

123. Brayshaw, S. K.; Knight, J. W.; Raithby, P. R.; Savarese, T. L.; Schiffers, S.; Teat, S. J.; Warren, J. E.; Warren, M. R. *J. Appl. Cryst.* **2010**, *43*, 337–340.

124. Hamilton, W. C. *Acta Cryst.* **1965**, *18*, 502–510.

125. Protassov, R.; van Dyk, D. A.; Connors, A.; Kashyap, V. L.; Siemiginowska, A. *Astrophys. J.* **2002**, *571*, 545.

126. *International Tables for Crystallography Volume C*, First online ed.; Prince, E., Ed.; International Union of Crystallography, 2006.

127. Ref. 126, Chapter 8.4.

128. Gilmore, C. J. *Acta Cryst. A* **1996**, *52*, 561–589.

129. Trotta, R. *Contemp. Phys.* **2008**, *49*, 71–104.

130. Gull, S. Bayesian inference and maximum entropy. In *Maximum-entropy and Bayesian methods in science and engineering*; Erickson, G. J., Smith, C. R., Eds.; Kluwer Academic Publishers: Dordrecht, 1988; Vol. 1, pp 53–74.

131. Sivia, D. S. *Data analysis: a Bayesian tutorial*, 2nd ed.; Oxford University Press: New York, 2006.

132. Ref. 131, 78.

133. Sheldrick, G. M. *Acta Cryst. A* **2008**, *64*, 112–122.

134. Warren, M. R.; Brayshaw, S. K.; Johnson, A. L.; Schiffers, S.; Raithby, P. R.; Easun, T. L.; George, M. W.; Warren, J. E.; Teat, S. J. *Angew. Chem. Int. Ed.* **2009**, *48*, 5711–5714.

135. Delley, B. *Z. Kristallogr.* **2008**, *223*, 329–333.

136. Boldyreva, E. V. *Solid State Ionics* **1997**, *101–103*, 843–849.

137. Boldyreva, E. V. *Russ. J. Coord. Chem.* **2001**, *27*, 323–350.

138. Clark, S. J.; Segall, M. D.; Pickard, C. J.; Hasnip, P. J.; Probert, M. J.; Refson, K.; Payne, M. C. *Z. Kristallogr.* **2005**, *220*, 567–570.

139. Payne, M. C.; Teter, M. P.; Allan, D. C.; Arias, T. A.; Joannopoulos, J. D. *Rev. Mod. Phys.* **1992**, *64*, 1045–1097.

140. Perdew, J. P.; Burke, K.; Ernzerhof, M. *Phys. Rev. Lett.* **1996**, *77*, 3865–3868.

141. Hirshfeld, F. L. *Theoret. Chim. Acta.* **1977**, *44*, 129–138.

142. Wolff, S. K.; Grimwood, D. J.; McKinnon, J. J.; Turner, M. J.; Jayatilaka, D.; Spackman, M. A. *CrystalExplorer (Version 2.1)*, University of Western Australia, 2010.

143. McKinnon, J. J.; Jayatilaka, D.; Spackman, M. A. *Chem. Commun.* **2007**, 3814–3816.

144. Bondi, A. *J. Phys. Chem.* **1964**, *68*, 441–451.

145. Blatov, V. A.; Shevchenko, A. P.; Serezhkin, V. N. *Acta Cryst. A* **1995**, *51*, 909–916.

146. Blatov, V. A.; Shevchenko, A. P.; Serezhkin, V. N. *J. Appl. Cryst.* **2000**, *33*, 1193.

147. Hämäläinen, K.; Siddons, D. P.; Hastings, J. B.; Bernan, L. E. *Phys. Rev. Lett.* **1991**, *67*, 2850–2853.

148. Webb, S. *SIXPACK: Sam's Interface for XAS Package*, Stanford Synchrotron Radiation Laboratory, 2006.

149. Chang, J. P.; Fung, E. Y.; Curtis, J. C. *Inorg. Chem.* **1986**, *25*, 4233–4241.

150. Zhao, M.; Clarke, M. J. *J. Biol. Inorg. Chem.* **1999**, *4*, 318–324.

151. Fay, M. J.; Proctor, A.; Hoffmann, D. P.; Houalla, M.; Hercules, D. M. *Mikrochim. Acta* **1992**, *109*, 281–293.

152. Ressler, T.; Timpe, O.; Neisius, T.; Find, J.; Mestl, G.; Dieterle, M.; Schlögl, R. *J. Catal.* **2000**, *191*, 75–85.

153. Smolentsev, G. Y.; Soldatov, A. V. *J. Surf. Invest.* **2008**, *3*, 398–401.

154. Smolentsev, G.; Guilera, G.; Tromp, M.; Pascarelli, S.; Soldatov, A. V. *J. Chem. Phys.* **2009**, *130*, 174508.

155. Malinowski, E. R. *Factor analysis in chemistry*, 3rd ed.; John Wiley and Sons: New York, 2002.

156. Isied, S.; Taube, H. *Inorg. Chem.* **1974**, *13*, 1545–1551.

157. Vogt, L. H.; Katz, J. L.; Wiberley, S. E. *Inorg. Chem.* **1965**, *4*, 1157–1163.

158. Esmadi, F. T.; Al-Hamid, A. J. *Trans. Met. Chem.* **1994**, *19*, 571–574.